Thermal Analysis and Testing of a Spaceborne Passive Cooler

Graham Jones

St. Cross College, Oxford

A thesis submitted for the degree of Doctor of Philosophy

in the University of Oxford

September 1994

ABSTRACT

Thermal Analysis and Testing of a Spaceborne Passive Cooler

Graham Jones
St. Cross College, Oxford

A thesis submitted for the degree of Doctor of Philosophy in the University of Oxford

This thesis describes the thermal design and thermal testing of the development model radiative cooler for the Composite Infra-Red Spectrometer (CIRS) due for launch on the Cassini spacecraft in 1997.

The radiative cooler is used to cool the instrument's Focal Plane Assembly (FPA) to approximately 80K. The FPA holds two arrays of HgCdTe detectors for the mid infra-red spectrometer of the instrument which covers the wavelength range $7\mu m$ to $17\mu m$.

The FPA is mounted from the optics on a titanium alloy tripod and is cooled conductively by the radiator via a flexible link and a cold finger. A range of thermal models of the system have been developed ranging from a simple, analytical model to a finite difference numerical model.

A calorimeter was designed to perform heat leak measurements on samples of Multi-Layer Insulation (MLI) blankets to determine the number and type of shields required for the MLI blanket covering the back of the cooler radiator.

A test facility incorporating a vacuum system, a space simulator target, and a simulator for the CIRS instrument was designed and constructed for testing the assembled cooler.

Various configurations of the Development Model (DM) CIRS cooler were tested as components became available and the results obtained compared to the thermal model predictions. It was found that the cooler will attain a temperature of 80K in operation, but with less excess cooling power than predicted by the thermal models.

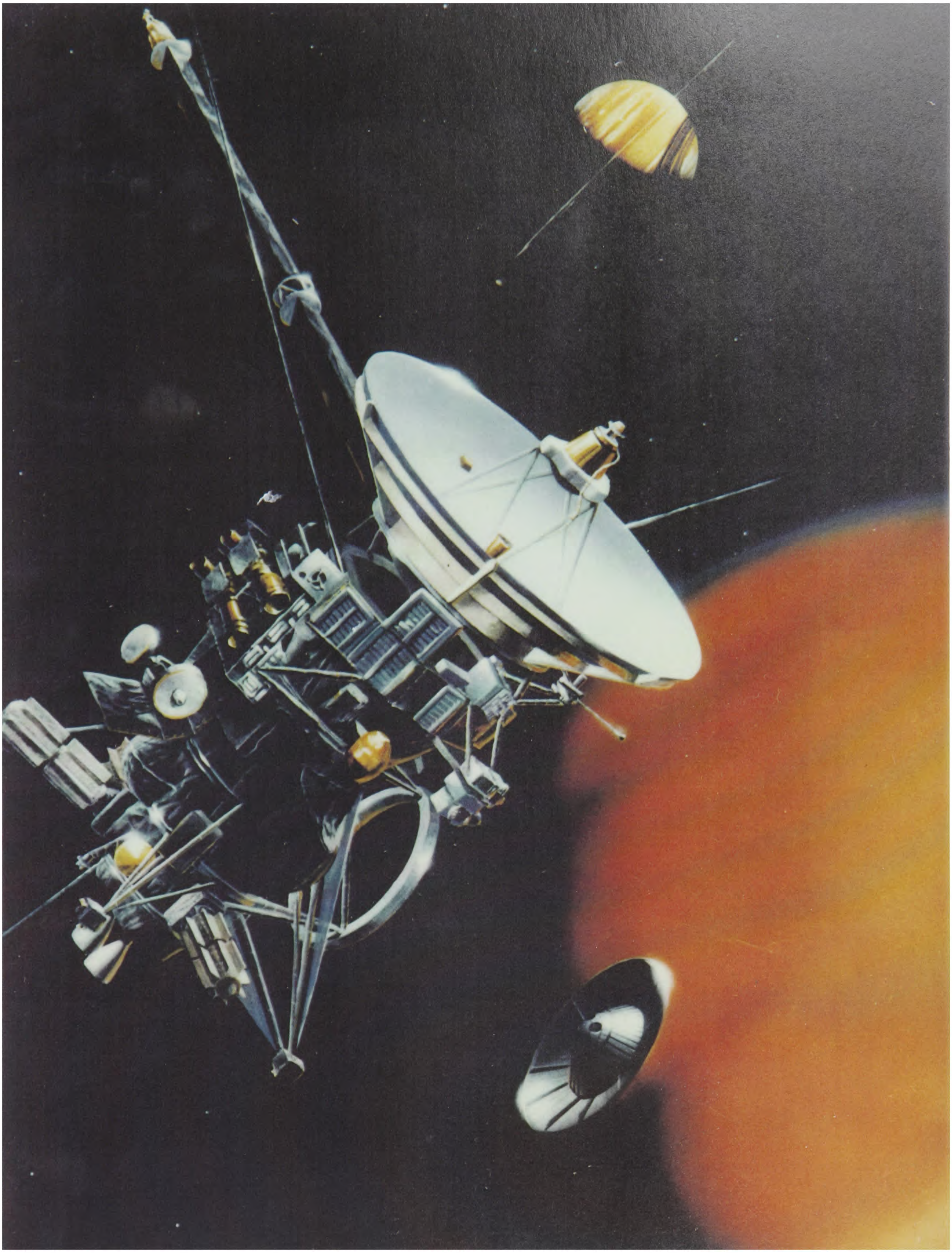

An Artist's Impression of Cassini at Titan (Jet Propulsion Laboratory)

Contents

Acknowledgements

Space projects inevitably involve a large number of people to make them work. I would like to thank the following people for their contributions, without whom this work would have been impossible:

My supervisor, Simon Calcutt for giving me the opportunity to work on this project, for his insistence that all my strange statements be proved conclusively before believing me, and for proof reading this thesis.

The late Steve Werrett for the original conceptual design of the cooler and thermal budget, and for his advice on the thermal analysis.

Tim Vellacott for performing the detailed design on the cooler and for successfully finding enough pieces of the cooler for me to perform the thermal tests described in Chapter 6.

Bob Watkins for designing the test facility vacuum chamber and pumping system, and for his invaluable advice during the commissioning of the test facility.

Ish Aslam, Chris Hepplewhite and Nick O'Donnell for their numerous contributions to the CIRS project.

The workshop staff, Mick Johnson, Martin Clarke, Gabby Nichols, Andy Clack, John Temple, Mark Sanders and Ed Morgan for their help in constructing the cooler test facility.

The SERC for providing a three year studentship to fund the work.

I would like to thank my parents for their moral and financial support during my stay in Oxford, and their encouragement to complete this thesis afterwards. Finally I would like to thank Sandie for her encouragement in the writing of this thesis, and for persuading me to take the time to finish it.

Preface

The work described in this thesis has formed a small part of the development of the Cassini Mission in general and the CIRS instrument in particular. Consequently a substantial amount of the work described in this thesis has not been performed by the Author alone but as part of a large team. The sections of the work which were performed by the Author were:

1. Development of the thermal models of the CIRS cooler and focal plane assembly (FPA).

2. An input into the selection of materials for the CIRS cooler and FPA.

3. Measurements of the emissivities of multi-layer insulation (MLI) blankets and the design of the equipment to perform the measurements.

4. Development of the cooler test facility.

5. Testing of the cooler test facility.

6. Testing of the development model (DM) CIRS cooler

7. Recommendations for the improvement of the cooler and FPA thermal performance.

The author was not involved in the mechanical design of the cooler and FPA, which was carried out by Dr. Vellacott at Oxford.

Abbreviations

CIRS	Composite Infra-Red Spectrometer
CLAES	Cryogenic Limb Array Etalon Spectrometer
DAOPP	Department of Atmospheric, Oceanic and Planetary Physics
DM	Development Model
ESA	European Space Agency
ESATAN	Thermal Analysis Package
FIR	Far Infra-Red
FM	Flight Model
FNM	Full Numerical Model
FP1,FP3,FP4	Focal Plane 1 (3 or 4)
FPA	Focal Plane Assembly
GSFC	Goddard Space Flight Center
ILM	Intermediate Level Model
IRIS	Infra-Red Interferometer Spectrometer
ISAMS	Improved Stratospheric and Mesospheric Sounder
MLI	Multi-Layer Insulation
MIR	Mid Infra-Red
NASA	National Aeronautics and Space Administration
PC	Photo Conductive
PID	Proportional, Integral, Derivative (Controller)
PRT	Platinum Resistance Thermometer
PV	Photo Voltaic
RGA	Residual Gas Analyser
RTG	Radioisotope Thermal Generator
SAM	Simple Analytical Model
SINDA	Thermal Analysis Package
SNM	Simple Numerical Model
SSPTA	Radiation Analysis Package
UARS	Upper Atmosphere Research Satellite

Chapter 1

The Saturn System and the Cassini Mission

This chapter gives a very brief overview of measurements of Saturn and its largest satellite, Titan. References [1], [2], [3] and [4] contain detailed reviews of the subject. A brief description of the Cassini mission is given in Section 1.3.

1.1 The Atmosphere of Saturn

The basic astronomical data for Saturn is shown in Table 1.1.

Table 1.1: Astronomical Data on the Saturn System [6].

Mean Distance from the Sun	9.54	Au
Orbital Period	10759	days
Rotational Period	10.2	hours
Equatorial Radius	60000	km

1.1.1 Composition

A large amount of our current knowledge of the composition of the atmosphere of Saturn has come from the IRIS infra-red spectrometers on the two Voyager spacecraft. The data analysis [5] required the averaging of a number of spectra in order to improve the signal to noise ratio of the sample. Figure 1-1 shows a typical averaged IRIS spectrum. The

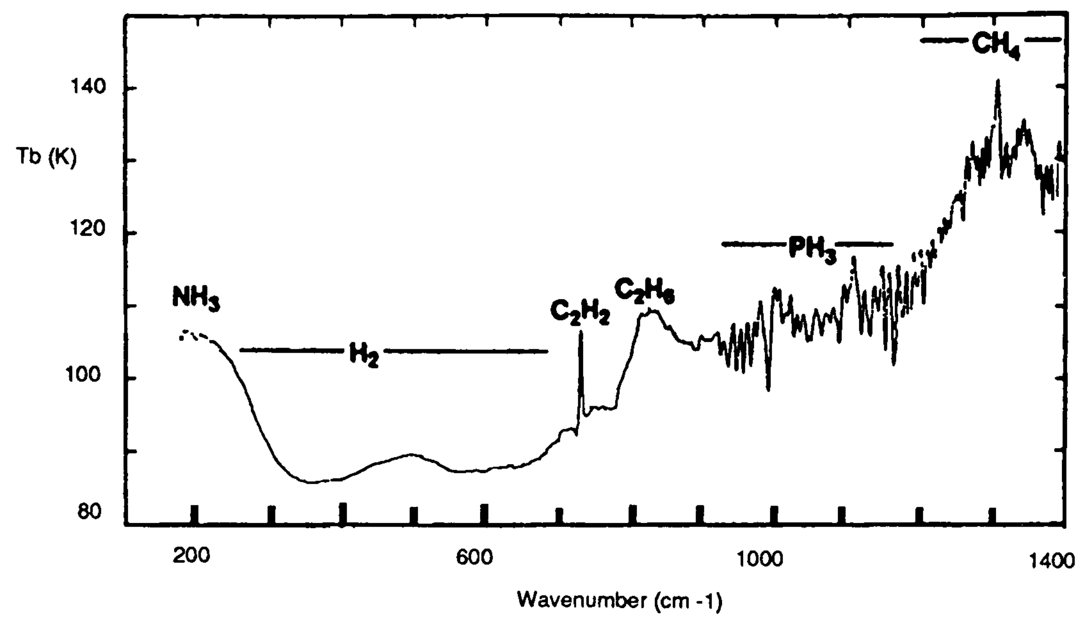

Figure 1-1: Voyager IRIS brightness temperature spectrum (T_b) [5].

figure shows the infra-red bands of methane (CH_4), phosphine (PH_3), ammonia (NH_3) and the hydrocarbons ethane (C_2H_6) and ethyne (C_2H_2).

The atmosphere of Saturn is composed predominantly of molecular hydrogen and helium. The analysis of Voyager IRIS and radio occultation data has retrieved the mole fraction of H_2 as 0.963 ± 0.024 [2]. The uncertainty in the retrieved mole fraction of helium in the atmosphere is large, but it is clear that helium is depleted by comparison to solar values. The depletion of helium is consistent with theories which predict that helium will precipitate into the metallic hydrogen core and release thermal energy. This theory is used to account for the emitted thermal radiation flux being greater than the absorbed solar flux by a factor of around 2 [1].

Methane (CH_4) is present in significant quantities in the atmosphere (The CH_4/H_2 abundance is approximately 4.5×10^{-3} [5]). This figure was derived from IRIS spectra using the temperature profile from radio occultation measurements (Figure 1-2).

The hydrocarbons ethane (C_2H_6) and ethyne (C_2H_2) have been detected (Figure 1-1) and latitudinal variations in the mixing ratios have been observed. A number of species have been predicted to exist as trace constituents but have not yet been detected. For example Hydrazine, methylamine and ethylene have been predicted and should be detectable in the infra-red if sufficient spectral resolution is available [2].

1.1.2 Thermal Structure

The thermal structure of Saturn has been studied both by ground based astronomy and spacecraft measurements. A typical vertical temperature profile is shown in Figure 1-2[1]. The figure shows both a global mean profile and a single profile obtained from radio occultation measurements during the Voyager 2 ingress. Also marked on the figure is the level at which ammonia would condense to form clouds assuming solar atomic composition. The minimum temperature of around 80K occurs at around the 100mbar level. The inversion of the temperature profile at this point is caused by the absorption of solar energy by methane.

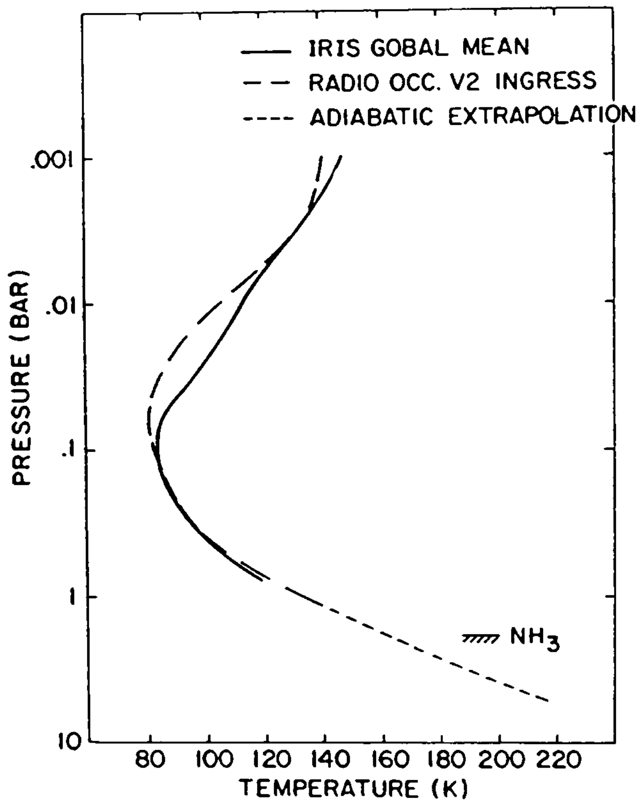

Figure 1-2: The vertical temperature structure of Saturn [1]

1.2 The Atmosphere of Titan

Titan is Saturn's largest satellite and orbits at a distance of 20.3 Saturn radii. It has a radius of 2575km, which makes it comparable in size to many of the terrestrial planets.

The surface of Titan is completely hidden from view by a dense cloud layer. The composition of the cloud layer remains uncertain, but theoretical simulations suggest a mixture of organic polymers.

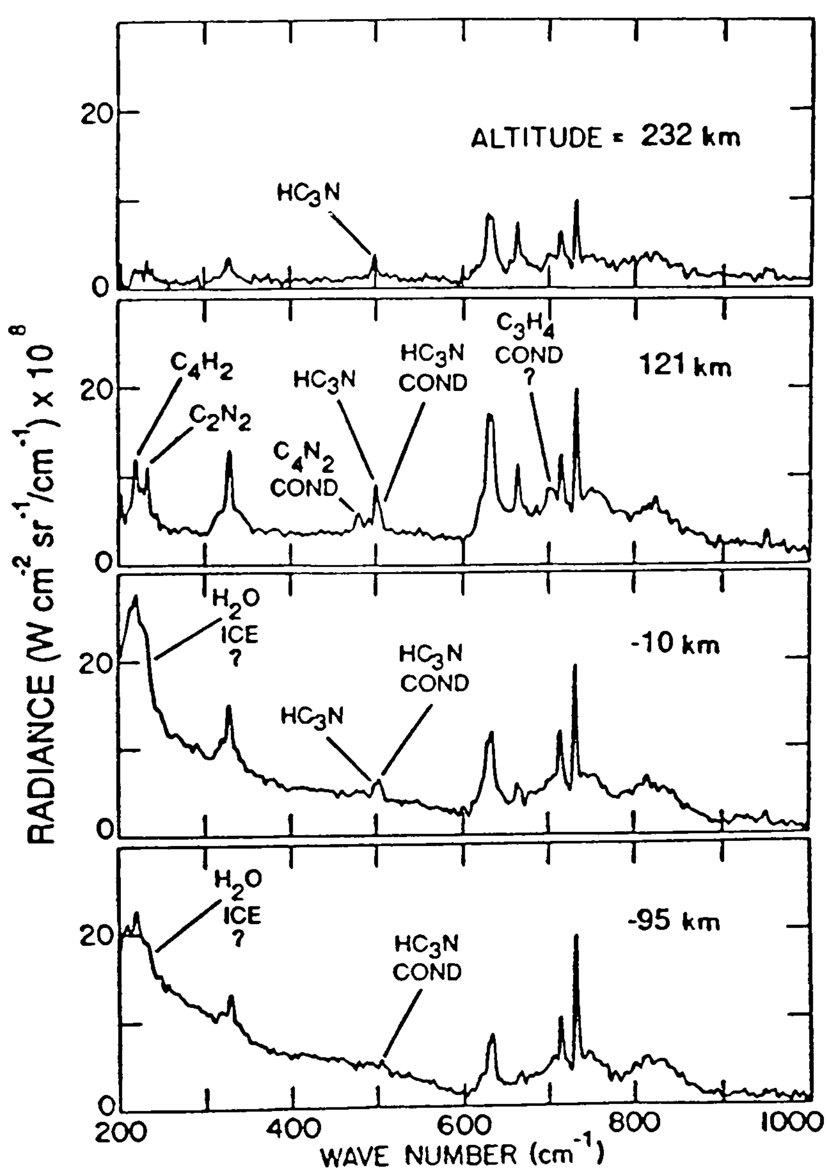

Figure 1-3: Titan limb emission spectra from IRIS at various tangent heights [7]

1.2.1 Composition

Measurements of Titan were taken by the two Voyager spacecraft. A great deal of our knowledge of its atmosphere has come from the IRIS infra-red spectrometers and radio occultation experiments on the spacecraft.

Figure 1-3 shows emission spectra from the limb of Titan. They were taken using IRIS at a resolution of 4.3cm^{-1} for various tangent heights.

The atmosphere of Titan is predominantly nitrogen with significant amounts of methane (between 2 and 10% [1]). It is suspected that argon may be present in the atmosphere (from the derivation of the relative molecular mass of the atmosphere using radio occultation and IRIS data [3]), but this has not been measured directly.

Methane (CH_4) in the atmosphere dissociates under solar irradiation to produce free radicals such as H and CH_2. The free radicals lead to the creation of heavier hydrocarbons such as ethane (C_2H_6), ethene (C_2H_4) and propane (C_3H_8). A large number of nitrogen species are formed in these reactions such as HCN, HC_3N and C_2N_2. Some of the nitriles and hydrocarbons which were identified in the atmosphere from the Voyager data have been shown to exhibit latitudinal and vertical variations, but the precise measurement of the variations will require higher spectral resolution and better spatial coverage than that available from the Voyager IRIS instrument [3]. It is believed that the dark orange or brown aerosols in the upper atmosphere are the products of the methane photochemistry.

Ethane (C_2H_6) is liquid at the conditions present at the surface, leading to speculation on the presence of a global ocean of ethane and other hydrocarbons. The methane which is destroyed by the photochemical reactions must be being replaced from either the interior of the planet or the ocean. It is suspected that the ocean will therefore be a mixture of molecular nitrogen, methane and ethane [4]. It would therefore act as a reservoir for methane which will gradually be replaced by the ethane and other products of the photochemistry which are formed in the upper atmosphere and precipitate out.

1.2.2 Thermal Structure

The vertical temperature profile of Titan is shown in Figure 1-4 [1]. The temperature falls from 94K at the surface to a minimum of 71K at the tropopause. It then rises to around 170K at the 1 mbar level. The temperatures throughout the profile are above the condensation temperature of nitrogen so the formation of nitrogen clouds is unlikely. Both the ingress and egress profiles are similar showing that the troposphere does not vary a great deal with either latitude or local time [1]. This is because of the high density and the low temperature of the atmosphere which result in a long thermal time constant.

1.3 The Cassini Mission

The purpose of the Cassini Mission is to perform a detailed exploration of the Saturn system and in particular Titan. The mission will comprise an orbiter which will be provided by NASA and an entry probe supplied by ESA. The probe will be dropped into the atmosphere of Titan during the first encounter to make detailed in-situ measurements during its three hour decent. The orbiter will perform a four year, 63 orbit tour of the Saturn system. Its orbit will be shifted by gravity assists at each encounter with Titan to

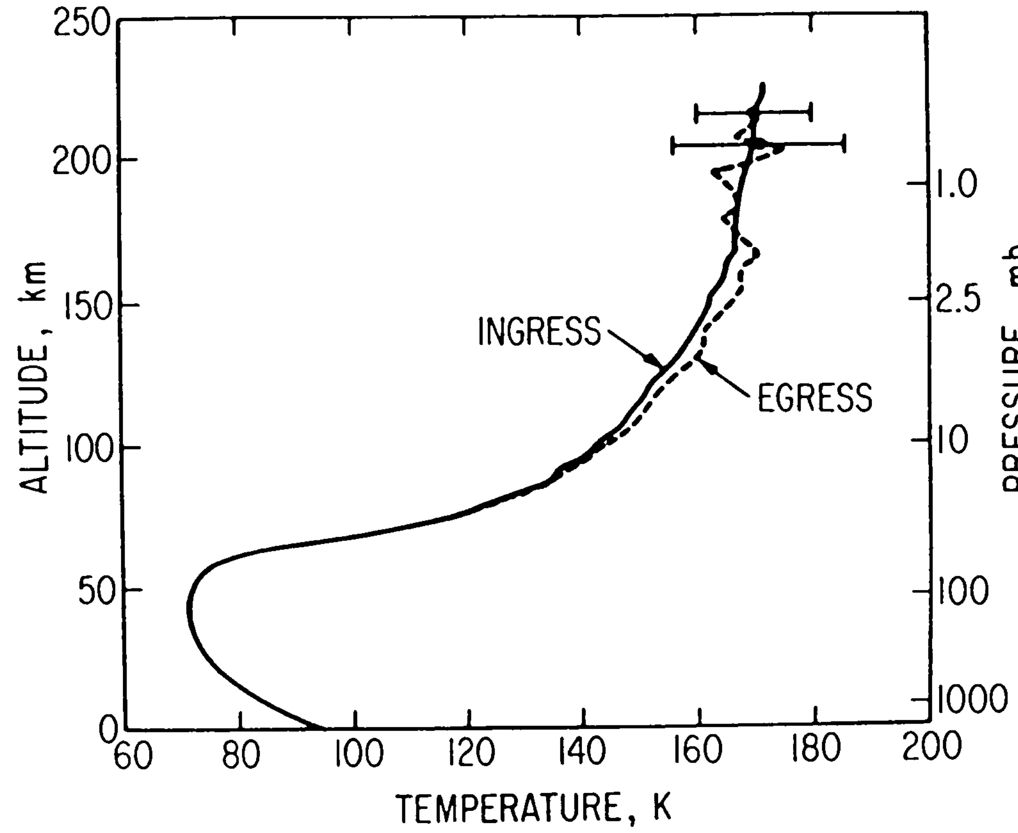

Figure 1-4: Temperature profile of Titan from Voyager 1 [1].

increase the coverage of both Saturn and Titan. The orbiter carries both remote sensing and particles and fields instruments.

The long duration of the mission will add to the knowledge gained from the Pioneer and Voyager fly-bys by taking measurements over a long time period. Cassini will complement the similar Galileo mission to Jupiter.

Cassini is due for launch in 1997 and is expected to arrive at Saturn in 2004 after a 6.7 year cruise. The interplanetary trajectory to be followed is shown in Figure 1-5. The closest approach to the Sun is 0.6Au around the time of the Venus encounters.

1.3.1 Scientific Objectives

Some of the main atmospheric science objectives for the Cassini Mission are listed below:

1. Titan

   - Determine the abundances of atmospheric constituents and establish the isotope ratios of the abundant elements. The abundances of many of the atmospheric gases are expected to vary sharply because the low tropopause temperature acts as a cold trap which limits their abundances in the stratosphere. The isotope ratios may be used to constrain scenarios of the formation and

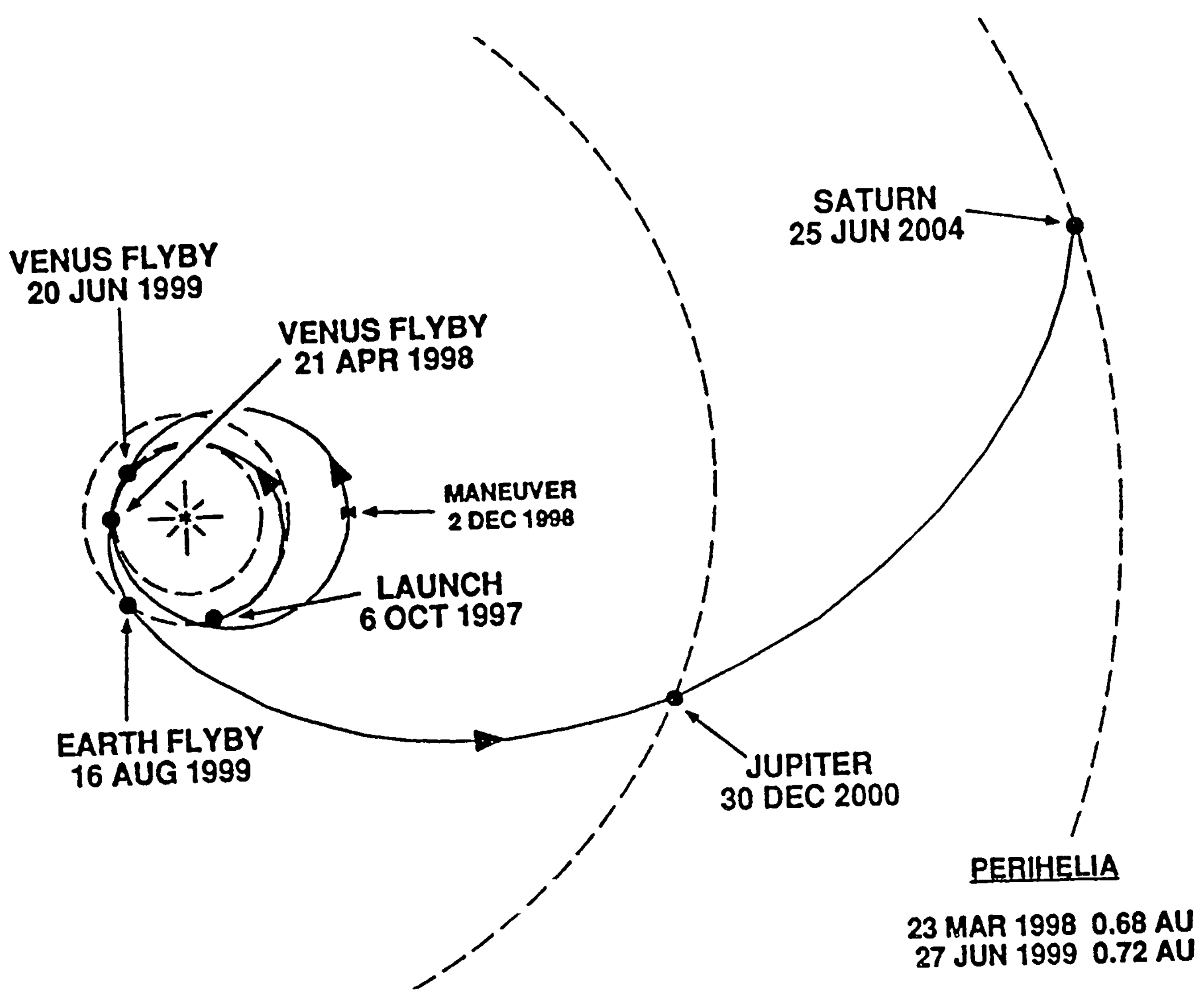

Figure 1-5: Cassini Spacecraft Trajectory (Jet Propulsion Laboratory)

evolution of the atmosphere. The measurements will be performed using both remote sensing instruments and the mass spectrometer on the probe.

- Observe vertical and horizontal distributions of trace gases, search for more complex organic molecules. This data will be useful in constraining photochemical models of the atmosphere which predict a number of species which were not identified using the Voyager data.
- Measure winds and global temperatures; investigate general circulation and seasonal effects in Titan's atmosphere. This data is required for studies of the general circulation of the atmosphere of Titan. Because of the lack of distinguishable cloud features the winds will be tracked using tracer gases.
- Determine the physical state, topography and composition of the surface and infer the internal structure. The composition of the ocean (if any) is required to constrain chemical models of the atmosphere.

2. Saturn

   - Determine the global temperature field. This data is measured by inverting data measured by the remote sensing instruments and by radio-occultation.
   - Measure the global wind field. The wind field can be measured by tracking cloud features. The wind field at other altitudes can be deduced from the temperature field. This data is necessary to study the dynamics of the atmosphere.
   - Measure gas compositions, isotope ratios etc. This data can be used to constrain scenarios for the formation of Saturn and chemical models of the atmosphere.

1.3.2 Spacecraft Configuration

The Cassini Spacecraft is shown schematically in Figure 1-6. One end of the spacecraft body holds the high gain antenna, which doubles as a radiation shield for the electronics and the instruments. The body of the spacecraft contains the spacecraft electronics and the fuel tanks. The remote sensing instruments are attached to the side of the spacecraft on a pallet. Power is supplied using three Radioisotope Thermal Generators

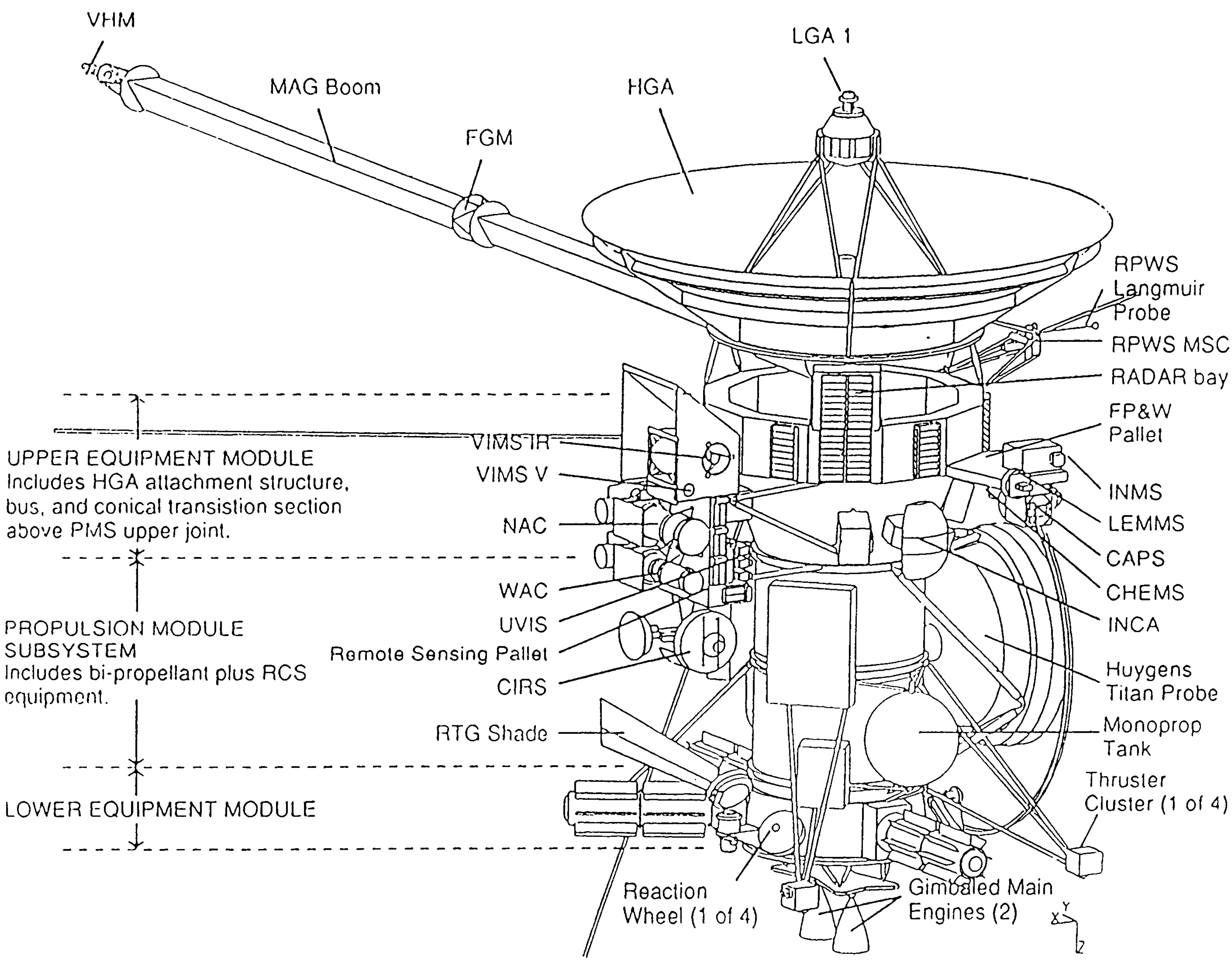

Figure 1-6: The Cassini Spacecraft Configuration (Jet Propulsion Laboratory)

(RTG's). The magnetometer instruments are mounted on an extendible boom away from the spacecraft body.

1.3.3 Atmospheric Remote Sensing Instruments

The atmospheric remote sensing instruments carried on the Cassini orbiter are summarised in Table 1.2. The payload consists of a number of cameras working in the visible for tracking cloud patterns to determine the atmospheric circulation, and spectrometers working in both the ultra-violet and the infra-red which will be used to investigate the atmospheric composition, temperatures and dynamics. Because the atmospheres of both Saturn and Titan are at similar temperatures only one set of instruments is required to study both atmospheres.

The instrument of concern in this work is the Composite Infra-Red Spectrometer (CIRS) which is being developed at Goddard Space Flight Center with sub-assemblies being supplied by a number of other institutions. DAOPP is supplying one of the two focal plane assemblies and the 80K radiative cooler for the detectors.

Table 1.2: The Cassini Orbiter Atmospheric Remote Sensing Instrument Payload

Instrument	Main Objectives
Imaging Science Subsystem (ISS)	Imaging atmospheres, satellites & rings
Visible and Infrared Mapping Spectrometer (VIMS)	Atmosphere composition and vertical, and horizontal distribution of constituents.
Composite IR Spectrometer (CIRS)	Atmosphere composition and vertical, and horizontal distribution of constituents. Deep sounding of Saturn and Titan
Ultra-violet Imaging Spectrograph	Saturn and Titan atmospheric composition, ionosphere remote sensing

Chapter 2

The Composite Infrared Spectrometer

2.1 The CIRS Instrument

The Composite Infra-Red Spectrometer (CIRS) is a remote sensing instrument to be flown on the Cassini Saturn orbiter. It is a development of the IRIS interferometer-spectrometer flown on the Voyager spacecraft and aims to improve upon the measurements taken by IRIS by extending the spectral range into the far infra-red, having a higher spectral resolution and a smaller field of view than IRIS (see Table 2.1). Additionally the long term measurements possible from an orbiter will provide a significant improvement over the measurements possible from the Voyager fly-by missions.

The spatial resolution of the CIRS instrument of 0.2mrad for frequencies greater than 600cm^{-1} and its use of ten element detector arrays at these frequencies will allow limb scanning of both Saturn and Titan at vertical resolutions comparable with the scale heights of the atmospheres.

2.1.1 Science Objectives

The infrared spectrum of Titan is dominated by absorption-emission bands of hydrocarbons and nitriles such as C_4H_2, C_2N_2 and HC_3N. It is believed that these are due to a complex set of photochemical reactions in Titan's stratosphere which may have lead to the existence of an ethane based ocean and many more compounds which have not yet

Table 2.1: Comparison of the performance of the IRIS and CIRS Instruments

Property	IRIS	CIRS
Spectral Range (cm^{-1})	180-2500	10–1400
	(4-55μm)	(7-1000μm)
Spectral Resolution (cm^{-1})	4.3	0.5
Spatial Resolution (mrad)	4.3	0.2 (600–1400cm^{-1} range)
		4.3 (<600cm^{-1})

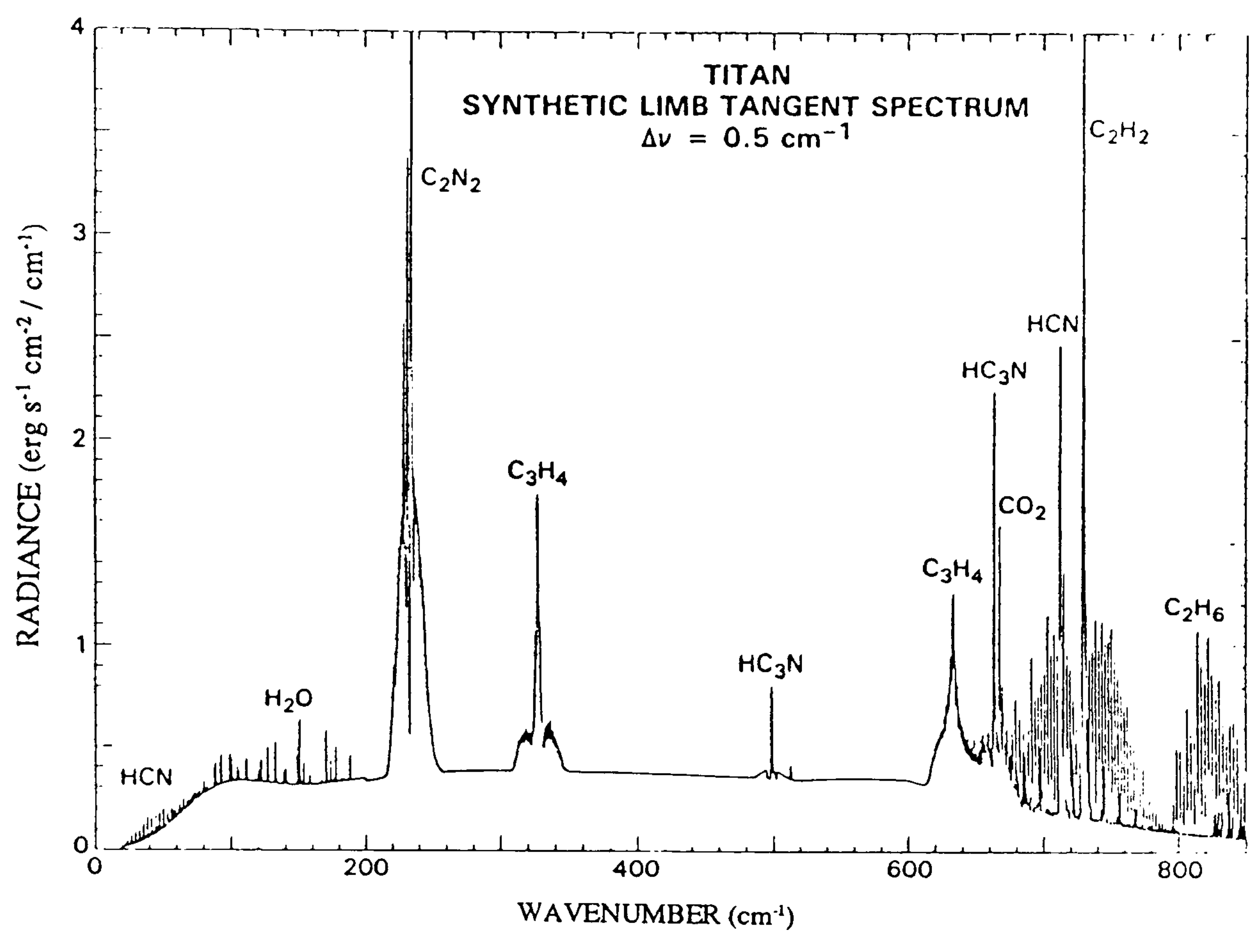

Figure 2-1: Calculated Titan limb emission spectrum at 0.5cm^{-1} spectral resolution [7].

been detected on Titan, but which have detectable infrared bands in the CIRS wavelength range [7]. A simulated limb tangent spectrum of Titan at 0.5cm^{-1} resolution is shown in Figure 2-1. It can be seen that CIRS has the ability to resolve a large number of spectral features and therefore identify chemical species.

In order to determine the abundances of the species the atmospheric temperature must also be measured. The vertical temperature profile can be measured if the abundance profile of any of the species is already known. Methane will be used in the upper atmosphere and N_2 below about 1mbar in a similar way that CO_2 is used to sound the Earth's temperature profile. Figure 2-2 shows the height range over which CIRS will measure temperatures on Titan. It will be possible to map temperature profiles and

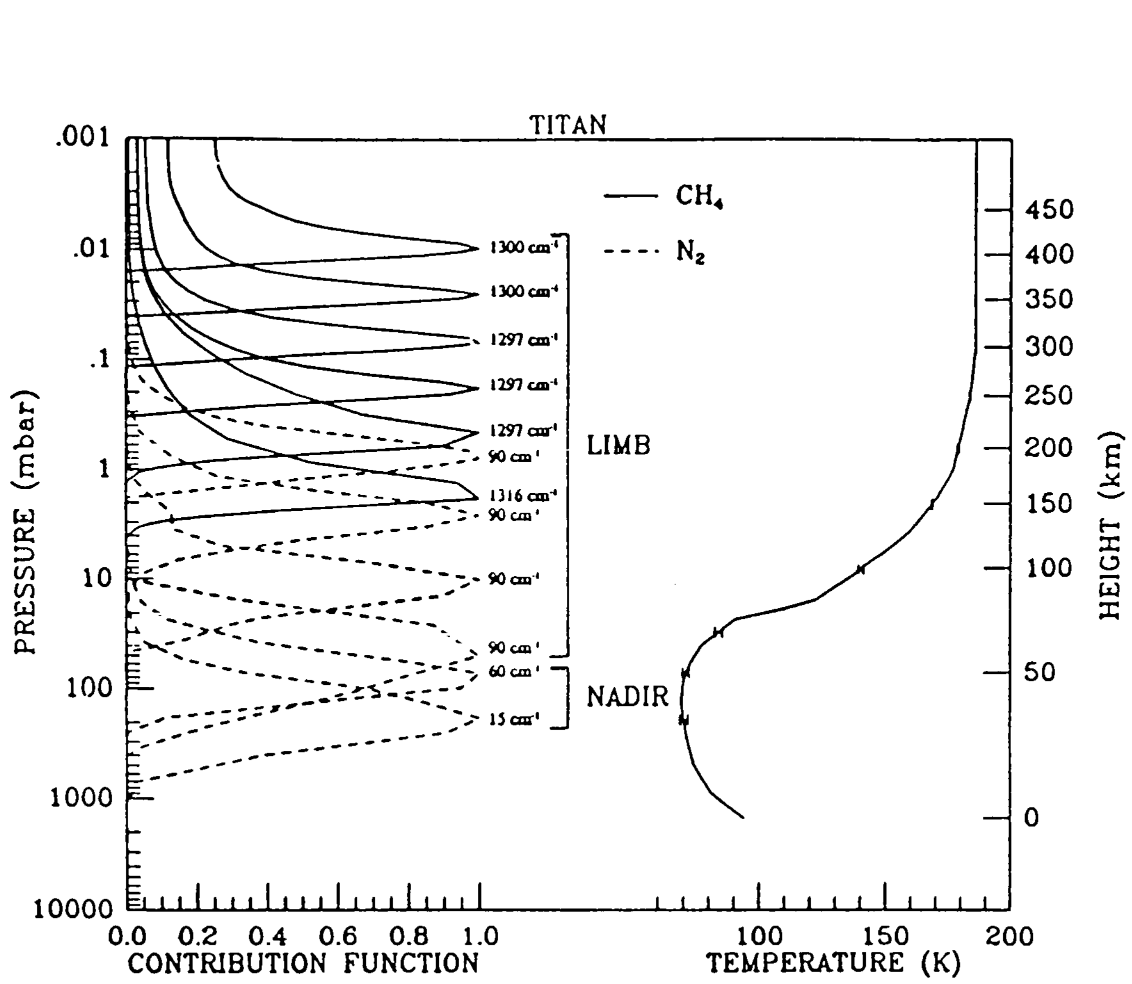

Figure 2-2: CIRS contribution functions for nadir and limb viewing of Titan [7].

chemical abundances over a large portion of the globe of Titan to build a picture of dynamical and chemical processes in the atmosphere.

Despite the differences between the atmospheres of Saturn and Titan the properties and temperatures of their upper atmospheres are similar so CIRS will be able to take measurements of the atmospheres of both bodies. The Cassini orbit [9] has a typical closest approach to Saturn of around five Saturn radii. In order to achieve vertical resolutions comparable to the scale height of the atmosphere when limb scanning under these conditions a very narrow field of view is required. The CIRS spatial resolution of 0.3mrad for its mid infra-red (MIR) interferometer was chosen to enable these measurements to be performed.

The CIRS contribution functions for Saturn are shown in Figure 2-3. The main difference between the figures for Titan and Saturn is that the deep atmosphere absorption is due to pressure induced hydrogen lines on Saturn, but it is due to pressure induced nitrogen lines on Titan. In addition to measuring temperature profiles on Saturn, CIRS will be used to study NH_3 clouds and the stratospheric haze caused by photochemistry.

The long wavelength interferometer in CIRS can be used to study thermal emission from Saturn's rings by probing through the outer layers of the ring particles to study

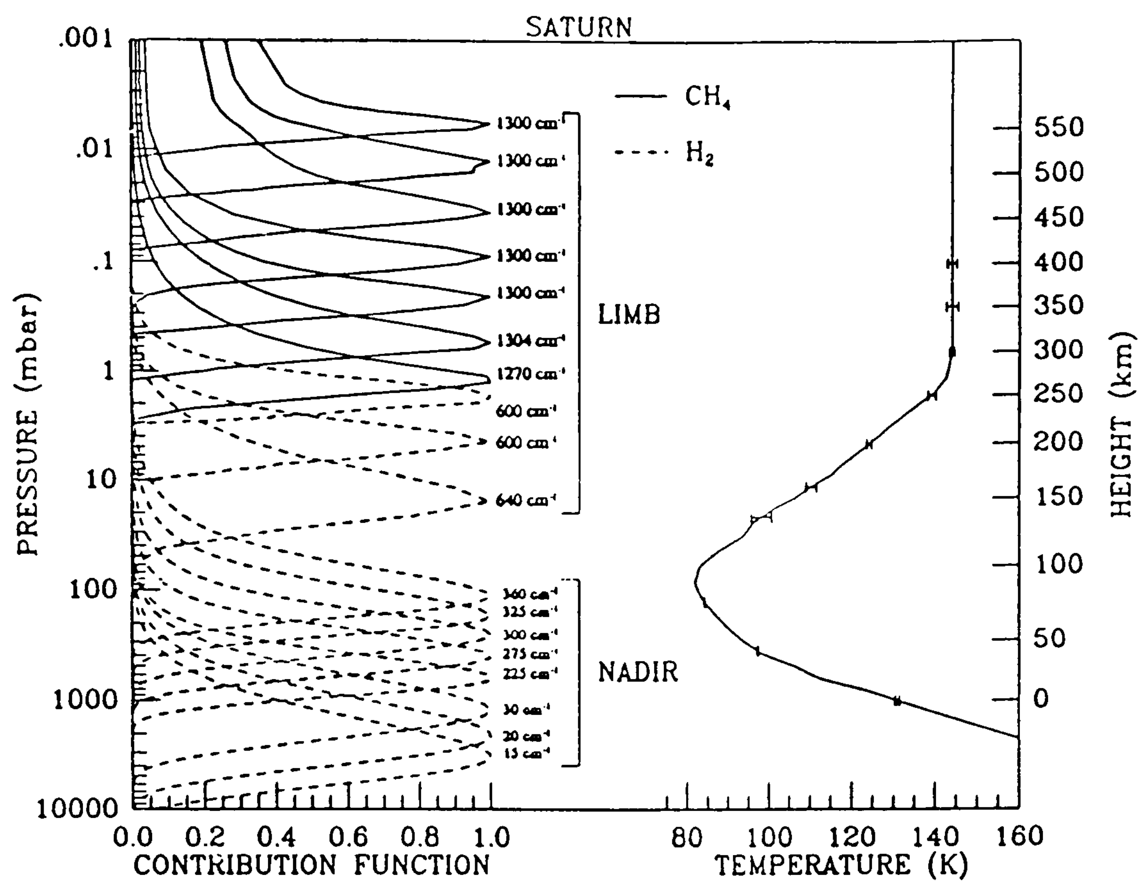

Figure 2-3: CIRS contribution functions for nadir and limb viewing of Saturn and a nominal temperature profile for the atmosphere [7]

ring thickness, particle composition etc.

The data measured by CIRS at Titan and Saturn will be used to study a number of processes including the energy balance of the atmospheres, compositions and photochemistry, to constrain theories of the development of the atmospheres and to study the dynamics of the atmospheres.

2.1.2 Instrument Description

Optics

The CIRS instrument is a twin Fourier transform spectrometer. The conceptual configuration is shown in Figure 2-4. Both interferometers share a 50cm diameter Cassegrain telescope by the use of a field splitting mirror which gives adjacent fields of view. The Mid Infra-Red (MIR) interferometer is a conventional Michelson interferometer covering the spectral range $7\mu m$ to $17\mu m$ using two ten element HgCdTe detector arrays (FP3 and FP4). The Far Infra-Red (FIR) interferometer is a polarising interferometer which extends the instruments spectral range out to $1000\mu m$ using two thermopile bolometer detectors (FP1). The two interferometers use the same mirror motor as shown in

Figure 2-5.

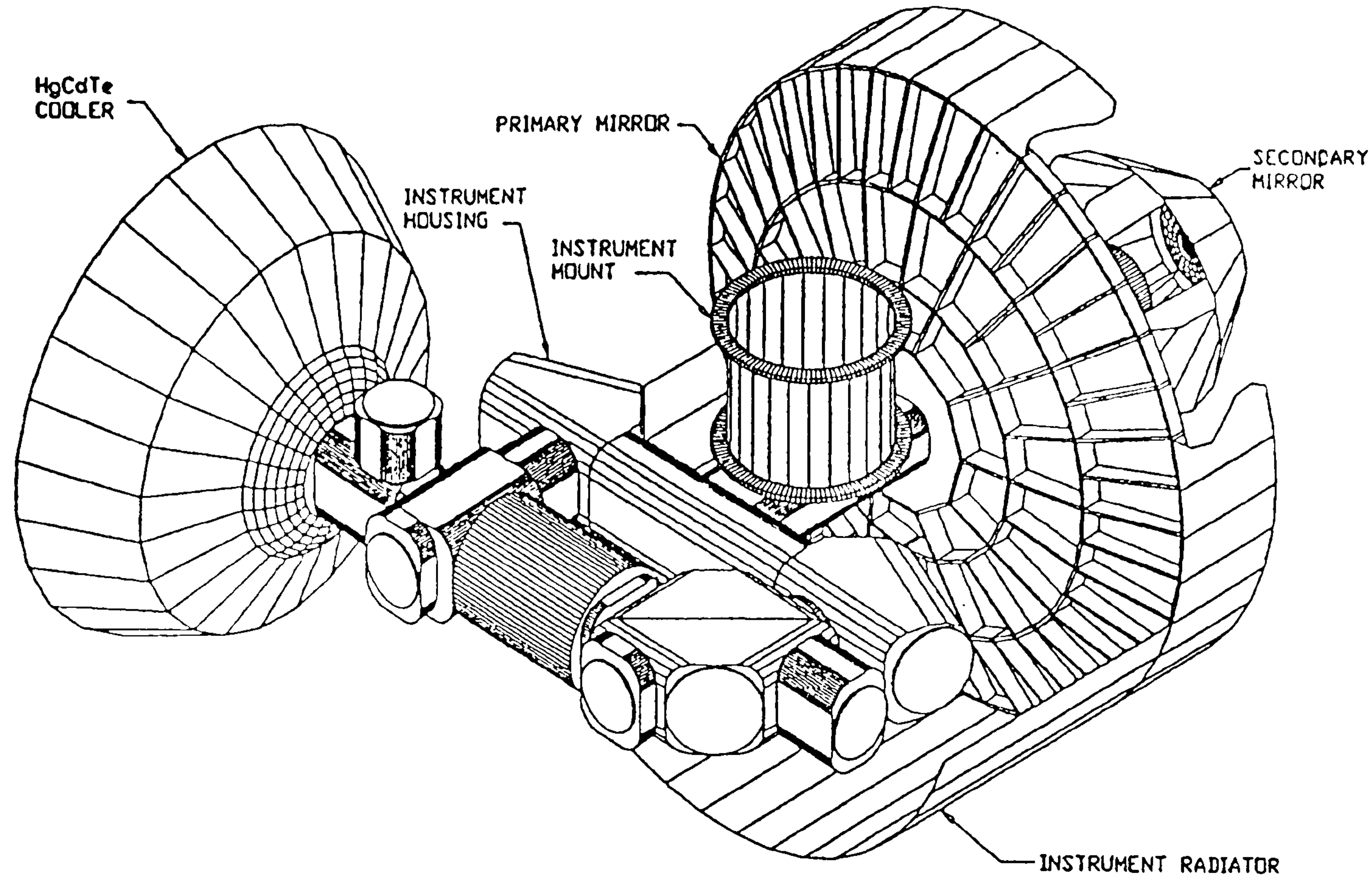

Figure 2-4: Conceptual Configuration of CIRS [8]

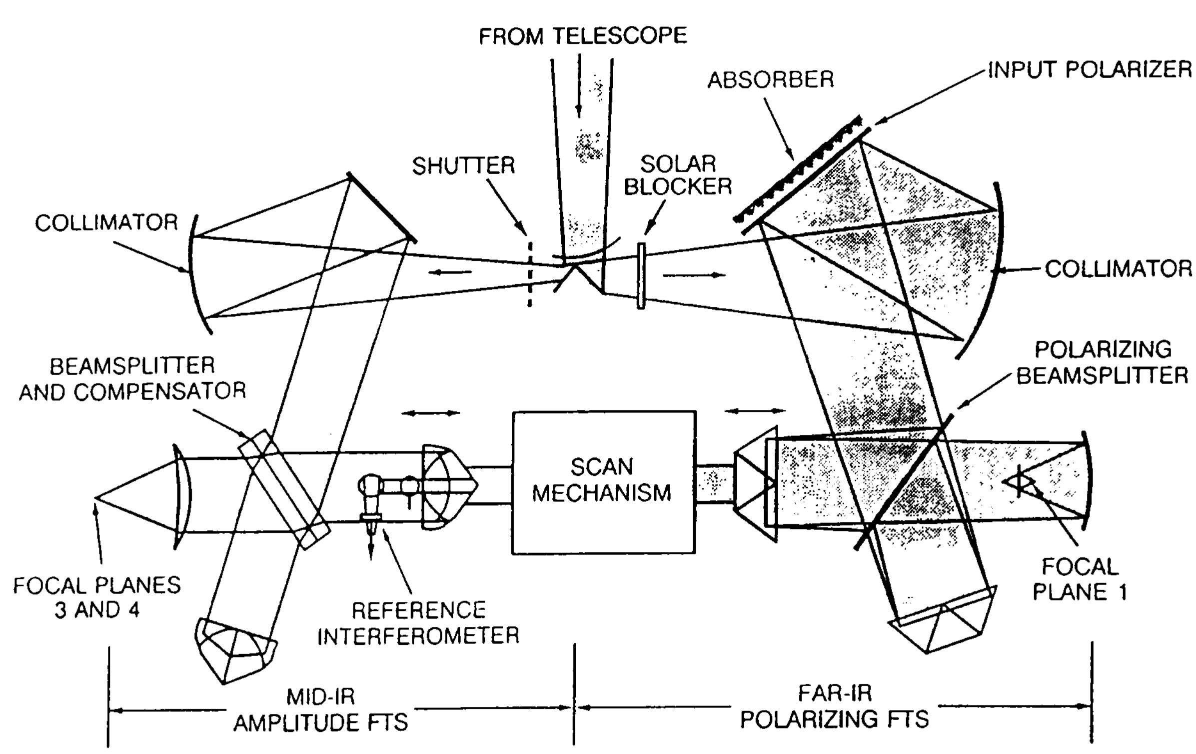

Figure 2-5: Schematic of the CIRS Optics [9].

Thermal Design

The CIRS instrument optics module is designed to operate at 170K in order to reduce the background radiation onto the detectors. This is accomplished by mounting the instrument from the warm spacecraft on a low conductivity support and using radiators on the telescope and instrument housing. These radiators will be directed towards space to cool the instrument, and electronic temperature controllers will be used to maintain a steady temperature during operation.

The HgCdTe detectors in focal planes 3 and 4 (FP3 & FP4) are cooled to 80K to maximise the detector performance. This is accomplished using a radiative cooler. The design and testing of this cooler forms the bulk of the remainder of this thesis.

2.2 Spacecraft Cryogenic Cooling

The HgCdTe detector arrays are required to be cooled to 80K during operation. A number of methods for producing cryogenic temperatures in spacecraft have been used in the past and were considered for CIRS. Some of these methods are discussed below.

2.2.1 Stored Cryogens

The simplest way of attaining cryogenic temperatures on a spacecraft is to carry a dewar of a cryogenic material in either liquid or solid form. The detectors to be cooled would then be mounted on the wall of the dewar to use the cryogen as a heat sink. Suitable cryogens could be for example solid argon or liquid helium. The temperature at which the cryogen boils or sublimes is varied by throttling the exhaust valve to vary the pressure above the cryogen. This method of cooling was used successfully by the CLAES instrument on the UARS spacecraft. Stored cryogen coolers are unsuitable for use on the Cassini mission because of the extremely long mission duration - CLAES was a heavy, earth orbiting instrument which still had only an 18 month lifetime so making a stored cryogen system which would weigh only 2.5kg (the mass of the CIRS cooler) and which would have sufficient life time for the Cassini mission would be impractical.

2.2.2 Mechanical Coolers

A number of mechanical coolers have been flown to produce 80K temperatures on spaceborne instruments [10, 11], for example the ISAMS instrument on UARS used two Stirling cycle coolers producing approximately 800mW of cooling at 80K. They consumed approximately 30W of electrical power and weighed over 4kg. This level of cooling is considerably more than the 200mW total cooling power needed for the CIRS 80K stage. If we were to assume that the ISAMS coolers could be scaled down without degrading their efficiency it would be likely that they could meet the 2.5kg mass budget, but they would require of the order of 7W electrical power which is almost half of the power requirements of the whole instrument. The mechanical coolers currently available commercially have an operating lifetime which is too short for use on Cassini, and would create vibration problems on CIRS. A large amount of development work would therefore be required to reduce the power requirement and increase the operating life time to levels usable in the outer solar system.

2.2.3 Radiative Coolers

Radiative coolers are simple passive cooling devices. The principle of operation is that a high emissivity radiator is directed towards space which has an effective temperature of approximately 4K and an emissivity of unity. The power radiated to space is then given by:

$$q_r = \epsilon_r A_r \sigma (T_r^4 - T_s^4) \tag{2.1}$$

where q_r is the radiated power, ϵ_r is the emissivity of the radiator, A_r is the area of the radiator, σ is the Stefan-Boltzmann constant (5.67×10^{-8}W/m^{2}K^4), T_r is the radiator temperature and T_s is the temperature of space. Equation 2.1 gives a radiated power of 209mW for a 0.1m^2 radiator of emissivity 0.90 operating at 80K with a clear view to cold space. In operation this cooling power will be balanced by the heat load into the focal plane being cooled, the parasitic heat leaks into the radiator from the support structure and any thermostat heater power used.

For deep space missions radiative coolers have a number of advantages over the other types of coolers discussed for cooling detectors:

- They require no electrical power to provide cooling. This is especially important in the outer solar system where solar arrays are not usable so the electrical power must be provided by thermal generators (RTG's).

- There are no moving parts, giving an effectively unlimited lifetime. The main limitation is the degradation of the surfaces due to contamination or radiation.
- Their mass is significantly lower than an equivalent stored cryogen cooling system.

For these reasons a radiative cooler was the obvious choice for the cooling method for the CIRS detectors. The following section describes the overall design of the CIRS cooler.

2.3 The CIRS Cooler

2.3.1 Design Philosophy

It is necessary to cool the HgCdTe detector arrays of the CIRS instrument to 80K or lower during operation in order to optimise the performance of the detectors. It is a system requirement that the CIRS cooler should be able to tolerate absorbing 50mW of environmental backloading from the planet or rings and still maintain a temperature of 80K. The figure of 50mW was chosen to enable the mission planners to determine viewing geometries which will enable the CIRS instrument to function correctly.

A "conventional" low temperature radiative cooler design typically consists of three or more concentric stages each at a different temperature, with the detectors mounted on the central coldest stage [12, 13, 14, 15, 16]. For CIRS it is intended to make use of the low ambient temperature of the instrument (170K) to allow direct mounting of the Focal Plane Assembly (FPA) from the optics, cooled via a flexible link to the radiator. This will improve the reliability of the detector alignment over previous radiative coolers and allow easy replacement of a failed FPA. This approach gives a much larger heat load into the FPA than the simpler designs which results in the requirement of a larger radiator. The large radiator introduces problems suspending it from its support structure. Unlike conventional Earth orbiting radiative coolers the CIRS cooler does not have a well defined backload direction for reflected solar radiation or thermal emission from the planet. This precludes the use of reflective radiation shields which again results in a larger radiator area being required, but reduces the sensitivity to contamination compared to radiators which utilise specular reflecting shields.

A circular radiator (patch) is suspended from a conical support structure by low conductance metal wires in tension. The use of metal wires rather than the more conventional epoxy support bands was designed to ensure that the cooler performance is predictable under any environmental conditions encountered and that the performance will be reproduceable because of the tightly controlled manufacturing processes for metals. A number of problems were encountered with this suspension system which resulted in the design being changed to utilise a clamping system to increase the strength during launch. The design changes are discussed briefly in Appendix C.

The CIRS cooler does not make use of a separately supported second stage. Instead the patch support structure is fitted with an annular radiator in order to reduce its temperature and so reduce the heat loads into the patch.

A number of design features of the UARS/ISAMS instrument have been used in the CIRS cooler. The focal plane assembly (FPA) is mounted rigidly from a titanium alloy tripod and the FPA is connected to the cooler cold finger via a thermally conductive flexible link. The use of a flexible link will help retain the detector alignment by taking up the thermal contraction of the cold finger during cool-down, and will protect the detectors from vibrations during launch.

2.3.2 Cooler Conceptual Design

A schematic of the cooler conceptual design is shown in Figure 2-6. The following sections describe the functions of the various components in more detail.

Cooler Patch

The function of the patch is to cool the focal plane assembly by radiating heat to space. The patch is a disc formed from an aluminium honeycomb composite to minimise the mass while maintaining the rigidity of the structure.

The side of the patch which views space is required to have as high an emissivity as possible in order to maximise the power radiated to space. It is well known that the emissivity of a surface is increased if the surface is textured rather than being smooth [41]. The two most common forms of texturing for radiators are V-grooves and honeycomb

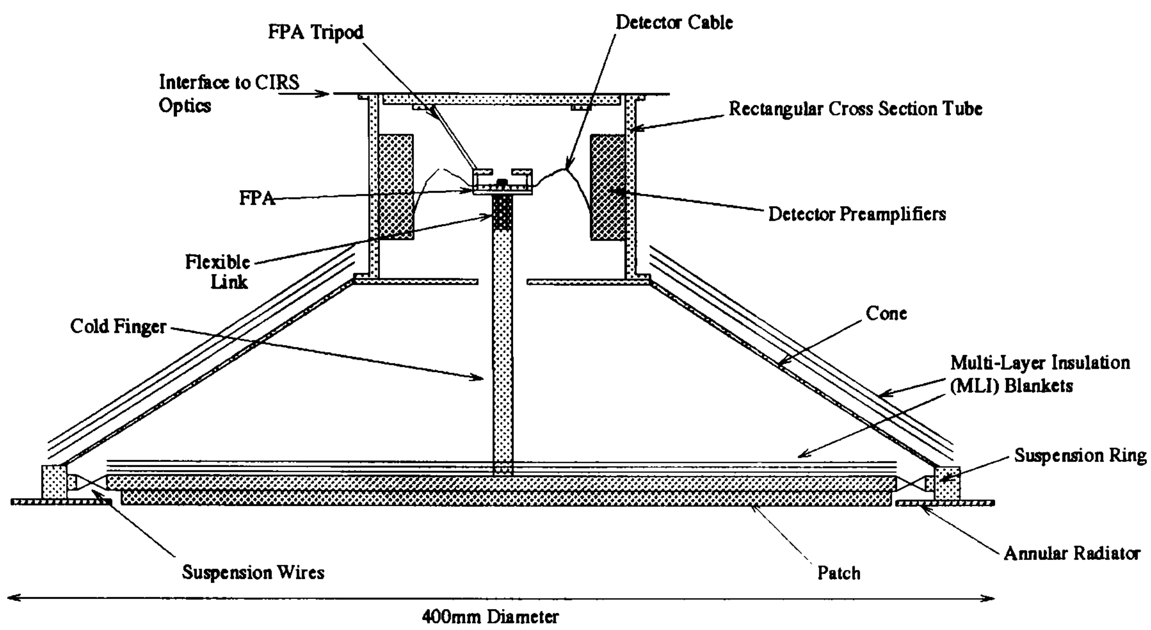

Figure 2-6: Cooler Conceptual Design

structures. A honeycomb structure was chosen for the patch front surface because the honeycomb gives slightly better thermal performance, and because with cell walls made from 0.001" thick aluminium foil, it is considerably lighter than an equivalent V-grooved surface. The honeycomb cell size was chosen to to give a cell 'diameter' to depth ratio of approximately unity because this gives close to the maximum emissivity enhancement [41].

The emissivity of the radiator is further increased by the use of black paint. There is a requirement for the Cassini mission that all external surfaces should be electrically conductive. This precluded the use of the extremely effective and well understood Nextel Black Velvet 2010 paint which was the first choice of coating because of its high emissivity (about 0.95) and the insensitivity of its emissivity to temperature [46, 47]. The space qualified electrically conducting black paint recommended by Goddard Space Flight Center (GSFC) is manufactured at GSFC and is known as MSA94B. The emissivity/temperature characteristic of the paint measured by GSFC [26] is shown in Figure 2-7. It is believed that the variation of the paint emissivity with temperature is due to changes in the wavelength distribution of the radiation being emitted as opposed to a true variation of emissivity with temperature. Unfortunately the equipment at GSFC for measuring emissivities has a minimum temperature of 170K so it was necessary to extrapolate the data to estimate the emissivity at 80K. A simple linear curve fit to the data predicted an emissivity of 0.76 at 80K. It is not at all clear that the emissivity is varying in a linear fashion so it was necessary to determine the sensitivity of the patch emissivity to the emissivity of the paint.

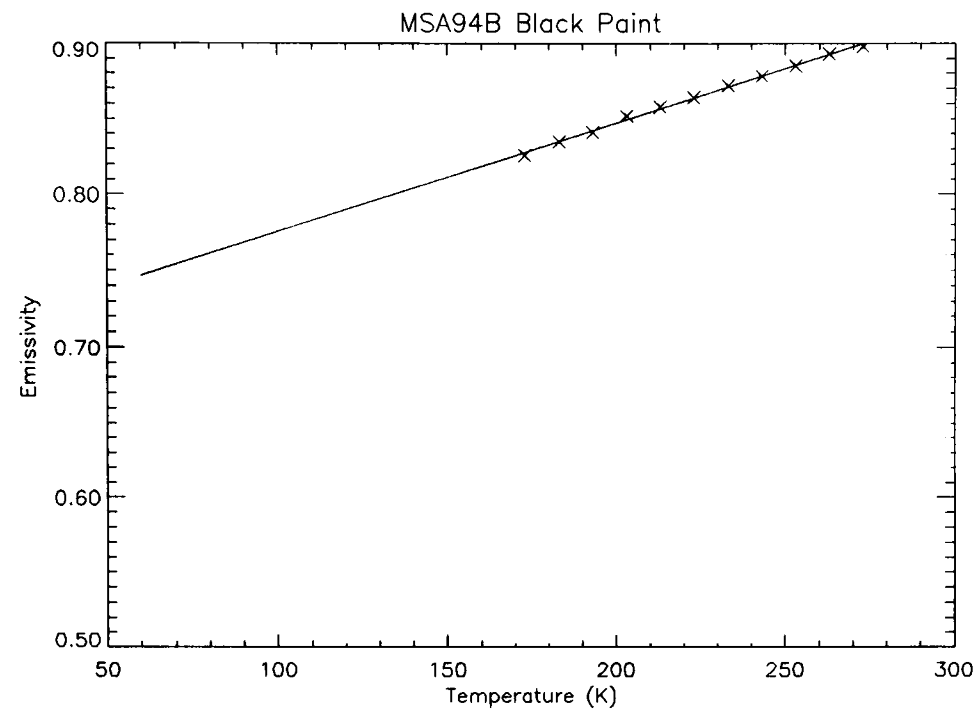

Figure 2-7: The emissivity of MSA94B black paint as a function of temperature.

A diffuse radiation model of a honeycomb cell was made using the Simplified Space Payload Thermal Analyser (SSPTA) program supplied by NASA [37]. This model was used to determine the effective emissivity of the cavity [24, 43]. The results are shown in Figure 2-8 along with data published for a similar size cylindrical cavity [41]. As would be expected the results for a hexagonal and a cylindrical cavity are similar. The model predicts that for the patch to have an effective emissivity greater than 0.90, the surface emissivity should be greater than 0.67 and that the surface emissivity must fall to around 0.4 for the patch emissivity to be reduced to 0.8. It was therefore confirmed that as would be expected the use of a textured surface reduced the sensitivity of the radiator emissivity to the surface emissivity.

The side of the patch which faces the warm cone support structure is covered with a multilayer insulation (MLI) blanket formed from a number of highly reflective shields separated by low conductivity spacers. A series of experiments were performed to determine the number of layers required and the best material for the shields. These experiments are discussed in Chapter 4.

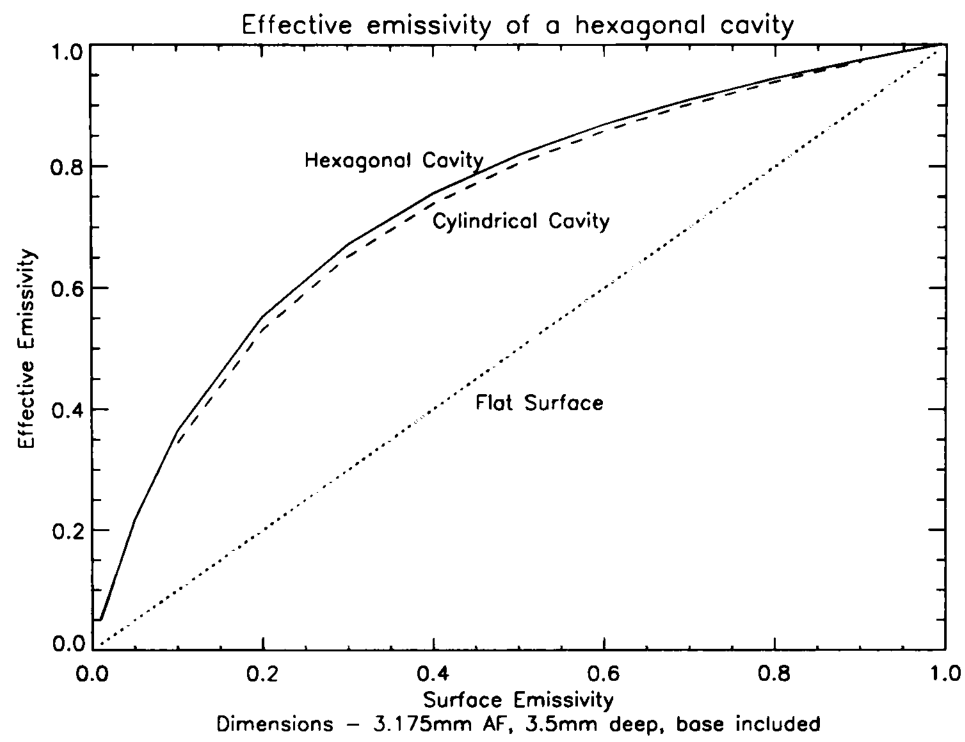

Figure 2-8: The effective emissivity of the patch honeycomb cells as a function of surface emissivity (see text).

Support Structure

The cooler support structure is formed from a cone frustum shell with a rectangular cross-section tube at the instrument (small) end. The patch end of the cone is fitted with an annular radiator in the same plane as the cooler patch in order to reduce the temperature of the cone, and hence the parasitic heat leaks into the patch. The cone is manufactured from titanium alloy (IMI-318) by super-plastic forming. IMI-318 was chosen because of its good mechanical properties and low thermal conductivity. The inside of the cone is gold plated and the outside covered with a multi-layer insulation (MLI) thermal blanket to minimise the heat loads into the cold stage.

The preamplifiers for the detector signals are mounted within the rectangular cross-section tube section and are well thermally coupled to the tube sides in order to minimise the heating of the cold stage due to the power dissipation within the amplifiers.

The annular radiator which is attached to the large end of the cone has the effect of cooling the end of the cone section to around 140K and so reduce the radiative and conductive load onto the patch back.

Patch Suspension

The original design for the patch suspension system was for the cooler patch to be suspended from the support structure by six pairs of thin titanium alloy (IMI-318) wires in tension. Titanium alloy wires were used in favour of the more conventional fibreglass support bands [15, 16, 17, 22] because the variation of material properties between batches is considerably less for metals than composites and there was a policy to minimise the use of polymers in the cooler to reduce the risk of contamination.

A number of problems were encountered with one or more wires failing under vibration because of a poor surface finish on the wires. The vibration test requirements for instruments on the spacecraft were later raised so the design was changed to utilise a clamping system to protect the suspension during launch. The design changes are summarised in Appendix C.

Cold Finger

The cold finger is a solid aluminium alloy (6061-T6) rod which conducts the heat generated in the focal plane assembly to the cooler patch. It is gold plated in order to reduce the radiative heat load from the warm support structure. The cold finger is connected rigidly to the patch at one end and to the FPA common carrier via a conductive flexible link at the other.

The flexible link is a development of the design used on the UARS/ISAMS instrument. It is formed from a bundle of 2200 copper wires which are 50μm in diameter. One end of the flexible link is soldered into the common carrier, and the other into a flange which bolts onto the cold finger.

Launch Cover

During launch and in the early part of the mission during which CIRS is inactive the patch is protected by a lightweight cover to prevent the detectors being overheated if the patch is directed towards the sun. The cover is a thin aluminium disc which is deployed using two wax pellet actuators and a system of springs. The cover is designed to release even if only one actuator operates in order to provide redundancy in the system and reduce the probability of a deployment failure.

Focal Plane Assembly

The cooler Focal Plane Assembly (FPA) houses the two detector focal planes FP3 and FP4. The configuration of the FPA is shown in Figure 2-9. The focal planes each comprise 1x10 element arrays of HgCdTe detectors mounted on separate subcarriers. The subcarriers are mounted on a common carrier which is suspended from the FPA tripod support. The common carrier and subcarriers are gold plated to reduce the radiative parasitic heat loads into the FPA.

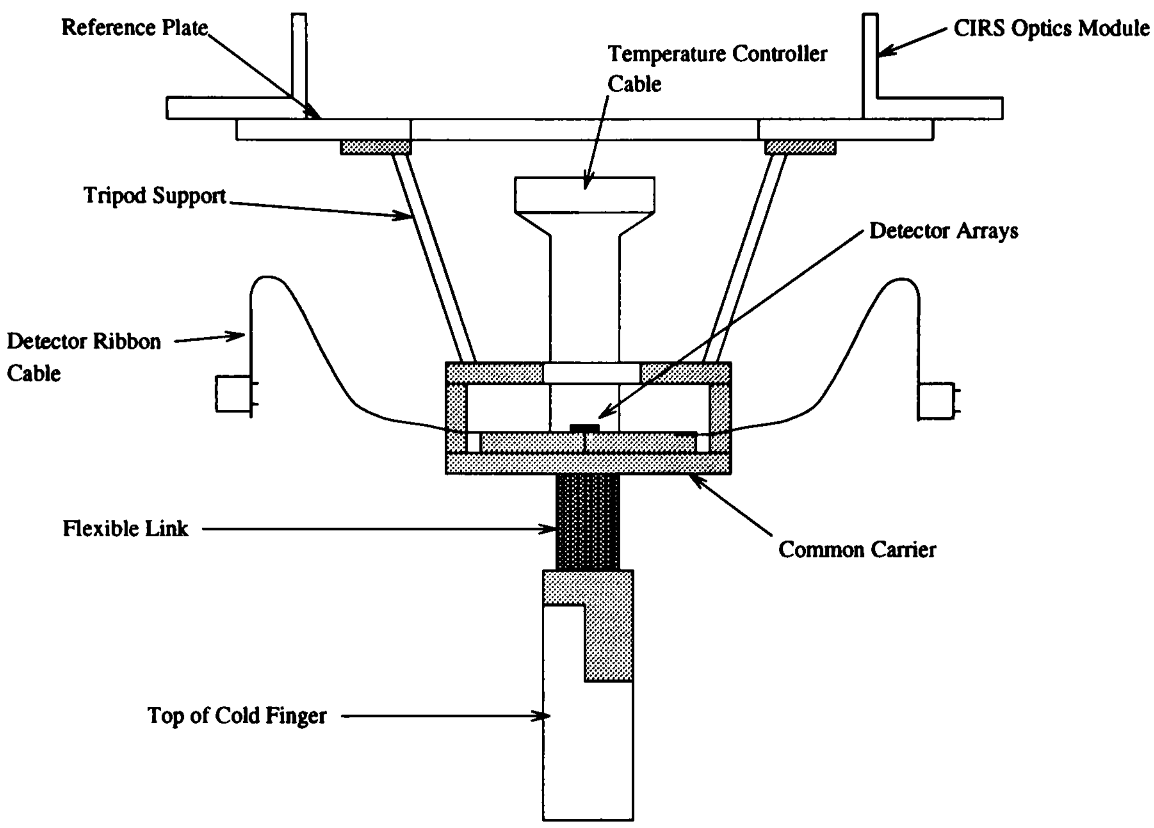

Figure 2-9: FPA Conceptual Design

Focal Plane Assembly Tripod Support

The FPA support is based upon the design used in the UARS/ISAMS instrument. The FPA is supported by a titanium alloy tripod with thin walled legs to minimise the heat leak into the FPA while maintaining the structural strength of the assembly. The base of the tripod is attached to the reference plate at the cooler/instrument interface. The tripod top incorporates an 80K cold shield to reduce the background signal to the detectors. The entire tripod is gold plated to minimise the radiative parasitic heat loads into the 80K stage.

FPA Wiring

The detector arrays FP3 and FP4 require 25 and 26 electrical connections respectively. Both of the detector ribbon cables comprise fine conductors etched from a metallic coating on a kapton (polyimide) substrate and covered with an insulating layer of kapton.

Because the resistance of the photoconductive detectors in FP3 is being measured using a two-wire technique the resistance of the cable conductors must be low so the FP3 conductors are copper. The FP4 cable conductors may have a higher electrical resistance so they are formed from a very thin (0.1μm) layer of nickel. The thermal design of the cables is discussed in Section 3.3. The manufacturing process for the FP3 cables has been developed by Ish Aslam and Tim Vellacott at Oxford. The FP4 cable has been developed by a collaborating group working at Saclay, France.

The heater for the FPA temperature controller is mounted on the back of the common carrier. It is an integral part of the cable connecting the FPA thermometers to the 170K instrument, and is manufactured in a similar way to the FP3 cable.

Chapter 3

Cooler Thermal Design

This chapter describes the thermal models which were developed to assist in the thermal design of the CIRS cooler and FPA. The models were developed as a hierarchy ranging from a very simple, analytical model which made a number of simplifying assumptions to a numerical model which incorporates a geometric radiation model of the cooler.

3.1 Model Hierarchy

Four thermal models of the cooler subsystem were developed and updated as the cooler and FPA designs matured.

- Simple Analytical Model (SAM): The baseline thermal model designed to give a conservative estimate of the cooler performance. Material properties are assumed to be constant over the operating temperature range of the components. The treatment of radiation is simplistic and consistently gives a slight over-estimate of the radiative heat loads.

- Intermediate Level Model (ILM): This model uses the same method of analysis as the SAM, but some heat loads such as the heat leaks through the detector cables for which the SAM gives unsatisfactory results have been replaced by the results from detailed thermal analysis in order to give a more accurate indication of the cooler performance.

- Simple Numerical Model (SNM): A finite difference numerical model of the cooler using a detailed node breakdown. It may be used for both steady state and transient analyses. It allows material properties to vary with temperature and uses a very simple treatment of radiation in order to make the results easily understood for model validation.

- Full Numerical Model (FNM): A complex finite difference model of the cooler using the same node breakdown etc. as the SNM, but includes a complete radiation analysis produced by a geometric model.

The purpose of the above hierarchy of models was to enable the results of the more complex models to be validated against the simpler ones at each stage of development to ensure that the complex models were physically meaningful.

3.2 The Simple Analytical Model

The simple analytical model is used to determine the heat balance of the cooler at a given focal plane temperature by the following procedure:

- Determine the temperatures of the tube, cone and annular radiator.
- Sum the heat flows into the focal plane, flexible link and cold finger.
- Determine the patch temperature by calculating the temperature drop across the cold finger and flexible link.
- Determine the heat flows into the patch.
- Subtract the total heat flow into the patch from the power radiated to space to give the excess cooling capacity of the cooler at the given focal plane temperature.

The following sections describe how the various temperatures and heat flows are calculated.

3.2.1 Thermal Conduction

Fourier's Law [24] states that the one dimensional, steady state heat flow rate between two points at different temperatures is:

$$q/A = -k\frac{dT}{dx} \tag{3.1}$$

where q is the heat flow rate between two points in a temperature gradient $\frac{dT}{dx}$. k is the thermal conductivity of the material and A the cross sectional area perpendicular to the heat flow.

In a linear temperature gradient in a material with constant thermal conductivity, k, Equation 3.1 becomes:

$$q = \frac{kA}{l}(T_h - T_c) \tag{3.2}$$

where T_h and T_c are the temperatures of the hot and cold boundaries and l is the distance between the two boundaries.

Equation 3.2 is similar to ohm's law for electricity where the *thermal resistance* (R_{th}) for one dimensional thermal conduction is given by:

$$R_{th} = \frac{l}{kA} \tag{3.3}$$

The heat flow q then becomes:

$$q = \frac{\Delta T}{R_{th}} \tag{3.4}$$

Expressions for the thermal resistance for more complex geometries in which the cross sectional area varies along the path may be derived easily by the integration of equation 3.2 along the conduction path (Appendix A). The conductive heat leaks into the cold stage of the cooler were calculated using equation 3.3 because the heat flows through components such as the tripod legs and the suspension wires will be very close to one dimensional. Only the heat flow through the cone was calculated using a more complicated expression.

3.2.2 Thermal Radiation

The total power radiated by a body at temperature T is given by:

$$q = \epsilon A \sigma T^4 \tag{3.5}$$

where q is the radiated power, ϵ is the surface emissivity, A is the surface area and T is the absolute temperature of the body. σ is the Stefan-Boltzmann constant (5.667×10^{-8}W/m^2/K^4).

If the body is surrounded by a black enclosure ($\epsilon = 1$) at a temperature T_h, the net power absorbed by the body is:

$$q = \epsilon A\sigma(T_h^4 - T_c^4) \tag{3.6}$$

where q is the net absorbed power, and T_c is the absolute temperature of the inner body.

It can be shown that equation 3.6 is also valid if the outer surface is not black provided that the inner surface is small by comparison to the outer one (Appendix B). This approximation was used to determine the radiative heat loads onto the FPA components and the cold finger.

3.2.3 Material Properties

The material thermal conductivities and heat capacities used in the models are either taken from published data [25, 18, 19, 41] or from data measured by Goddard Space Flight Center's thermal branch [26]. The thermal conductivity of the component is assumed to be constant and is taken at the mean temperature of the component.

The emissivity of a surface is highly dependent on the surface coating and texture and so is difficult to predict exactly. Most of the cold surfaces in the cooler are gold plated to give a low emissivity finish. In order to account for the uncertainty in the emissivity, a conservative estimate of the emissivity of 0.05 was used throughout [27].

3.2.4 Temperatures of Cone and Tube

Before the heat flows into the cold stage of the cooler may be determined, the temperature of the annular radiator must be determined since this provides one of the hot boundary temperatures for the heat flows into the cooler patch. In order to determine the annular radiator temperature the support structure is treated as shown in Figure 3-1.

The thermal resistance between the instrument and the midpoint of the tube section is determined using the one dimensional heat conduction equation:

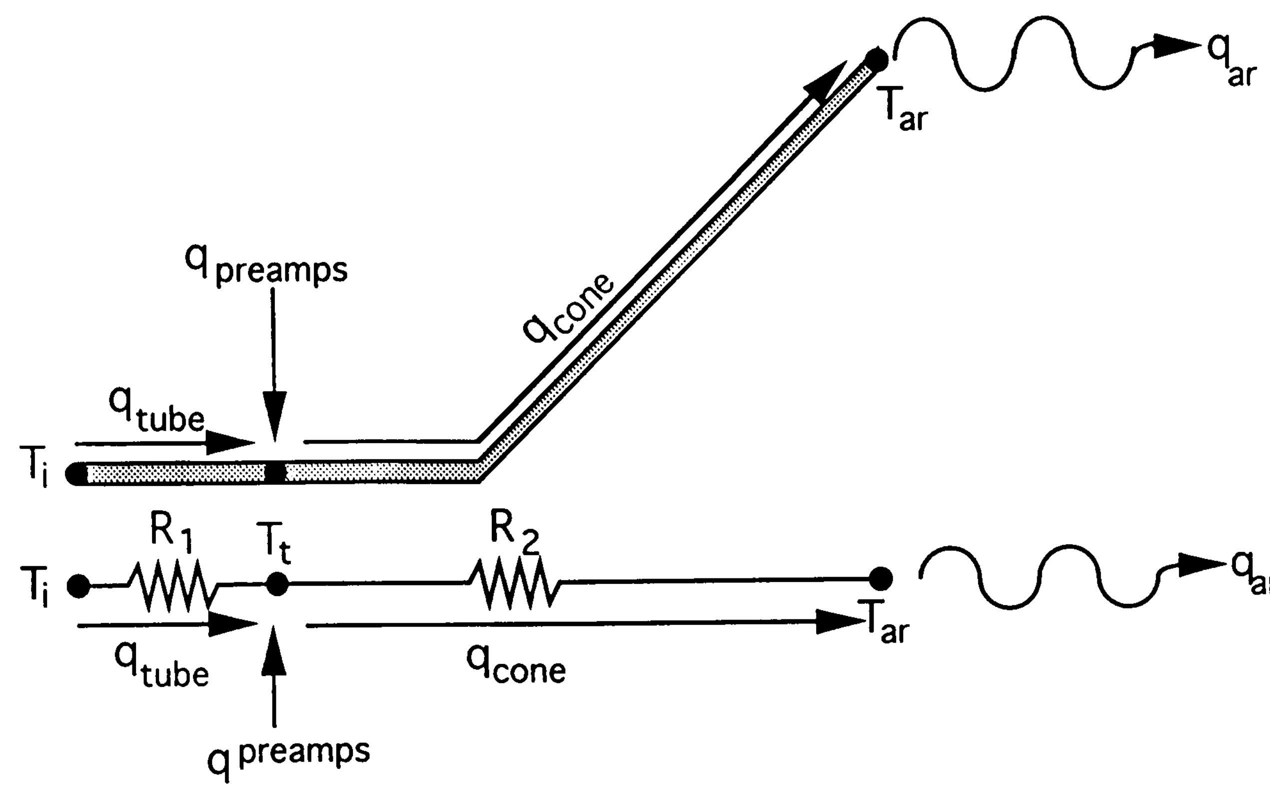

Figure 3-1: Simple representation of the cooler cone and tube — Schematic (top) with electrical analogue (bottom). T_i is the temperature of the instrument, T_{ar} is the temperature of the annular radiator and T_t is the temperature of the midpoint of the tube.

$$R_1 = \frac{l_{tube}}{2k_{tube}A_{tube}} \tag{3.7}$$

where k_{tube} is the tube thermal conductivity, A_{tube} the cross sectional area of the tube and l_{tube} the height of the tube.

The thermal resistance between the midpoint of the tube and the annular radiator is determined using equation 3.7 and the expression for radial heat conduction in a cone frustum shell which has been determined by the author:

$$R_2 = \frac{l_{tube}}{2k_{tube}A_{tube}} + \frac{\log\left(\frac{2r_2+t\cos(\beta)}{2r_1+t\cos(\beta)}\right)}{2\pi k_{cone} t \sin(\beta)} \tag{3.8}$$

where r_1 and r_2 are the inner radii at the top and base of the frustum respectively, t is the thickness of the shell, β is the cone half angle and k_{cone} the thermal conductivity of the cone material. The heat flow through the lower half of the tube and the cone (q_{cone}) is equal to the heat flow through the top half of the tube (q_{tube}) plus the preamplifier power dissipation ($q_{preamps}$):

$$q_{cone} = q_{tube} + q_{preamps} \tag{3.9}$$

inserting the expressions for the heat flows gives:

$$\frac{(T_t - T_{ar})}{R_2} = \frac{(T_i - T_t)}{R_1} + q_{preamps} \tag{3.10}$$

The power radiated by the annular radiator is $q_{ar} = \epsilon_{ar} A_{ar} \sigma T_{ar}^4$ and in thermal equilibrium $q_{ar} = q_{cone}$ which gives:

$$\epsilon_{ar} A_{ar} \sigma T_{ar}^4 = \frac{(T_i - T_t)}{R_1} + q_{preamps} \tag{3.11}$$

For given instrument temperature (T_i) and tube temperature (T_t), equation 3.10 defines the temperature of the annular radiator T_{ar}. The heat balance (equation 3.11) determines whether or not the system is in equilibrium. The assumed value of T_t is varied until thermal equilibrium is achieved. If there is an environmental radiation backload onto the annular radiator, it is subtracted from the left hand side of equation 3.11, in effect reducing the power radiated to space. The radiative heat load onto the outside of the cone from the instrument is treated in a similar manner, with the cone temperature assumed to be that of the annular radiator. The effect of the radiative heat load onto the outside of the cone is small because the cone is covered with an MLI blanket giving it a low emissivity (approximately 0.01–0.02).

This analysis neglects the effect of the heat flow between the cone and the patch (approximately 50mW). This enables the cone and tube temperatures to be determined separately from the cold stage (patch and FPA) temperatures. The effect is to slightly over-estimate the housing temperatures which will in turn result in a slight over-estimate of the heat flows into the cold stage.

Using this procedure on the cooler design for a clear view to cold space predicts the annular radiator temperature to be 142.6K for an instrument temperature of 170K with a heat load of 300mW into the tube due to the preamplifiers and the cone exposed to an environmental temperature from the instrument and spacecraft of 170K.

3.2.5 Heat Flows into the FPA

The heat flows into the focal plane assembly are calculated by assuming that the hot boundary temperature is that of the instrument (170K nominally). Conductive loads into the FPA are calculated using equation 3.3 and radiative loads are calculated using equation 3.6.

For components connecting the FPA to the tube and reference plate such as the tripod legs and cables it was assumed that the total heat leak into the FPA is equal to the sum of the conductive heat leak through the component plus the net radiative load on the component, with both values calculated independently. It is assumed that the temperature gradient is linear, and that the material thermal conductivity is constant over the temperature range of the component.

The net radiative heat load is calculated using equation 3.6 in which the temperature of the component (T_c) is taken as the 'effective radiative temperature' of the component which is calculated by assuming a linear temperature gradient along the component. The effective temperature is determined using the following expression which was derived by the author (See Appendix B):

$$T_{eff}^4 = \frac{(T_h^5 - T_c^5)}{5(T_h - T_c)} \tag{3.12}$$

Giving an effective temperature (T_{eff}) of 132.5K for a component between a hot boundary temperature (T_h) of 170K and a cold boundary temperature (T_c) of 80K.

The assumption that the conductive and radiative components of the heat leak may be summed independently is only valid for situations in which the effect of radiation is small so the temperature gradient will be very close to linear. This is the case for the tripod legs which are gold plated and have a comparatively high cross sectional area, but is not the case for the detector cables which have a very low conductance and high emissivity. For this reason two versions of the SAM heat balance have been tabulated in Table 3.4, one including the calculated net radiative heat load onto the electrical cables, and the other with the radiative load neglected. The purpose of the models developed for the intermediate level model is to improve the treatment of these components (see Section 3.3).

Example - Tripod Legs

The FPA tripod legs have an o/d of 1.05mm, an i/d of 0.80mm and the length of their narrowest section is 14mm. They are made from titanium-318 which has a thermal conductivity of 4.40W/m/K at 125K [25]. The conductive heat leak is calculated using equation 3.2 to be 10.27mW per leg.

If the emissivity is assumed to be 0.05 and the effective temperature of the leg to be 132K, the net radiative heat load using equation 3.6 is 0.07mW per leg. The total heat leak through the tripod legs is then $3 \times (10.27 + 0.07) = 31.0$mW.

3.2.6 Patch Temperature

In thermal equilibrium all of the heat flowing into the FPA must be conducted to the patch by the flexible link and cold finger. The heat flow through the flexible link is assumed to be the total heat flow into the FPA plus the net radiative load onto the flexible link wires (which are assumed to be black). The temperature drop across the flexible link is calculated using:

$$\Delta T = qR_{th} \tag{3.13}$$

where ΔT is the temperature drop across the flexible link, q the heat flow through the flexible link and R_{th} its thermal resistance as defined by equation 3.2.

The temperature drop across the cold finger is determined in a similar manner but with the addition of the net radiative load onto the cold finger. The patch temperature is then given by:

$$T_{patch} = T_{FPA} - \Delta T_{flexi} - \Delta T_{coldfinger} \tag{3.14}$$

where T_{FPA} is the assumed FPA temperature, ΔT_{flexi} is the temperature drop across the flexible link and $\Delta T_{coldfinger}$ is the temperature drop across the cold finger. The heat leak through the flexible link and the cold finger is approximately 72mW (including radiation onto the electrical cables) when the FPA is in equilibrium at 80K, giving a patch temperature of about 78.5K.

3.2.7 Heat Flows into the Patch

The conductive heat flows into the patch through the suspension wires and electrical cables are determined in a similar way to those into the FPA, but the hot boundary temperature is taken as the temperature of the annular radiator.

The net radiative loads onto the patch edges are calculated using equation 3.6 assuming that the patch edge views the annular radiator which is assumed to be a black cavity. Although this is not an accurate representation, it ensures that the model will give a conservative estimate of the cooler performance.

The net radiative load onto the patch back is calculated assuming that it views a conical cavity at a single effective temperature. The effective emissivity of the conical cavity was determined from published data [41] and it is then treated as a flat plate with that effective emissivity. The net heat load is then given by:

$$q_r = \frac{1}{\frac{1}{\epsilon_c} + \frac{1}{\epsilon_p} - 1} A_p \sigma (T_{eff}^4 - T_p^4) \tag{3.15}$$

where ϵ_c is the effective emissivity of the conical cavity (around 0.1[41]), ϵ_p is the emissivity of the patch back (0.01), A_p is the area of the patch back and T_{eff} and T_p are the effective temperatures of the cone and the patch temperature respectively.

The effective temperature for the cone is determined by assuming that there is a linear temperature gradient along the cone, then calculating an area weighted average of T^4 along the cone (See Appendix B). This gives a conservative estimate of the effective temperature because the true temperature gradient is exponential in shape because of the form of equation 3.8. The over-estimate is small because the absolute temperature change along the cone is small. The effective temperature of the cone using the above approximations is given by:

$$T_{eff}^4 = \frac{2}{r_o + r_i} \left[\frac{(r_o T_o^5 - r_i T_i^5)}{5(T_o - T_i)} - \frac{(r_o - r_i)(T_o^6 - T_i^6)}{30(T_o - T_i)^2} \right] \tag{3.16}$$

where r_i is the radius of the top of the cone frustum and r_o is the radius of the base of the cone frustum. T_i and T_o are the temperatures of the top and base respectively. For a top temperature of 168.3K and a base temperature of 142.6K the effective temperature is found to be 154.1K. Using this value in Equation 3.15 gives a calculated net heat load is 26.9mW for a patch temperature of 78.9K.

3.2.8 Heat Balance

The power radiated to space by the patch is calculated using equation 3.6 for a cold boundary temperature of 4K (cold space). The radiated power is reduced by any absorbed environmental heat fluxes. The heat imbalance is calculated by subtracting the total heat flow into the patch from the radiated power. If the imbalance is zero then the cooler is in thermal equilibrium at the focal plane temperature assumed at the beginning of the process. If the imbalance is positive then there is a net flow of heat out of the system and the assumed FPA temperature must be reduced. Conversely if the imbalance is negative then the FPA temperature should be increased and the process repeated until the thermal equilibrium temperature is found.

If it is not necessary to find the equilibrium temperature, but merely the excess cooling capacity at the chosen FPA temperature, then the heat imbalance is simply the amount of heater power or environmental backload which may be tolerated without the FPA temperature increasing above the assumed value. The cooler specification requires this value to be at least 50mW to account for environmental heat fluxes from the planet or the rings during operation.

3.2.9 Results from the Simple Analytical Model

Radiator Area

The simple analytical model was used early in the project to determine the patch radiating area required by calculating the model for various areas and determining the cooling capacity. The diameter was chosen to achieve the target of 50mW excess cooling at 80K with the FPA installed. The area of the radiator is just under 0.1m^2 giving a total cooling power of slightly less than 190mW at 78K.

Heat Load Sensitivity

The heat load sensitivity of the combined cooler and FPA was determined by calculating the equilibrium focal plane temperature for various heat loads into the patch. The model was run both as described above and with the radiative loads onto the electrical cables neglected (since these are grossly over-estimated by the SAM - see Section 3.3). The results are shown in Figure 3-2. The heat load sensitivity is the gradient of the curve at a given temperature and was found to be 0.09K/mW for the model which included detector cable radiation, and 0.10K/mW for the model which neglected detector cable radiation. Both calculations were for a FPA temperature of 80K. The sensitivity calculated for the model which included the extra radiation was slightly smaller than the model which neglected it because adding the extra radiation terms increases the temperature of the patch. Because the power radiated (q) is proportional to T^4, $\frac{dq}{dT}$ is proportional to T^3, so the heat load sensitivity $\frac{dT}{dq}$ is proportional to $1/T^3$, so the sensitivity decreases as the patch temperature increases.

The heat load sensitivity is a useful parameter for quickly assessing the effects of design changes which will involve additional heat loads because it enables a new patch temperature to be estimated easily.

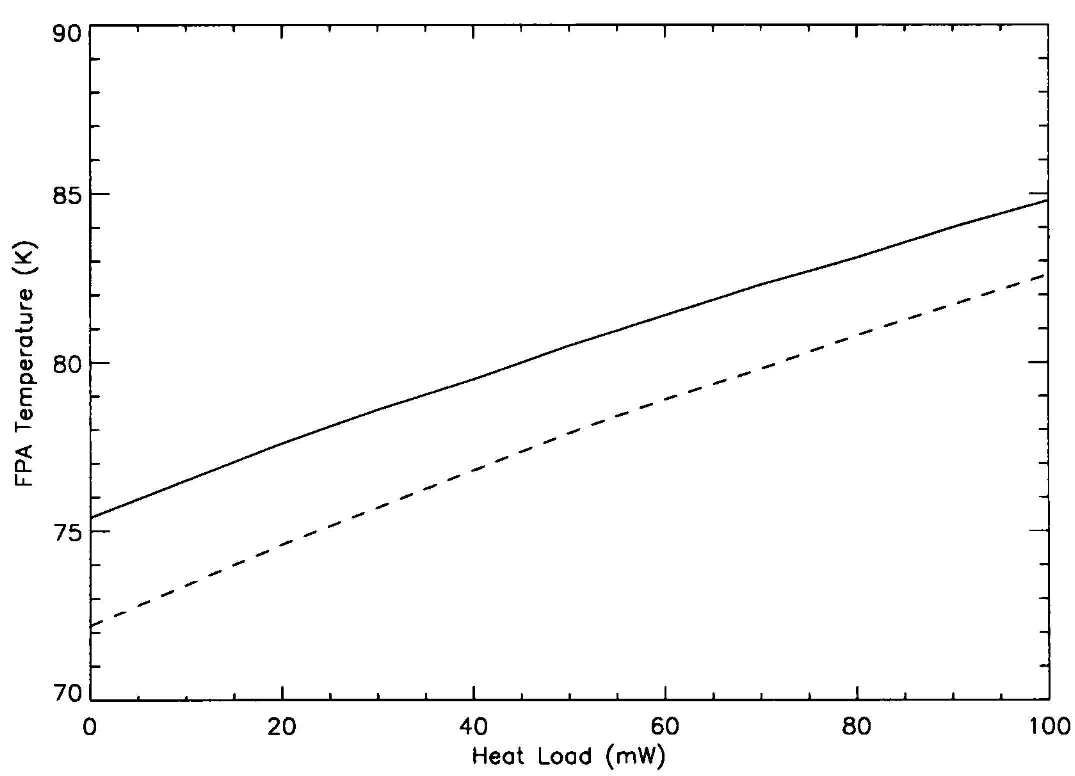

Figure 3-2: Variation of the FPA tempearature with heat load into the FPA. The solid line is the SAM with the radiative load onto the electrical cables included. The dashed line was calculated by neglecting the radiative load onto the cables.

Sensitivity to Instrument Temperature

The variation of the FPA temperature with instrument temperature was determined by calculating the equilibrium FPA temperature for various instrument temperatures. The SAM was calculated both with and without including radiative heat loads onto the electrical cables. The results are shown in Figure 3-3.

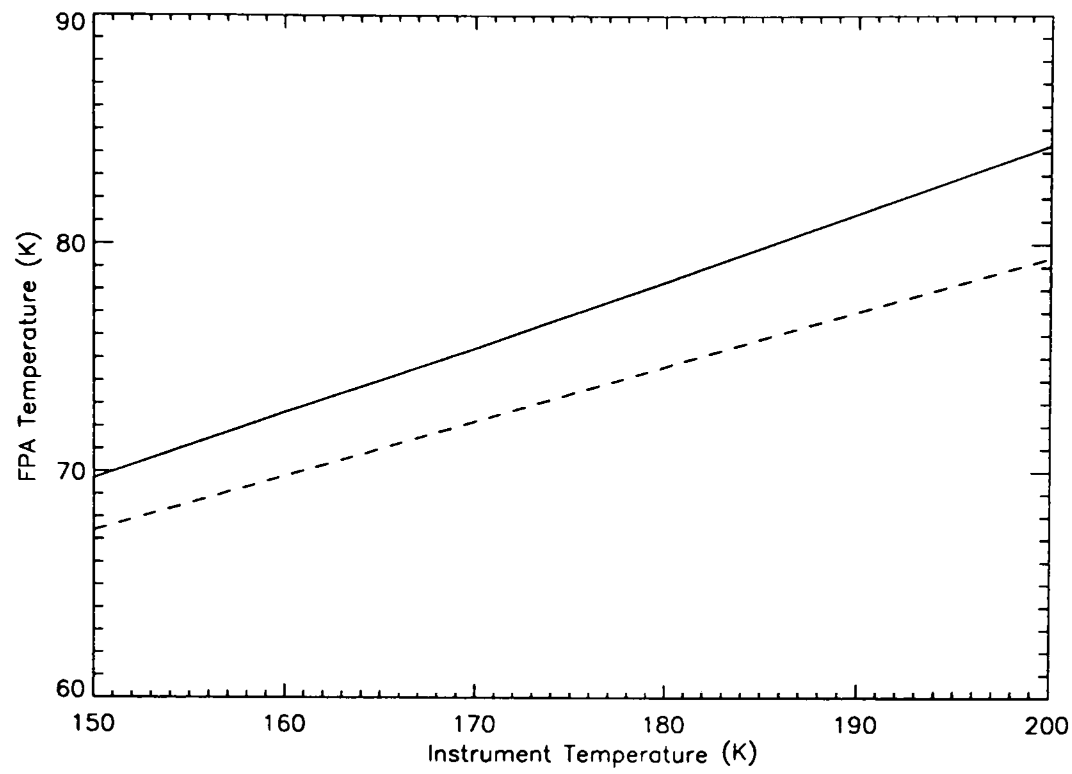

Figure 3-3: Variation of the FPA temperature with instrument temperature using the SAM which included radiation onto the electrical cables (solid line) and neglected radiation onto the electrical cables (dashed line).

The calculated values of the sensitivity of the FPA temperature to the instrument temperature were 0.291K/K for the SAM which included radiation onto the electrical cables, and 0.240K/K if the radiation was neglected.

Using the same model results it is possible to plot the variation of the FPA temperature with annular radiator temperature as shown in Figure 3-4. The sensitivity of the FPA temperature to annular radiator temperature was found to be 0.585K/K for the model including radiation on to the electrical cables and 0.482K/K for the model neglecting the cable radiation.

Heat Balance

The calculated heat balance at 80K is summarised later in Table 3.4 on page 62 along with the results from the more sophisticated models. The two versions of the SAM (with and without the detector cable radiation) are included for comparison. It can be seen that the largest single heat load is the FPA tripod. The tripod is the structural support for the FPA which ensures detector alignment so it is not envisaged that this heat load will be reduced by making the legs thinner because to do so could compromise the mechanical strength of the structure.

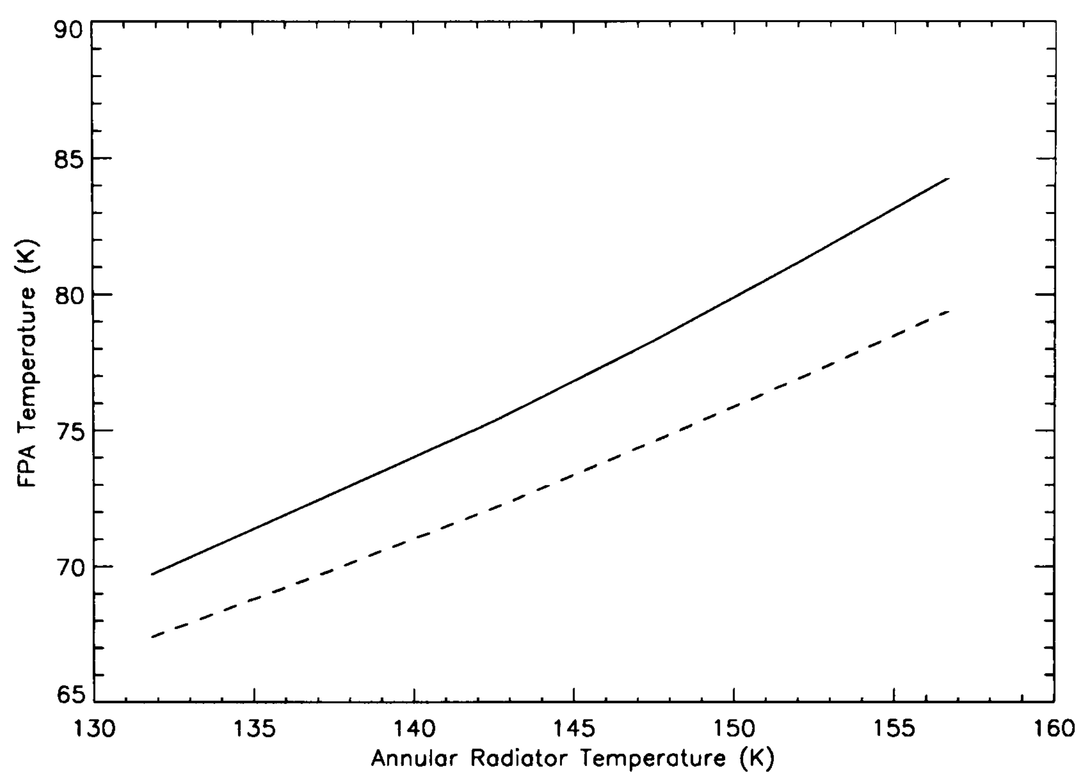

Figure 3-4: Variation of the FPA temperature with annular radiator temperature using the SAM which included radiation onto the electrical cables (solid line) and neglected radiation onto the electrical cables (dashed line).

The second largest heat leak is the radiative load on to the patch back. The emissivity of the patch back MLI blanket is assumed to be 0.01 so it is very unlikely that the performance of the blanket could be improved beyond that figure (See Chapter 4 for details of the experiments performed on the MLI blankets).

The reason for the large difference in the cooling power at 80K between the two versions of the SAM is that the radiative loads onto the cables increase the heat load through the flexible link and patch, so the FPA to patch temperature drop is increased, resulting in a lower patch temperature and hence lower radiated power in addition to the increased heat load through the cables. Comparison with the more detailed models described below shows that the SAM which does not include the radiation onto the electrical cables gives the best agreement with the more detailed models which are the "best estimate" of the cooler performance.

3.2.10 Decontamination Heater Power

During operation it may be necessary to decontaminate the cooler and FPA by raising the FPA temperature to 300K. This is achieved using a heater on the cold finger. The power required was determined using the simple analytical model with the material properties changed to account for the new operating temperatures. It was found that the patch temperature would be raised to approximately 240K with a heater power of 18W. The FPA temperature achieved can be varied by changing the position of the heater on the cold finger because the temperature drop along the cold finger is changed. Positioning the heater on the cold finger approximately 20–25mm from the patch will give a FPA temperature of 300K. The required position of the heater was confirmed later using the simple numerical model of the cooler.

3.3 The Intermediate Level Model

As was stated previously, the intermediate level model (ILM) of the cooler is the simple analytical model with the heat leaks through certain components replaced by the results of detailed numerical thermal analysis.

The components which have been replaced in the ILM are:

- The FP3 (PC) detector cable.
- The FP4 (PV) detector cable.
- The temperature controller cable.
- The patch thermometer cable.

Detailed models of other components (such as tripod legs, suspension wires etc.) have been produced, but the results obtained were very similar (<0.2mW difference) to those produced by the SAM so the SAM results were used instead. The following sections describe the models and their results in detail.

3.3.1 The FP3 Detector Cable

Cable Design

The FP3 detector cable provides the electrical connections between the FPA and the preamplifiers in the cooler tube for the 10 detector elements in FP3 and two silicon diode temperature sensors on the detector arrays. A total of 25 conductors are required including a separate ground conductor. The design of the cable is summarised in Table 3.1.

The design of the cable is driven by the electrical specification - a maximum resistance of 10Ω is allowed (10% of the nominal detector element resistance). This requires a minimum conductor size for a given material and length of cable. To minimise the heat leak down the cable, the maximum thermal resistance consistent with an electrical resistance of 10Ω is required.

In order to make a choice of material for the conductors a figure of merit must be determined. Since a material with a high electrical conductivity but low thermal conductivity is required the figure of merit chosen was the product of the thermal conductivity (k) and the electrical resistivity (ρ). A "good" material in this context should have a low value of kρ. Table 3.1 shows the values of kρ for various common conductor materials. The values of thermal conductivity and electrical resistivity used in the table are at a temperature of 130K since this is the mean temperatures of the conductors during operation. The table clearly shows that of the commonly available conductor materials copper has the lowest value of kρ so pure copper was chosen as the prefered conductor material.

In general pure metals are better than alloys as indicated in the table. Because pure metals have high thermal conductivities they require the tracks to be very thin which can produce manufacturing problems which is why alloys such as constantan are often used in cryogenic systems. In this case the track dimensions required are within the capability of the manufacturing process used.

Table 3.1: Comparison of various conductor materials at 130K

Material	k [25] (W/m/K)	ρ [18] ($\times 10^{-8}\Omega$ m)	kρ ($\times 10^{-6}$WΩ /K)
Copper	450	0.53	2.39
Nickel	156	1.7	2.65
Gold	339	0.87	2.95
Constantan	17.7	46	8.14

The electrical specification that the individual conductor resistances should not exceed 10Ω determines the cross sectional area of the conductors given that the conductor length is 40mm. The required cross sectional area was found to be 2.12×10^{-11}m^2 using the material properties given in the table. This area corresponds to an equivalent circular wire diameter of around 5μm which is too fine to be practical, so a ribbon cable was

Table 3.2: Summary of the FP3 Detector Cable Design

Number of Conductors	25
Conductor Width	35.3μm
Conductor Thickness	0.6μm
Length of narrowest section of cable	40mm
Width of narrowest section of cable	3.2mm
Thickness of kapton substrate	75μm
Thickness of kapton insulator	25μm
Surface Finish	Bare Kapton

designed in which rectangular cross section conductors were etched from 0.6μm thick copper deposited on a 75μm thick kapton (polyimide) substrate. A 25μm thick kapton insulating layer was glued over the conductors after etching. The development work needed to manufacture the cables was carried out by S Aslam and T Vellacott at Oxford. The design of the cable is summarised in Table 3.2.

Cable Thermal Model

The thermal models of the FP3 ribbon cable assume the length of the cable to be 32.4mm. This is the length of the section of the cable where the conductor tracks are narrowest rather than the full length of the cable.

The numerical model of the ribbon cable was written using the ESATAN thermal analysis package[36]. The model divides the cable up into a number of *sections* along its length, with each section containing five nodes as shown in Figure 3-5. In each section a single node represents the conductors and two more the bulk of the substrate and insulator layer. The two outer nodes are on the outside of the substrate and insulating layers to ensure that the treatment of radiation is accurate - they represent the surface temperature rather than the bulk temperature of the material.

The thermal conduction between nodes within the cable is calculated using Fourier's law (equation 3.2). The material thermal conductivity is calculated using linear interpolation of the tabulated data published in [25] which has been entered into a database file.

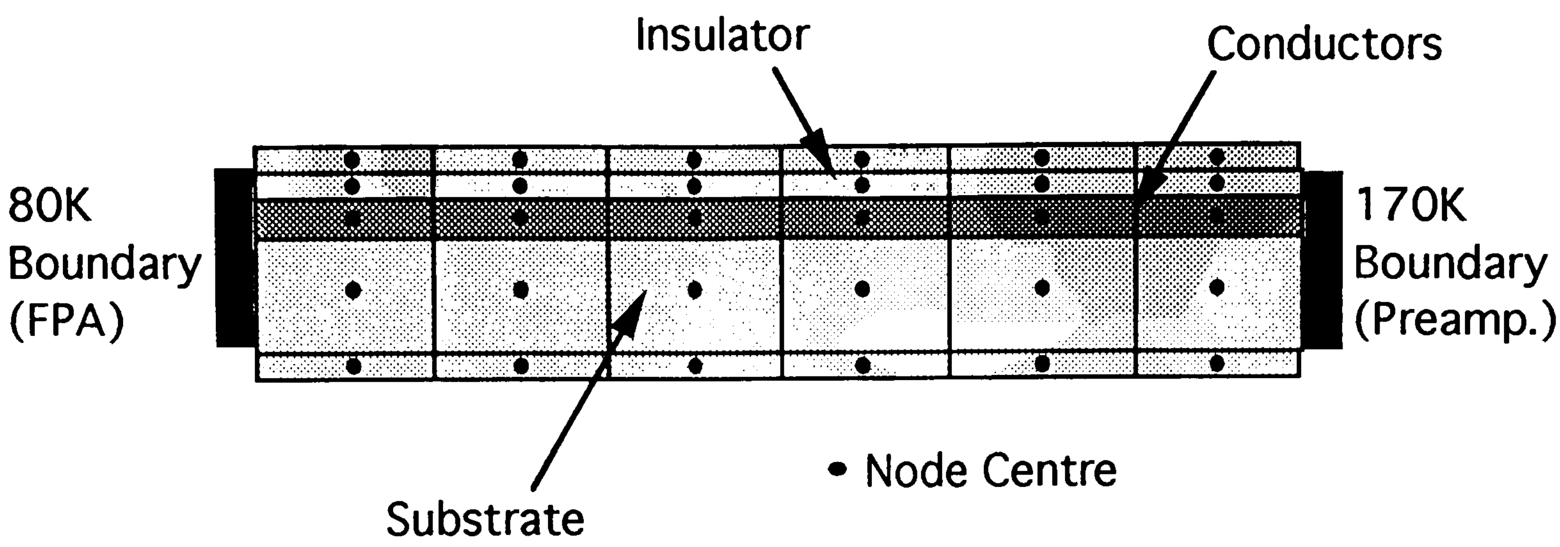

Figure 3-5: The PC Cable Numerical Model

The ends of the cable are connected to boundary nodes at 80K and 170K representing the FPA and instrument respectively. The outer nodes of each section are radiatively connected to the hot (170K) boundary node by assuming that it forms a black cavity. It is possible to set the detector bias current in the model, in which case an internal heat load is calculated for each conductors node equal to the joule heating within the conductors. The temperature distribution along the cable is essentially unchanged over the range of bias currents envisaged for normal operation. The model is solved for temperature and heat leak into the cold boundary node using the matrix inversion solution routine provided with the ESATAN package.

Results

The effect of model resolution was investigated by varying the model resolution and recording the heat leak into the FPA which the model predicted. The results are shown in Figure 3-6. The figure clearly shows that very little improvement in the accuracy of the model is gained for running the model at resolutions above 20 sections – the difference in predicted heat leak between the 20 section model and the 25 section model is less than 0.01mW.

Initially the model was verified by switching off the radiation (setting the cable emissivity to zero) and setting the bias current to zero. In this case the heat leak predicted by the model showed good agreement with the simple analytical model - The SAM predicts a heat leak of 0.67mW through the conductors plus a further 0.14mW through the kapton giving 0.81mW in total. This is very close to the 20 section numerical model's value of 0.82mW which takes into account the variation of the thermal conductivity of the conductors with temperature.

With boundary conditions of 170K and 80K, the 20 section model predicts a heat leak into the FPA of 3.2mW during normal operation (detectors on). This compares to a value of 6.4mW for the SAM using the radiation treatment described above. The large difference between the two models is caused because the SAM assumes a linear temperature gradient to calculate the net radiative heat load whereas the numerical model allows the temperature profile to vary along the length of the cable, giving a more accurate calculation of the radiative heat loads onto the sections of the cable.

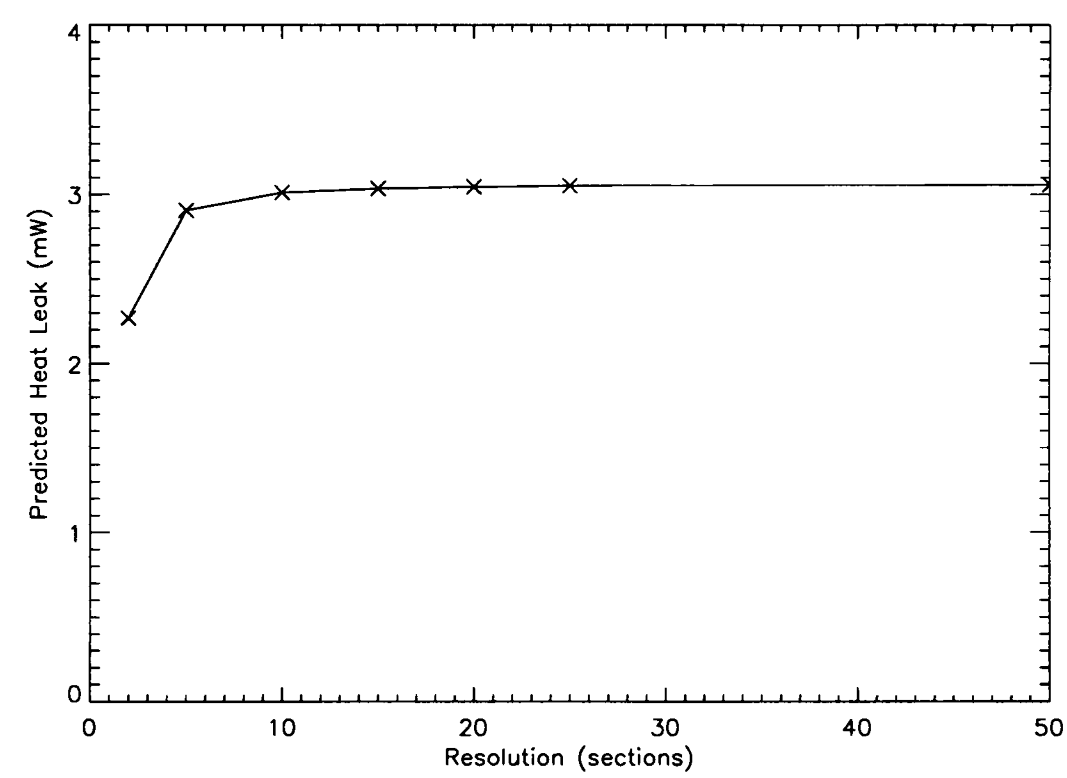

Figure 3-6: The effect of model resolution on the heat leak predicted by the FP3 detector cable model

3.3.2 The FP4 Detector Cable

Cable Design

The cable connecting the FP4 detector array to its preamplifier is very similar to the FP3 cable described above. A group working at Saclay, France were responsible for the design and procurement of the cable. They chose 37 nickel conductors 0.1μm thick by 50μm wide. The overall width of the cable is 6mm and its length is 30mm. The cable is formed on a kapton substrate with a kapton insulation layer in a similar manner to the FP3 cable. The cable surfaces were bare kapton as opposed to gold coated.

Cable Model

The numerical model of the FP4 Detector ribbon cable is simply a copy of the FP3 cable model discussed above with the material properties and geometry changed. An investigation was performed to determine whether any benefit would be gained by adding gold layers to the cable. At the time of the investigation the design detailed above was not available so the model was run using both fine gold conductors and thicker constantan conductors in order to demonstrate the effect of adding gold layers onto different cable types.

Results

The model was solved for four potential designs of cable:

1. 5μm square gold conductors with complete gold layer.
2. 5μm square gold conductors without gold layer (bare polymer surface).
3. 10μm square constantan conductors with complete gold layer.
4. 10μm square constantan conductors without gold layer (bare polymer surfaces).

Where present the gold layers were assumed to be 0.25μm thick and have an emissivity of 0.05. The bare polymer surfaces were assumed to have an emissivity of 0.9. The heat leaks into the FPA were calculated to be:

Configuration	Heat Leak (mW)
Gold conductors, no gold layer	4.52
Gold conductors with gold layer	4.21
Constantan conductors, no gold layer	2.44
Constantan conductors with gold layer	3.22

The above results show good agreement with the analytical model predictions — The models agree to better than 5% for the cases with gold layers present and so the analytical model is valid (because the radiation term is small compared to conduction).

The temperature profiles shown in Figure 3-7 confirm that the assumption of linear temperature gradients used in the SAM is valid for gold coated cables.

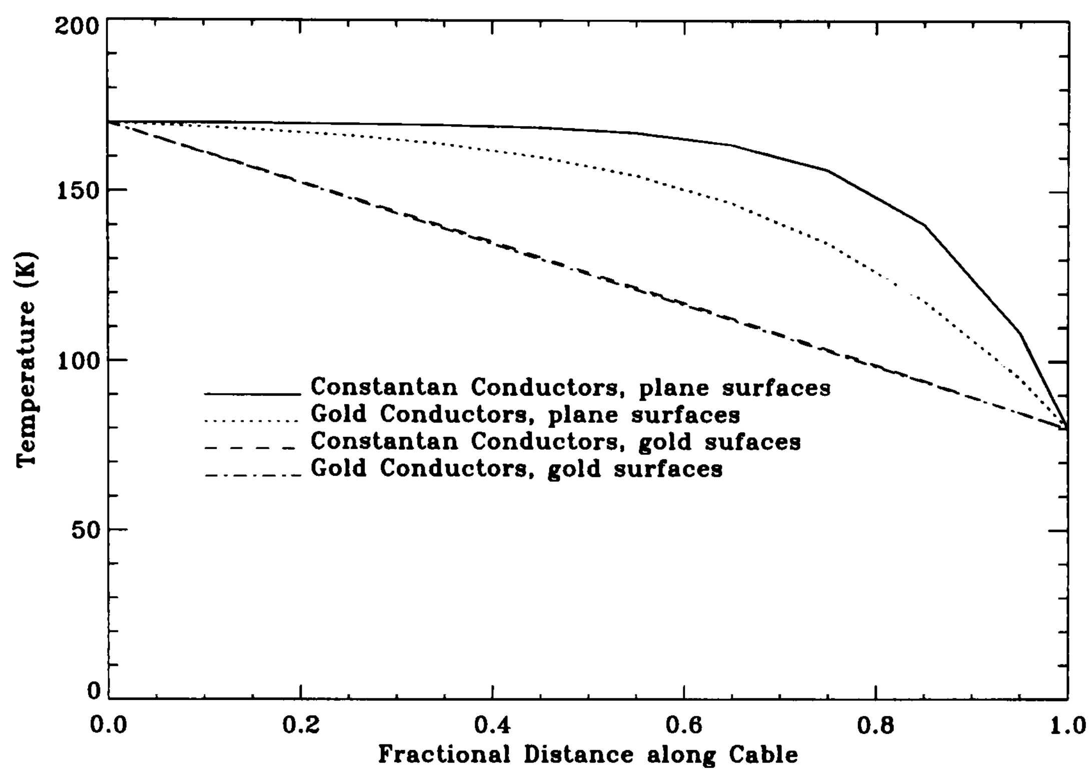

Figure 3-7: Temperature profiles along FP4 detector ribbon cable models

An interesting result is that adding gold layers to the surface of the gold-conductor cable tends to decrease the heat leak into the FPA, whereas the gold layers increase the heat leak through the constantan-conductor cable. This is because adding the gold layers has the effect of forcing the temperature profiles close to linear by reducing the net radiative load into the cable, and hence reduce the magnitude of the temperature gradient at the focal plane end of the cable (see Figure 3-7). The heat flow into the focal plane is proportional both to the temperature gradient and to the thermal conductivity of the cable, so flattening the gradient reduces the heat leak into the FPA. However adding the gold layer adds in a heat leak through the gold, so there is a trade-off between the reduction in conduction due to the flattening of the profile and the addition of the conduction through the gold layers.

The constantan conductors have a very low thermal conductivity, resulting in a small heat leak through the conductors even under the steep temperature gradient. The reduction in the heat leak through the conductors because of the flattening of the gradient is less than the conduction through the gold layers, resulting in a net increase in the heat leak.

The heat leak due to gold conductors is much more significant under the steep temperature gradient, and the reduction in this heat leak caused by flattening the gradient by adding gold layers is larger than the heat leak through the gold layers, resulting in a net decrease in the heat flow into the FPA. Using the results of this investigation it was decided that there would be no benefit in adding gold layers to the PV detector cable since the thermal resistance of the nickel conductors in the real cable is similar to that of the constantan conductors studied above.

Once the dimensions of the actual cable design were available and the model was altered accordingly, the heat leak through the nickel conductor cable was predicted to be 2.1mW with the FPA at 80K and the tube at 170K. This shows good agreement with the model developed independently by P.Lavocat at Saclay [28] who predicted a heat leak of between 2mW and 3mW under the same conditions. The results from the SAM for this design of cable were 0.4mW neglecting radiation or 10.1mW when the radiation term was added. This again demonstrates the inadequacy of the SAM to predict the radiative component of the heat leak through components which have non-linear temperature profiles. The two SAM results do however bracket the results of the numerical model which increases confidence in the results of the numerical model.

3.3.3 Patch Cable

Cable Design

A cable is required to connect between the patch and the suspension ring in order to provide connections for the patch thermometer and the decontamination heater. The construction is similar to the FP3 detector cable, but the heater conductors are considerably wider to prevent them burning out when they are carrying the current for the decontamination heater.

Cable Model

The model is again similar to the FP3 detector cable model, but with a slight change to account for the conductors having different widths. During operation with the decontamination heater off the model predicts a heat leak of 6.3mW.

With the decontamination heater on the cable carries a current of 600mA. Under these conditions the model predicts that the conductors will reach a temperature of 483K. This is well within the maximum recommended operating temperature of the kapton substrate of 672K [41].

3.3.4 Temperature Controller Cable

The temperature controller cable is of similar construction to the FP3 detector cable, but because it only has 6 conductors they are slightly wider to increase the manufacturing yield. This has only a small effect on the total heat leak through the cable because the heat leak is dominated by radiation onto the cable rather than conduction though it. The FPA end of the cable has the temperature controller heater built in by forming a fine zig-zag pattern in the copper conductor to give a long resistance path. The model is similar to the FP3 model and predicts a heat leak of 2.2mW during normal operation.

3.3.5 SAM-ILM Model Comparison

Table 3.4 shows the comparison of the heat balances of the cooler and FPA calculated using the SAM and ILM. The only differences are in the calculated heat leaks through the electrical cables which have been replaced by the ILM results described above. The table shows that for the detector cables and the temperature controller cable, the SAM which neglected the detector cable radiation shows the closest agreement to the numerical results calculated in the ILM. The patch electrical cable model shows better agreement with the SAM which included the radiation onto the cable. This is because the patch cable contains two large conductors for the decontamination heater which force the temperature profile close to linear so the SAM radiation treatment is more accurate than for the cables which show less linear profiles. The cooling power at 80K of 62.5mW meets the 50mW minimum cooling capacity specification agreed with the instrument developers.

The analysis of the cables showed that the cables could have been made shorter without a thermal penalty, but the manufacture of the cable and the assembly of the cooler would have been considerably more difficult in that case so the lengths of the cables were not reduced from those described above.

3.4 Simple Numerical Model

3.4.1 Description

The numerical model of the cooler and FPA is a simple finite difference representation of the assembly. The model is written using the ESATAN thermal analysis package [36] which was written for the European Space Agency.

The main component parts of the cooler are represented using general purpose routines which were written to produce sub-models of simple geometric shapes by generating a node mesh at a given resolution and connecting the nodes together using conductive shape factors calculated by the author for the specific geometry. The derivation of the conductive shape factors is given in appendix A. The code to generate the sub-models is written in a FORTRAN-like programming language which is integrated into the ESATAN analysis program. The model of the cooler is an assembly of sub-models as defined in Table 3.3.

Patch

The cooler patch is represented by four sub-models as shown in Figure 3-8. The back of the patch and the radiating surfaces are represented by seven node circular plates (PATCHBCK & PATCHRAD). The edge of the patch is represented by a four node cylindrical shell (PATCHSID) and the area between the radiator and the edge of the patch by a four node annulus (PATCHANN). The cold finger is represented by a 5 node solid cylinder (COLDFINGER).

Cone

The cone and suspension ring are represented by three sub-models as shown in Figure 3-9. The cone top is represented by a four node annulus (RADSHIELD), the main body of the cone by a six node cone (BELL) and the suspension ring by a four node cylindrical shell (SUSPRING).

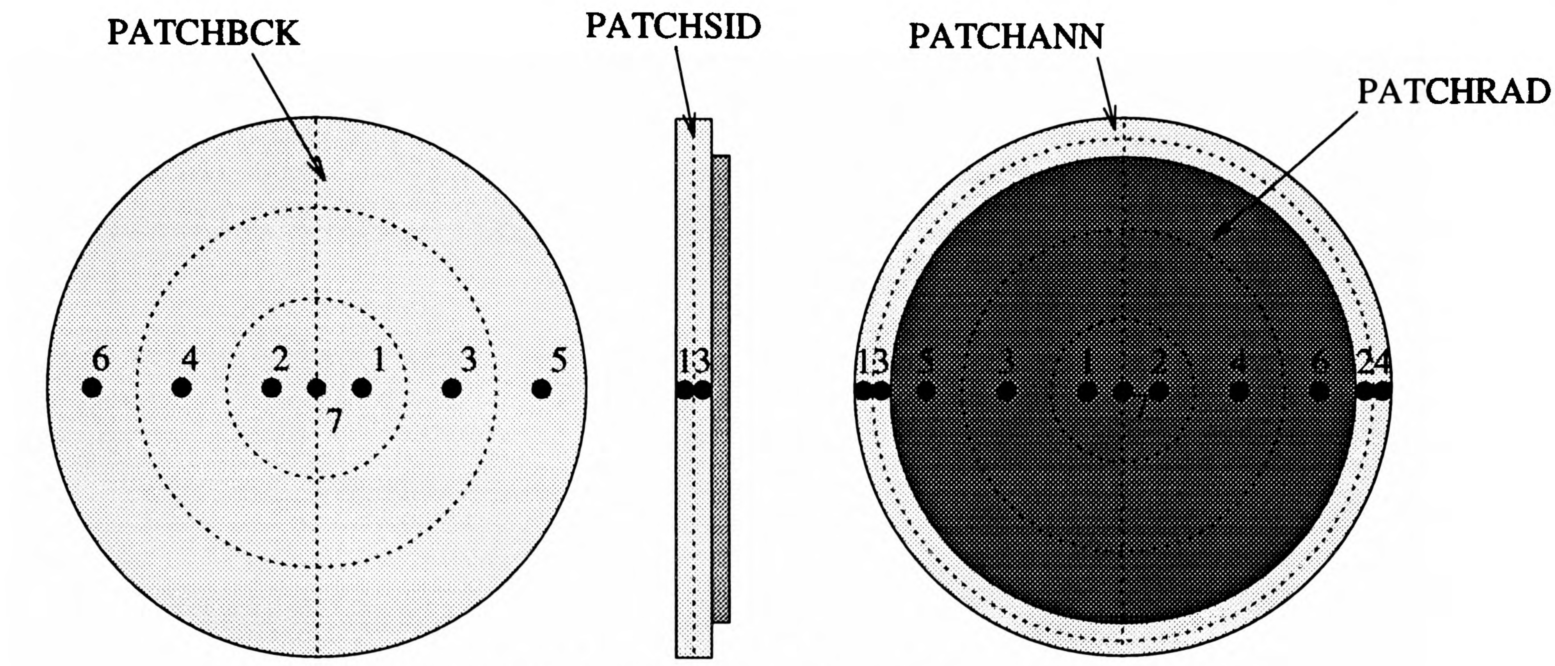

Figure 3-8: Node break down of the cooler patch.

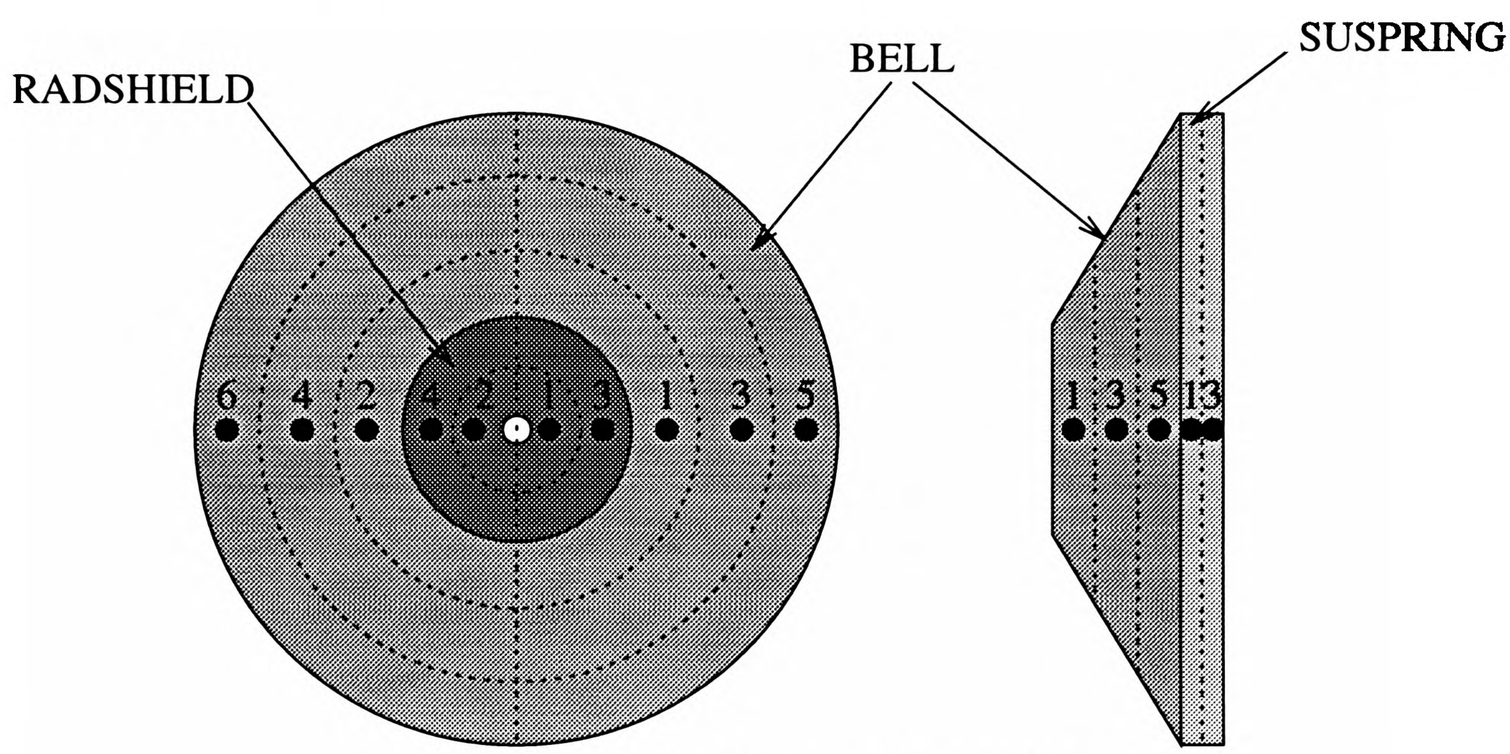

Figure 3-9: Node break down of the cooler cone.

Tube

The rectangular cross section tube is represented by four rectangular plates as shown in Figure 3-10. Each side of the tube is represented by a nine node rectangular plate.

Focal Plane Assembly

The focal plane assembly is formed from seven nodes representing the common carrier, the two subcarriers, the tripod top, the flexible link wire bundle and the flexible link base. The three tripod legs are represented by a single node.

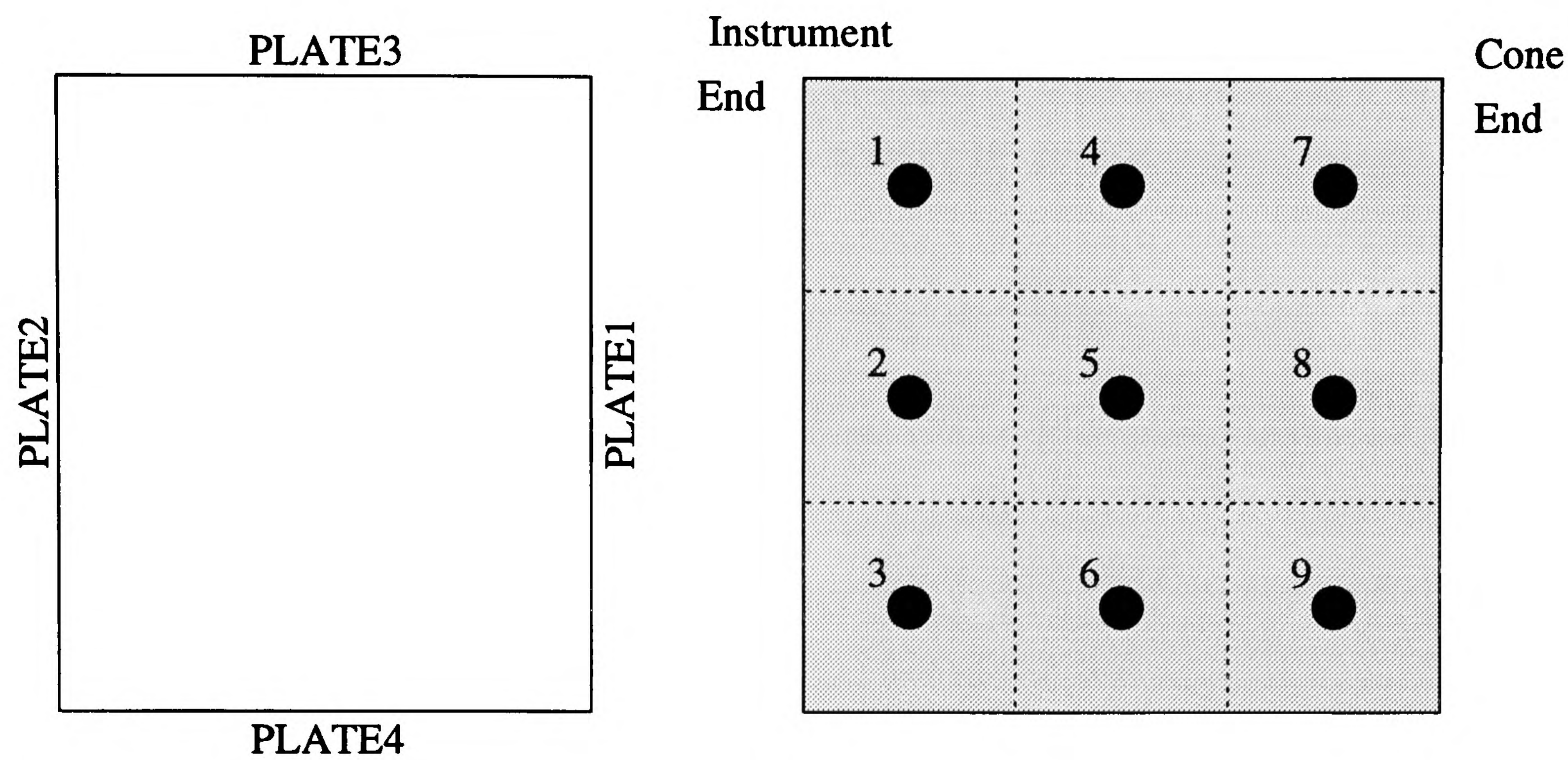

Figure 3-10: Node break down of the cooler tube.

Main Model

The main model connects the sub-models together to form a model of the whole cooler. The main model also contains the code necessary to define the type of solution required (transient or steady state) and the boundary conditions. The cooler numerical model is summarised in Table 3.3.

The various sub-models are connected together conductively by defining conductors between the outer nodes of the sub models to be connected. Thermal contact resistances were assumed to be small but could be added if they were found to be significant during testing.

The various sub-models must also be connected together radiatively. The two types of numerical model (simple numerical model and full numerical model) differ only in the way the radiative conductors are defined. In the simple numerical model the radiation treatment is similar to the simple analytical model – each component in the cold stage is assumed to view a single node in the warm stage, which is treated as a black body. Therefore the simple numerical model suffers from the same inaccuracies as the SAM, but was used to verify that the conductive couplings were defined correctly and to perform some simple transient analyses. The determination of the radiative couplings for the full numerical model is described in Section 3.5.1.

The boundary conditions are set by defining constant temperature boundary nodes in the sub-models SPACECRAFT and SPACE. SPACECRAFT contains three nodes - one node represents the interface to the CIRS instrument (170K) and the other two the environment which the outside of the cone sees (170K). SPACE contains a single node representing cold space (4K).

Table 3.3: The node breakdown used in the cooler numerical models

Component	Sub-Model Name(s)	Model Type	Num. Nodes
Cooler			
Patch	PATCHBCK	Circular Plate	6
	PATCHSID	Cylindrical Shell	4
	PATCHANN	Annular Plate	4
	PATCHRAD	Circular Plate	7
Cold Finger	COLDFINGER	Cylinder	6
Annular Radiator	CONERAD	Annular Plate	4
Suspension Ring	SUSPRING	Cylindrical Shell	4
Cone	BELL	Cone	6
Cone Top	RADSHIELD	Annular Plate	4
Tube	PLATE1-PLATE4	Rectangular Plate	4x9
Patch Cable	CABLEPT	20 nodes	20
FPA			
Reference Plate	REFPLATE	Rectangular Plate	9
Tripod Legs	FPATRI	1 node	1
Tripod Top	FPA	1 node	1
Common Carrier	FPA	1 node	1
Sub Carriers	FPA	1 node each	2
Flexible Link	FLEXI	2 nodes	2
FP3 Cable	CABLEPC	20 nodes	20
FP4 Cable	CABLEPV	20 nodes	20
Thermostat Cable	CABLETC	20 nodes	20
Other CIRS Instrument	SPACECRAFT	3 nodes	3
Space	SPACE	1 node	1
Total			**175**

3.4.2 Results

The purpose of the SNM was initially only to verify that the node breakdown selected for the model was implemented correctly before up-grading it to the full numerical model (FNM). However owing to problems encountered with maintaining the FNM to the current cooler design, the SNM was used for some simple transient studies earlier in the project.

Table 3.4 shows the comparison between the SNM and the other models. The results of the SNM show good agreement with those from the SAM and ILM. The heat leak through the tripod legs is less than that calculated by the simpler models because the SNM resolves the FPA into a separate common carrier and tripod top. The reduction in the heat leak is caused because the tripod top is slightly warmer than the common carrier. The heat leaks through the electrical cables are different in the SNM to those calculated using the ILM. This is because it was not practical to include the very detailed ILM models into the larger numerical model. The resolution of the cable models was 10 nodes per cable in the SNM compared to 50 nodes in the ILM. Even with this reduction of resolution, the calculated heat leaks are all within 1mW of those calculated using the ILM. The calculated radiative heat loads onto the cold finger and patch back are slightly lower than the SAM values because the hot boundary temperature was assumed to be different. In the SNM the hot boundary temperature was taken to be the temperature of the node at the mid point of the cone when calculating the radiative heat loads.

The effect of the cooler directly viewing the sun when it is at 0.6Au (closest approach) was studied using a variety of models starting with an analytical model of an isolated patch (no support structure etc.) and progressing to a numerical model of the patch and cold finger. A reduced SNM without the FPA was compared to these results as shown in Figure 3-11.

It can be seen that the simple (constant heat capacity) numerical model shows excellent agreement with the analytical calculation for an isolated patch. When the heat capacity is allowed to vary with temperature a somewhat slower warm-up is observed because the heat capacity of aluminium increases with temperature. The addition of a cold finger to the patch results in an additional time lag because of its thermal resistance and heat capacity. The SNM shows a significantly slower warm-up time because the patch is suspended from a cooler support structure and is allowed to radiate back to the instrument. As would be expected the equilibrium temperature of the SNM is slightly lower than the temperatures obtained for the simple models because of radiation and conduction back into the instrument. The figure shows clearly that the FPA temperature will exceed 300K in less than 5 minutes if no action is taken to point the cooler away from the Sun. The temperature limit of the HgCdTe detector arrays is 300K so it

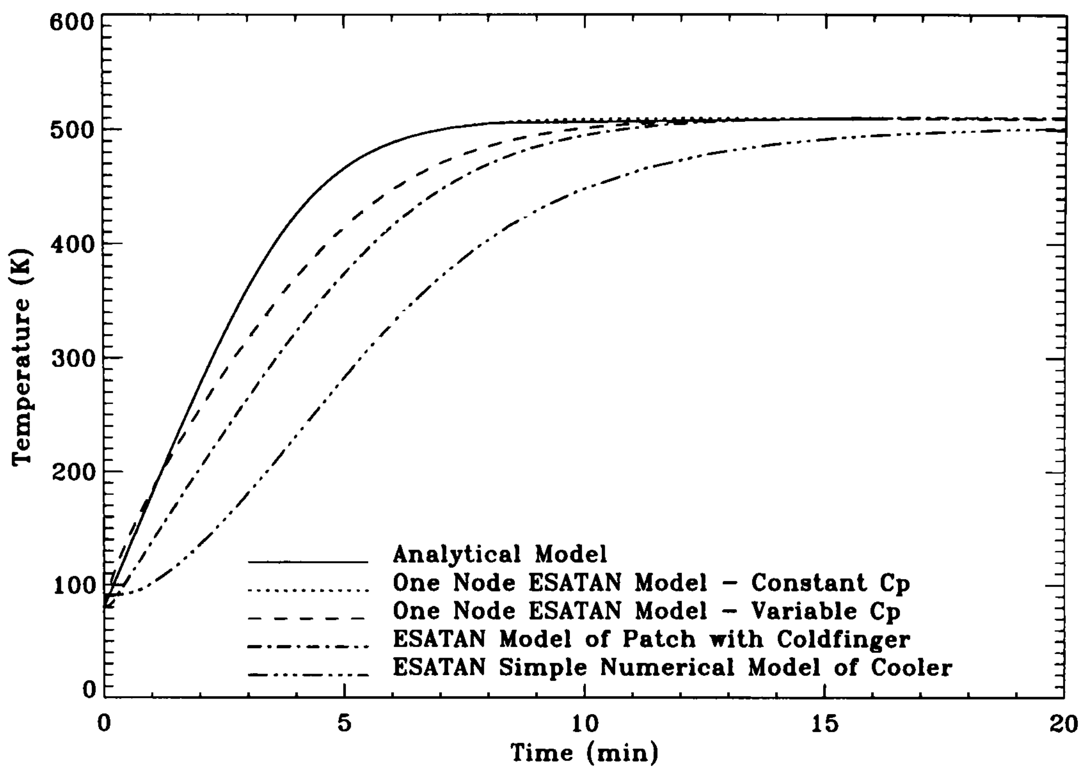

Figure 3-11: Temperature transients predicted by various models representing the cooler viewing the Sun at a distance of 0.6Au

was decided that the cover should remain over the patch during this phase of the cruise to ensure that the detectors would not be damaged by accidentally directing the cooler towards the Sun.

3.5 Full Numerical Model

The full numerical model (FNM) is exactly the same code as the SNM, but with the simple radiation treatment replaced by the results from a geometric model of the cooler developed using NASA's VIEW program and solved using SSPTA [37].

3.5.1 Cooler Geometric Model

The radiative couplings between components in the Full Numerical Model (FNM) were determined using programmes supplied by Goddard Space Flight Center. The programmes used were a geometry definition and visualisation program (VIEW) with a simple program to convert to the input format for the radiation analysis part of the SSPTA[37] program suite.

The model is written using VIEW by specifying the positions and dimensions of primitive shapes (circles, cones etc.). It is then possible to view the model in a number of orientations in order to ensure that the representation is correct and that the surface normals point in the correct direction.

Once the model has been completed using VIEW the geometry must be converted to SSPTA format using a program supplied by NASA. At this stage SSPTA may be used to calculate the viewfactors between the various surfaces in the model. SSPTA calculates the viewfactors between the surfaces by dividing them into a number of sub-surfaces and summing the viewfactors between the sub-surfaces.

The radiative conductances between nodes in the model are calculated by SSPTA by assuming that all reflections are diffuse, i.e. the reflected radiation is distributed uniformly in all directions. In reality this will not be the case — A proportion of the radiation will be reflected specularly. Unfortunately very little data is available in which the specular and diffuse reflectivities of surfaces have been measured for the same sample so it was not possible to calculate the true radiative conductances based on the combined specular and diffuse reflections. It is common practice in thermal analysis to assume perfectly diffuse reflections in order to simplify the analysis, because only one reflectance need be defined for each surface ($1-\epsilon$).

For SSPTA to convert the viewfactors into radiative conductances the surface emissivities must be specified. It is necessary to specify the emissivity and absorptivity for each surface in the model. The radiative conductances are calculated and written to a file which may be converted into ESATAN format using a simple program. The file of conductances is then simply included in the ESATAN input deck for the FNM.

The geometric model of the cooler is shown in Figure 3-12. It can be seen that the cone and patch back are represented by 36 facets each, with other surfaces such as the patch edge and suspension ring represented by 12 surfaces each. This discretisation was chosen to be one which gives an acceptable representation of the geometry while keeping the time for the calculation acceptably small.

It can also be seen that only the cone section of the cooler is modelled - the tube and FPA are not represented at all. This is because the FPA is considerably smaller than the surrounding tube so the simple approximation that it views a black cavity is valid, giving only a small over-estimate of the radiative heat load onto the FPA, so the simple approximation was used in the model to reduce the solution time. This approximation is worst for the flexible link which has a high emissivity. In this case it over-estimates the heat load by just under 5% or approximately 0.4mW. This error is considerably reduced for the remaining components which have low emissivities.

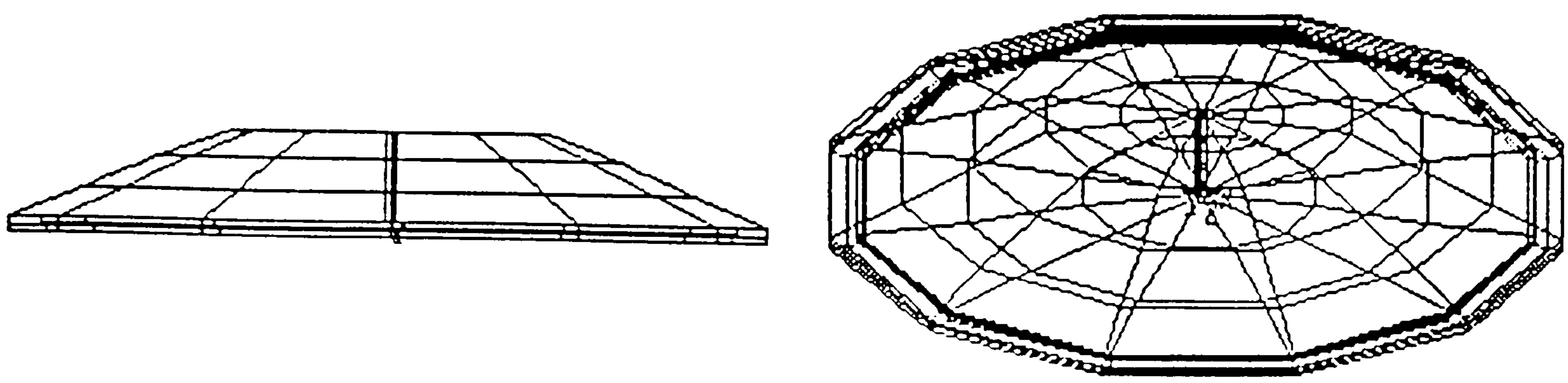

Figure 3-12: The geometric model of the cooler used for radiation exchange calculations.

3.5.2 Results from the Full Numerical Model

Parasitic Heat Leaks

The heat balance calculated using the FNM shows significant reductions in the radiative heat leaks into the cooler components compared to the SAM as shown in Table 3.4. The reduction observed between the SAM and the FNM is due to the removal of the assumptions that the patch views simple cavities and that the temperature gradient along the cone is linear, resulting in a more accurate result for the full numerical model. The radiative heat load onto the cold finger is reduced because the hot boundary temperatures are lower than that assumed in the SAM.

The heat load onto the patch back is 7.0mW smaller than the SNM. The reduction is due partly to the improved treatment of radiation and partly to the reduced cone temperature predicted by the FNM. The heat load onto the patch edge is lower than the SAM value for similar reasons.

Sensitivity of FPA Temperature to Instrument Temperature

The variation of the FPA temperature with instrument temperature was calculated using four of the models described previously in this chapter (SAM with and without detector cable radiation, SNM and FNM). The results are shown in Figure 3-13. The five models

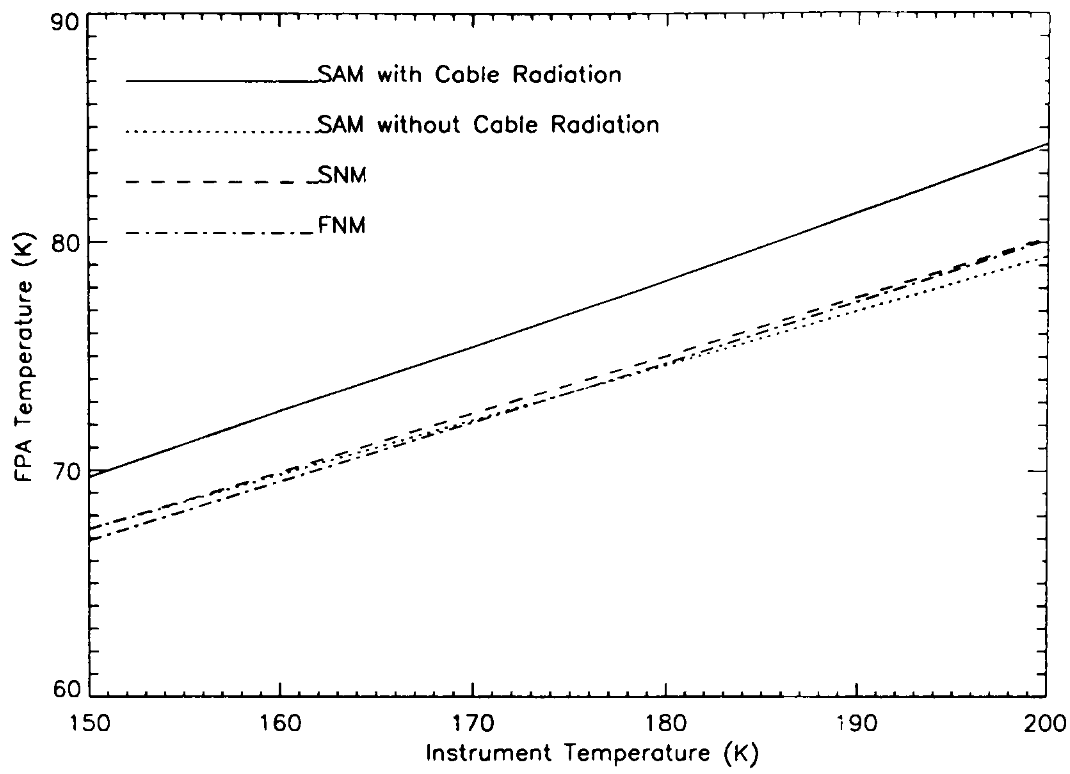

Figure 3-13: The variation of FPA temperature with the temperature of the CIRS instrument calculated using various thermal models.

show good agreement. The FPA temperature calculated using the FNM is generally slightly lower than that calculated using the SNM because of the reduced radiative heat loads calculated using the detailed radiation treatment.

A similar comparison can be made between the models by considering the variation of the FPA temperature with the annular radiator as shown in Figure 3-14. The results are similar to those described above with the FNM showing lower FPA temperatures than the SNM.

Sensitivity of FPA Temperature to Heat Load

The heat load sensitivity (the variation of cold stage temperature with heat load) for the FNM of the cooler was determined by performing a steady state solution on the cooler for various heat loads. The calculation was performed for heat loads into the common carrier and the patch. The results are plotted in Figure 3-15. The gradient of the line gives the heat load sensitivity (the change in FPA temperature per unit change in heat load). The sensitivity to FPA heat load was found to be 0.13K/mW at 80K. The sensitivity to patch heat load (backload) was found to be 1.0K/mW at 80K. The sensitivity to FPA heat load is the larger of the two because the temperature drop along the cold finger increases when the FPA heat load is increased, whereas the cold finger temperature drop

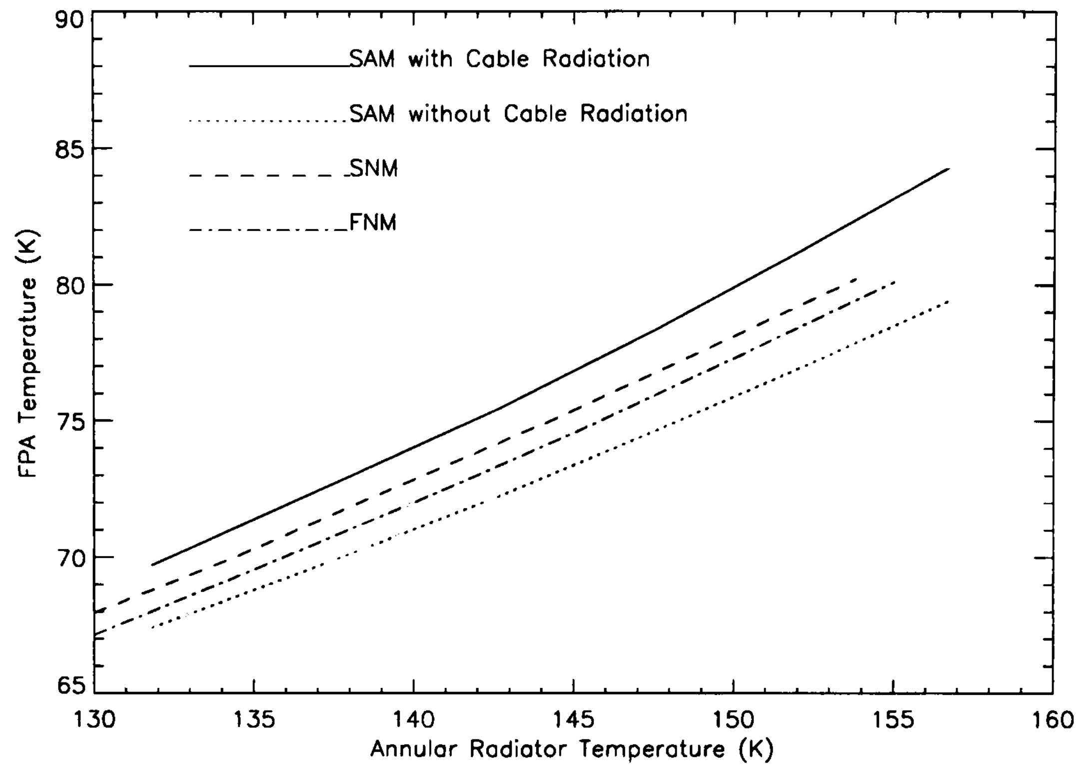

Figure 3-14: The variation of FPA temperature with the temperature of the annular radiator calculated using various thermal models.

is fairly constant if the patch heat load is increased.

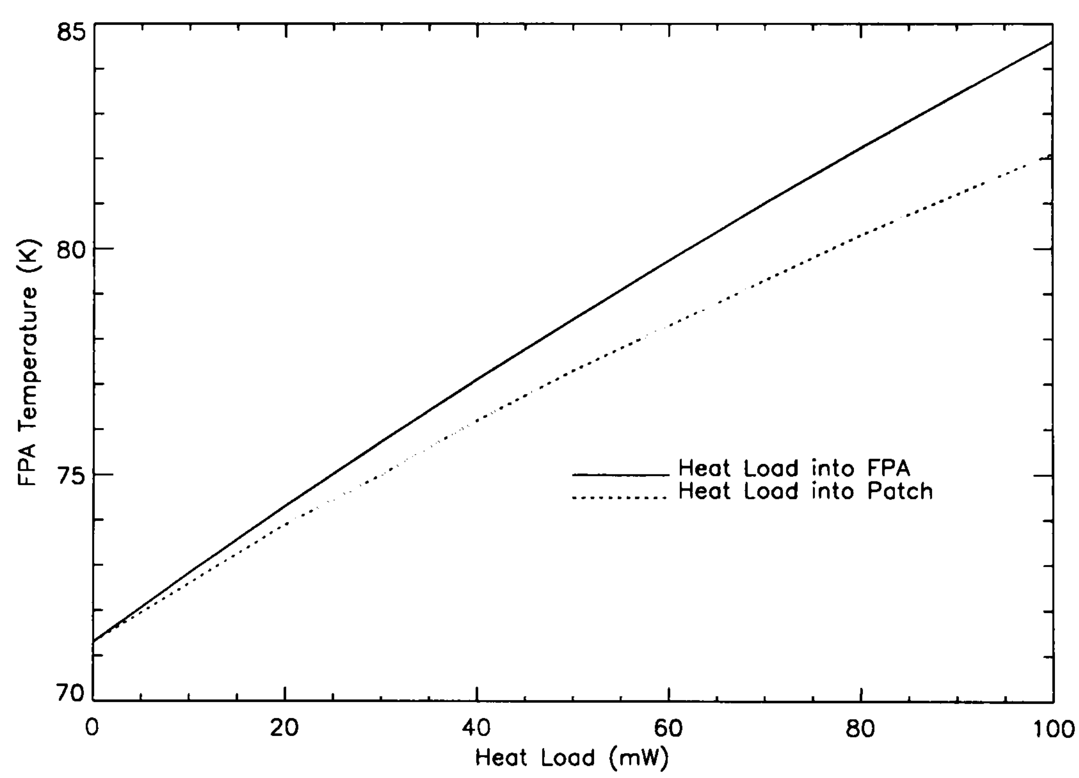

Figure 3-15: The sensitivity of the FPA temperature to to heat load into the common carrier, calculated using the FNM.

Cool Down Time

In order to determine the time the cooler will take to cool from room temperature to its base temperature the full numerical model of the flight model cooler was solved for 300K boundary conditions using a full matrix inversion routine in ESATAN. The temperatures of the instrument and the environment were then reduced to 170K, and the temperature of space to 4K. The transient response of the cooler was determined using a transient solution routine supplied with ESATAN. The results of the analysis are shown in Figure 3-16. It can be seen from the figure that the cooler will take around 15 hours to cool from 300K to 80K when viewing cold space. This will have significance in mission planning when the cooler decontamination sequences will need to be timed so that the cooler has time to reach its operating temperature before it is needed again.

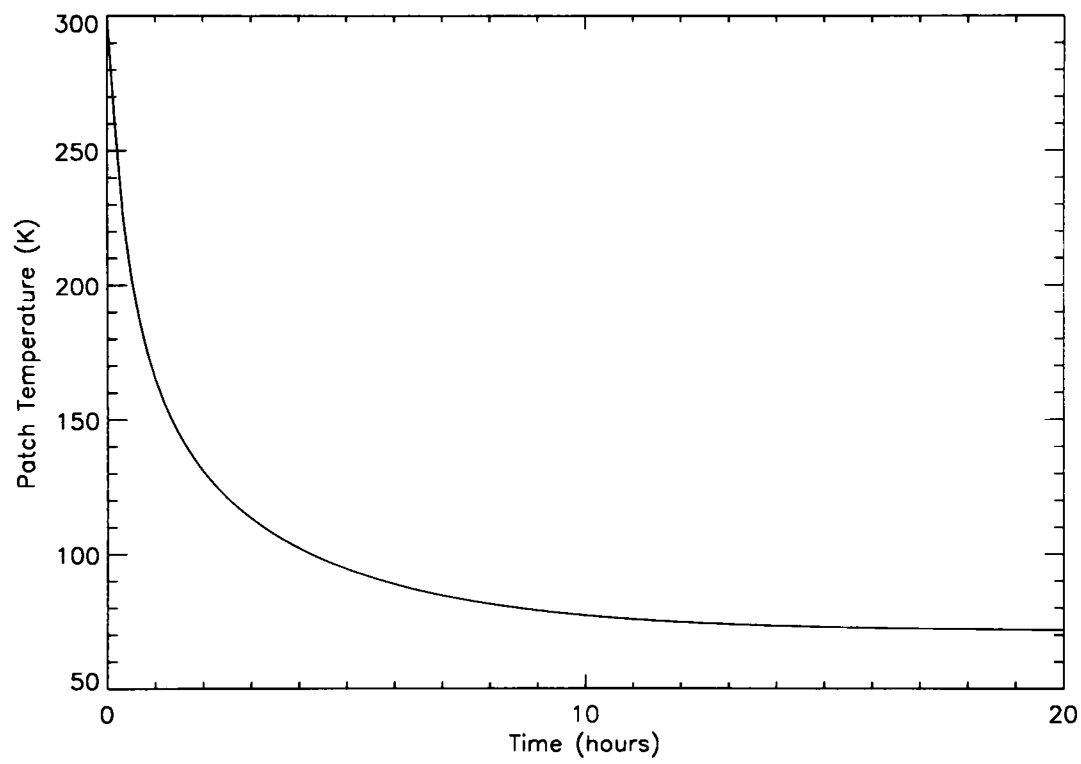

Figure 3-16: The results of the full numerical model simulating a cool down from 300K when viewing cold space

Table 3.4: Comparison between the heat budgets predicted by the four thermal models of the cooler and FPA. The figures in parentheses are the values obtained by calculating the SAM without including the radiation onto the electrical cables.

	SAM	ILM	SNM	FNM
Temperatures (K)				
Instrument	170.0 (170.0)	170.0	170.0	170.0
Environment	170.0 (170.0)	170.0	170.0	170.0
Space	4.0 (4.0)	4.0	4.0	4.0
Annular Radiator	142.8 (142.8)	142.8	137.7	138.5
FPA	80.0 (80.0)	80.0	80.0	80.0
Patch	78.5 (78.9)	78.8	78.6	78.6
Heat Sources (mW)				
Detector Bias Power	5.0 (5.0)	5.0	5.0	5.0
Radiation onto FPA	8.5 (8.5)	8.5	8.3	8.3
FPA Tripod	31.1 (31.1)	31.1	30.1	30.1
FP3 Detector Cable	6.4 (0.8)	3.2	2.7	2.7
FP4 Detector Cable	10.1 (0.4)	2.1	1.3	1.3
Temperature Controller Cable	5.6 (0.4)	2.2	2.5	2.5
Heater Power	0.0 (0.0)	0.0	0.0	0.0
Radiation onto Flexible Link	5.7 (5.7)	5.7	5.7	5.7
Radiation onto Cold Finger	4.4 (4.4)	4.4	3.0	2.9
Radiation onto Patch Back	27.1 (27.0)	27.0	23.4	20.1
Radiation onto Patch Edge	17.6 (17.6)	17.6	15.2	15.6
Patch Suspension	13.5 (13.4)	13.4	12.9	13.1
Patch Electrical Cable	6.5 (4.1)	6.3	5.4	5.4
Total Heat Input	141.4 (118.3)	126.4	115.5	112.8
Radiated Power	185.8 (189.8)	188.6	186.8	186.9
Cooling Capacity at 80K	44.4 (71.5)	62.2	71.3	74.1

Chapter 4

Patch Thermal Blanket Testing

4.1 Multi-Layer Insulations

The side of the patch which faces the cone requires a very low emissivity because of its large surface area and the relatively high temperature of the cone. The emissivity specification for the patch back is 0.01 or less. The heat load onto the patch back represents the largest parasitic heat load into the cold stage of the cooler, which makes the cooler very sensitive to the emissivity of the patch back (a 10% increase in the emissivity will increase the heat load by approximately 2.7mW which is equivalent to an increase in the minimum patch temperature of almost 0.3K).

It is possible that the emissivity target could just be met with a thick layer of gold [27], but this would make the cooler particularly susceptible to contamination which would raise the emissivity of the surface. It was for this reason that a multi-layer insulation (MLI) blanket was chosen to insulate the patch back because MLI is far less sensitive to the emissivity of the outside surface than a bare metal surface.

4.1.1 Theory

A MLI blanket is formed from a number of highly reflective radiation shields separated by insulating spacers. The effective operation of the blanket relies on there being very little conduction between the shields so the heat transfer through the blanket will be radiation dominated.

The one dimensional heat transfer rate between two infinite, parallel, grey planes 1 and 2 is expressed as [41]:

$$\frac{q}{A} = \frac{1}{\frac{1}{\epsilon_1} + \frac{1}{\epsilon_2} - 1} \sigma \left(T_2^4 - T_1^4 \right) \tag{4.1}$$

where q is the heat flow rate between the two surfaces, A is the surface area, T_1 and T_2 are the absolute temperatures of the surfaces, ϵ_1 and ϵ_2 are the emissivities of the surfaces and σ is the Stefan-Boltzmann constant.

If N parallel shields are inserted between two boundaries C and H, and the the above expression for shields i and $i+1$ becomes:

$$\frac{1}{\epsilon_{i,1}} + \frac{1}{\epsilon_{i+1,2}} - 1 = \frac{\sigma A}{q} \left(T_{i+1}^4 - T_i^4 \right) \tag{4.2}$$

The subscripts 1 or 2 represent the emissivities of the two sides of the shields to allow the shields to have different emissivities on each side. Summing the $(N+1)$ equations which govern the heat transfer between the consecutive pairs of plates, and assuming that all of the shields have the same emissivities (ϵ_1 and ϵ_2) gives the following expression for the heat transfer between the hot and cold boundaries:

$$\frac{q}{A} = \frac{1}{\frac{1}{\epsilon_C} + \frac{1}{\epsilon_H} + N(\frac{1}{\epsilon_1} + \frac{1}{\epsilon_2}) - (N+1)} \sigma \left(T_H^4 - T_C^4 \right) \tag{4.3}$$

where ϵ_H and ϵ_C are the emissivities of the hot and cold boundaries respectively. If the outer shields are assumed to be the hot and cold boundaries, the expression simplifies to the well known form:

$$\frac{q}{A} = \frac{1}{(N-1)\left[\frac{1}{\epsilon_1} + \frac{1}{\epsilon_2} - 1\right]} \sigma (T_H^4 - T_C^4) \tag{4.4}$$

Therefore the effective emissivity of the blanket (ϵ_{eff}) is given by:

$$\epsilon_{eff} = \frac{1}{(N-1)\left[\frac{1}{\epsilon_1} + \frac{1}{\epsilon_2} - 1\right]} \tag{4.5}$$

For example, assuming a blanket is formed from 10 shields with emissivity 0.03 on both sides, the effective emissivity calculated using equation 4.5 is 0.0017. This would suggest that the $\epsilon = 0.01$ specification should be achieved easily, but this simple theory assumes the shields are infinite plates so the effects of the edge of the shields and any penetrations for supports etc. are neglected. Some limited data has been published on the effects of penetrations on the emissivities of blankets [31], but the prediction of the performance of MLI blankets is known to be exceedingly difficult [32, 33, 34, 35, 41] so a calorimeter was developed to measure the heat leaks through prototype MLI blankets to determine the number of shields necessary for the patch blanket. The apparatus and test results are descried in Sections 4.3 and 4.5.

4.2 MLI Materials

A number of materials have been used in multi-layer insulations on spacecraft. The most common shield material is aluminised mylar, although this is tending to be replaced by aluminised kapton which is less flammable. Metal foils such as aluminium and titanium have also been used, but usually in high temperature applications such as near engines.

If the MLI is to work in the manner described above, it is important to ensure that there is the absolute minimum of thermal conduction between the shields. This is achieved either by using a spacer, which is usually a net formed from a polymer material, or for the case of aluminised mylar shields by crinkling the shields to ensure that there is only a small contact area between them. The purpose of the tests described below was to determine the best method to use, and to determine the number of shields required.

There is a large variety of possible spacer materials such as Dacron, silk or nylon net or glass fibre paper. Many other spacer materials have been used in the past, but many of them pose unacceptable contamination or outgassing hazards.

It is well known that MLI blankets tend to retain contaminants so they are usually perforated to allow outgassing. The patch blanket is sufficiently small to enable it to vent at the edge only. The blanket is assembled in house so that its cleanliness can be controlled and monitored.

4.3 Thermal Blanket Test Apparatus

The apparatus which was used to measure the heat leaks through the thermal blankets was a flat plate calorimeter. This technique has the advantage over the more conventional

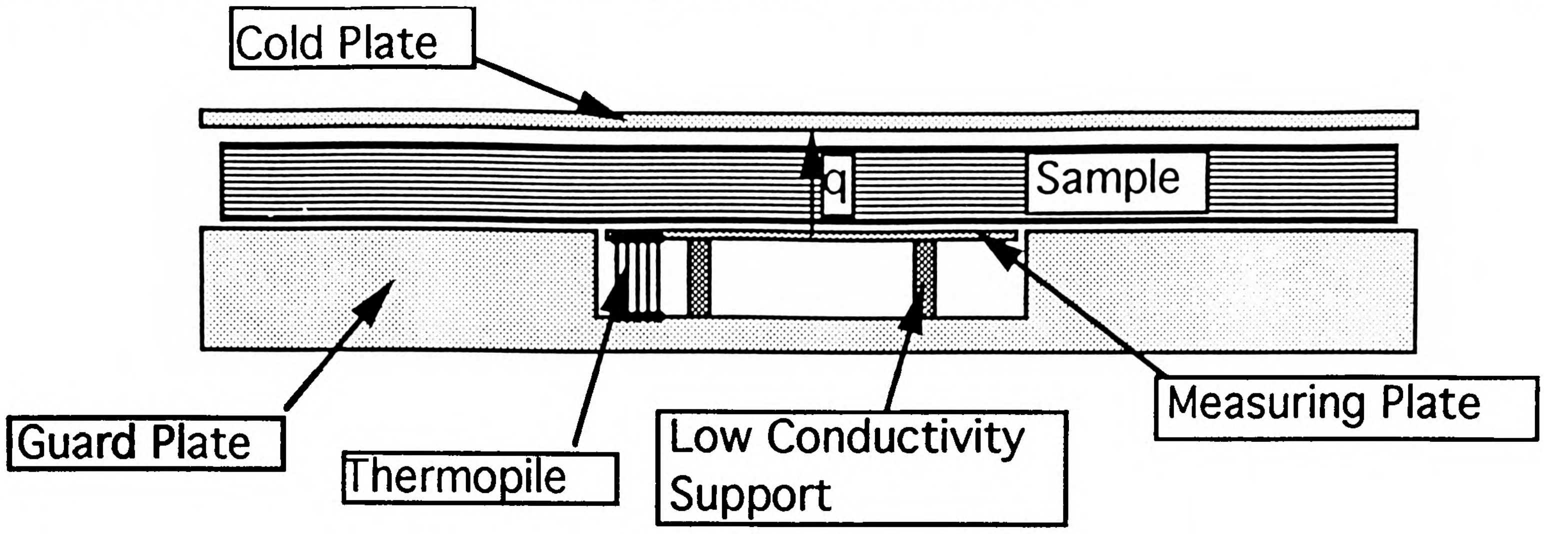

Figure 4-1: Schematic of a Flat Plate Calorimeter

boil-off type calorimeters in that the MLI sample was installed flat in the same way that it will in the cooler, whereas a boil-off calorimeter requires the sample to be wrapped around a cylindrical dewar.

A schematic of a flat plate calorimeter is shown in Figure 4-1. It contains three plates — the cold plate which is blackened, the measuring plate, and the guard plate which contains a well in which the measuring plate is supported on a low conductance support as shown. The sample is placed between the measuring plate and the cold plate. The apparatus is suspended within an evacuated cryostat to provide thermal insulation and cooling.

The cold plate and guard plate are set to the cold and hot boundary temperatures respectively. In thermal equilibrium the measuring plate will tend to float to a lower temperature than the guard plate because there is very little thermal contact between them and the top surface of the measuring plate is radiating to the cold plate through the sample. The temperature difference between the guard plate and the measuring plate is monitored using a 10 way thermopile. A small heater on the measuring plate is used to null out the temperature difference between the two plates. When the temperature difference between the guard plate and the measuring plate is zero there is no heat transfer between the guard and measuring plates so the power being supplied by the heater must be being radiated through the sample to the cold plate. This gives the heat flow through the sample from the area of the measuring plate between two boundary temperatures.

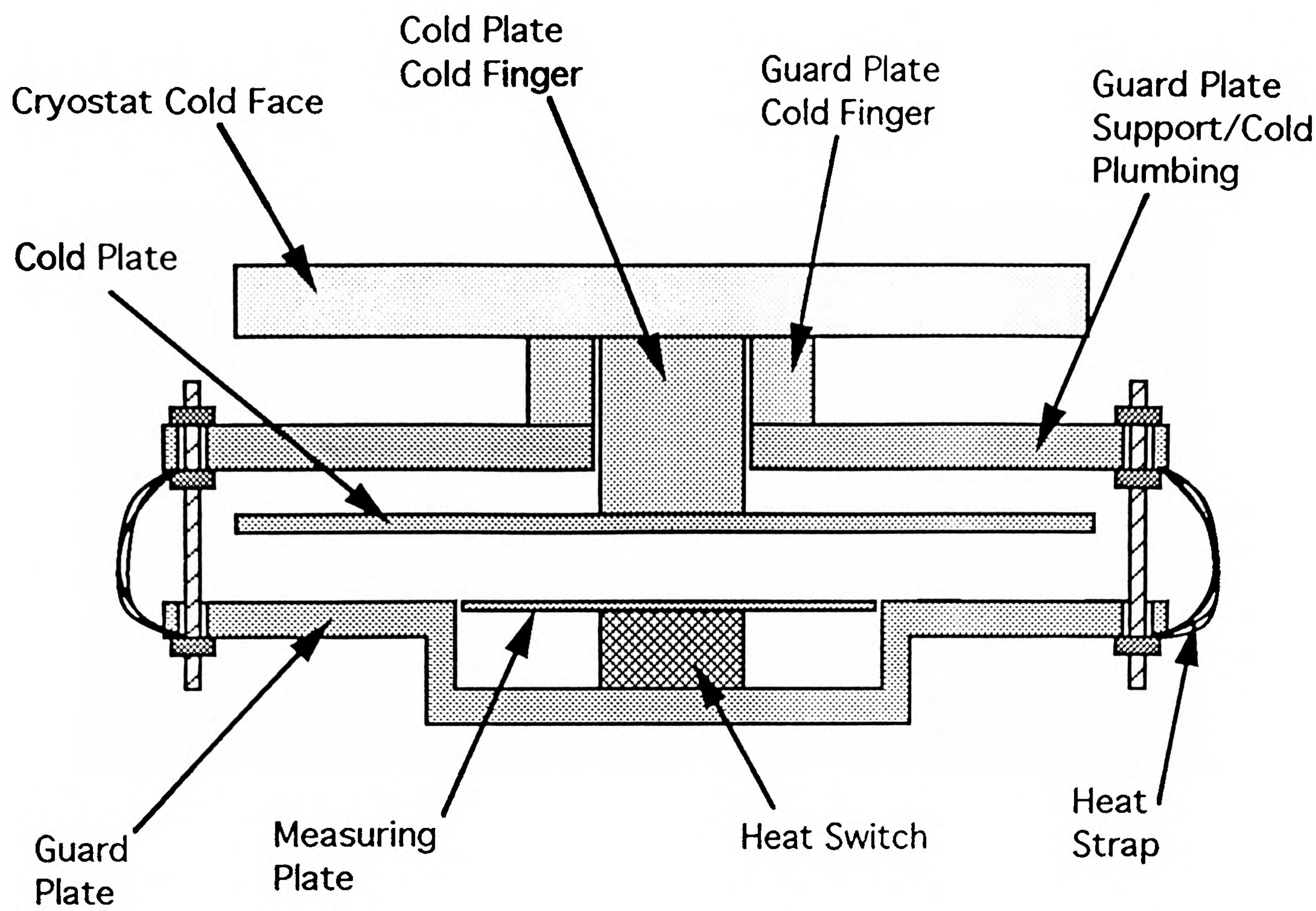

Figure 4-2: Schematic of the Flat Plate Calorimeter Cold Plumbing

4.3.1 Thermal Design

In order to accommodate the calorimeter within a simple reservoir cryostat the thermal design of the calorimeter has been kept very simple with both the cold plate and the guard plate being cooled conductively via copper cold plumbing from the liquid nitrogen reservoir base. The configuration is shown in Figure 4-2.

The guard plate cold plumbing serves as the mechanical support for the guard plate which is suspended from threaded stainless steel rods. The guard plate is cooled conductively from the cold plumbing using flexible copper braid heat straps.

The measuring plate originally sat in the well in the guard plate, supported by a thin walled kapton tube in order to ensure that it is well thermally isolated from the guard plate. Initial tests revealed that there was insufficient thermal contact between the measuring plate and the guard plate for the measuring plate to cool down within an acceptable time — the guard plate would cool to around 150K overnight but the measuring plate would remain about 70K higher. It was therefore decided that a heat switch was necessary which could be turned on to make a good thermal contact between the guard plate and measuring plate in order to cool the measuring plate. Once down to temperature the heat switch could be closed to leave the measuring plate thermally isolated to take the readings.

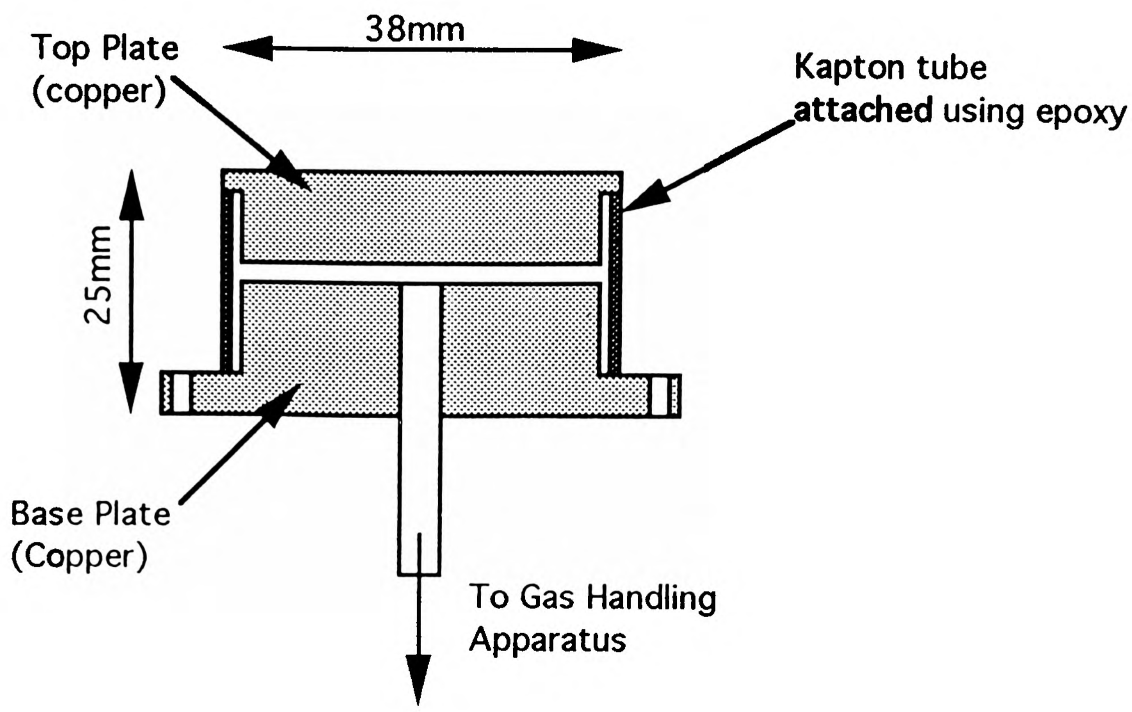

Figure 4-3: Schematic of the Measuring Plate Heat Switch

The heat switch comprises two copper plates separated by a kapton tube as shown in Figure 4-3. The switch is turned on by filling the gap between the plates with gas and turned off by venting the gas into the vacuum chamber. This technique gives two orders of magnitude variation in the thermal conductivity of the heat switch between the 'on' and 'off' positions.

4.3.2 Cryostat

The cryostat which houses the calorimeter is a simple liquid nitrogen (LN2) reservoir cryostat (see Figure 4-4). It comprises a single vacuum chamber which houses both the reservoir and the calorimeter. The cryostat is supported from the top, which enables the base of the vacuum chamber to be removed to gain access to the apparatus mounted beneath the reservoir. The apparatus is bolted directly to the copper base plate of the LN2 reservoir.

The chamber is evacuated using a turbo-molecular pumping system as shown in Figure 4-5. The system is connected in such a way that it is possible to isolate the vacuum chamber and switch to pumping the liquid nitrogen dewar should lower temperatures be required.

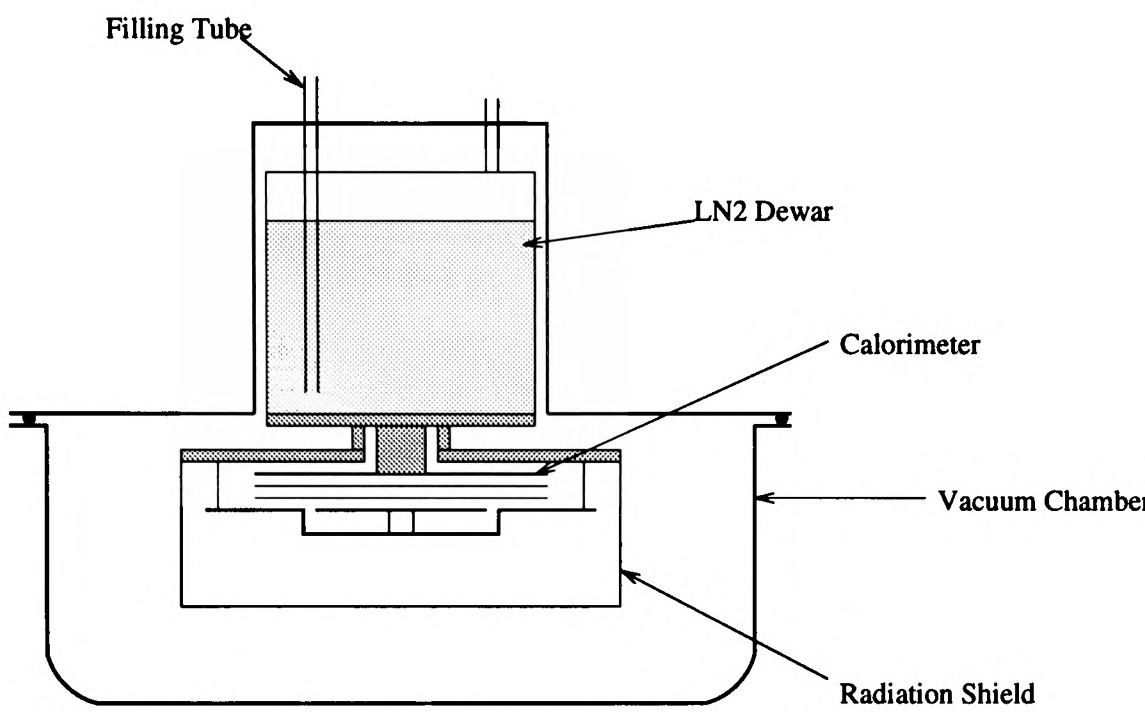

Figure 4-4: Schematic of the cryostat used for MLI measurements

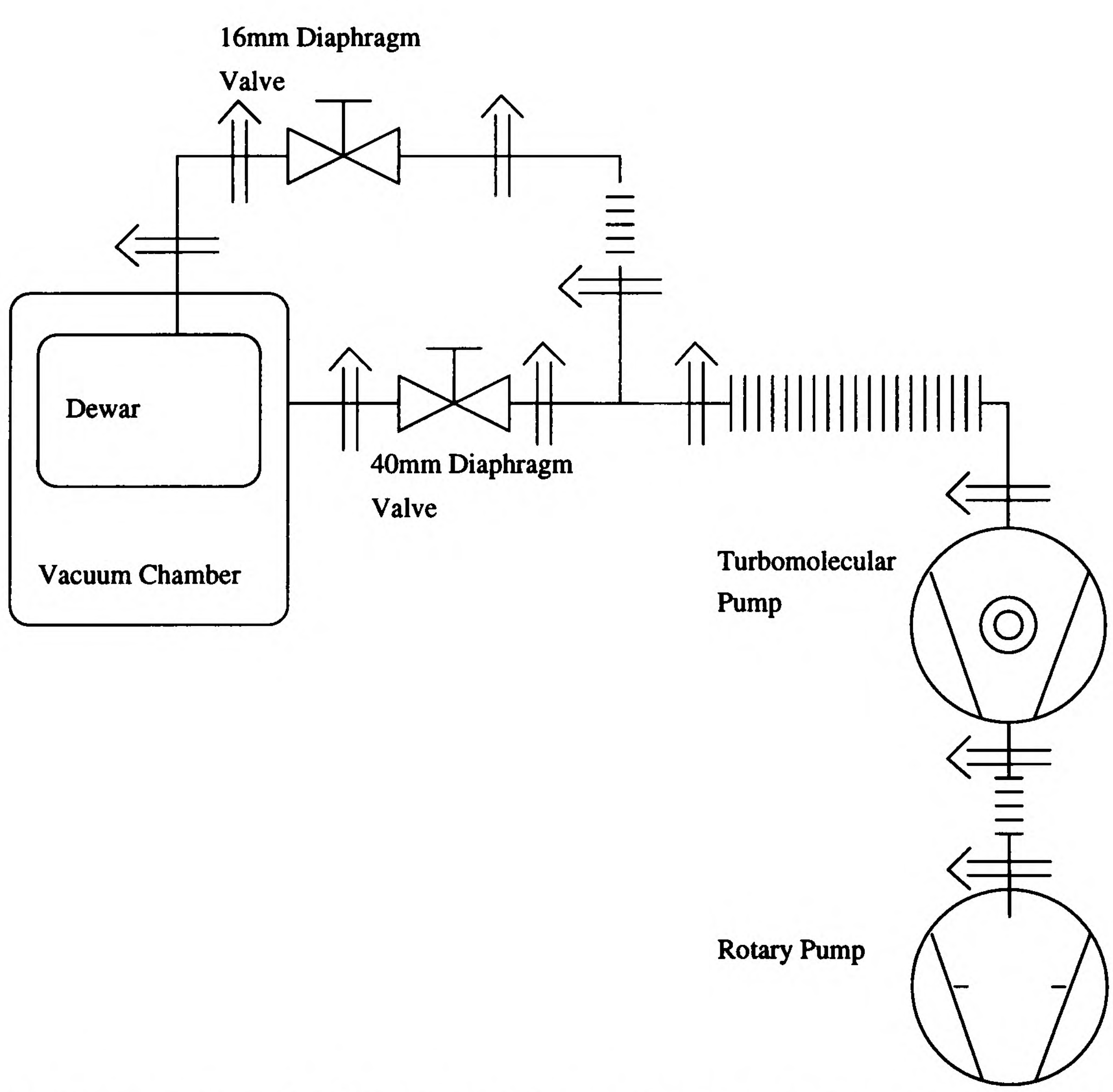

Figure 4-5: Vacuum system for the MLI test cryostat. Symbols conform to DIN 28 401 [42]

4.3.3 Temperature Control and Measurement

The flat plate calorimeter requires three temperatures to be controlled — the cold plate, the guard plate and the measuring plate. The cold plate and guard plate are controlled using identical systems utilising commercial PID temperature controllers to switch a low voltage a.c. supply to the heaters. The measuring plate uses a custom built temperature controller.

The temperature difference between the guard plate and measuring plate must be controlled to be less than 0.1K to reduce the error in the measurement of the heat flow through the sample. The value of 0.1K was used as the error in the temperature difference between the guard plate and the measuring plate in the error analysis of the system, and it was found that with this temperature error accuracies of better than ±8% could be achieved in the emissivity determination. Because it is only the temperature difference which is of importance rather than the absolute temperature a differential thermopile is used to monitor the temperature difference. The thermopile is a 10 way copper/eureka (copper/constantan) thermopile giving a sensitivity of approximately 200μV/K.

The output from the thermopile is used directly as the error signal in a proportional temperature controller. The circuit diagram for the controller is shown in Figure 4-6.

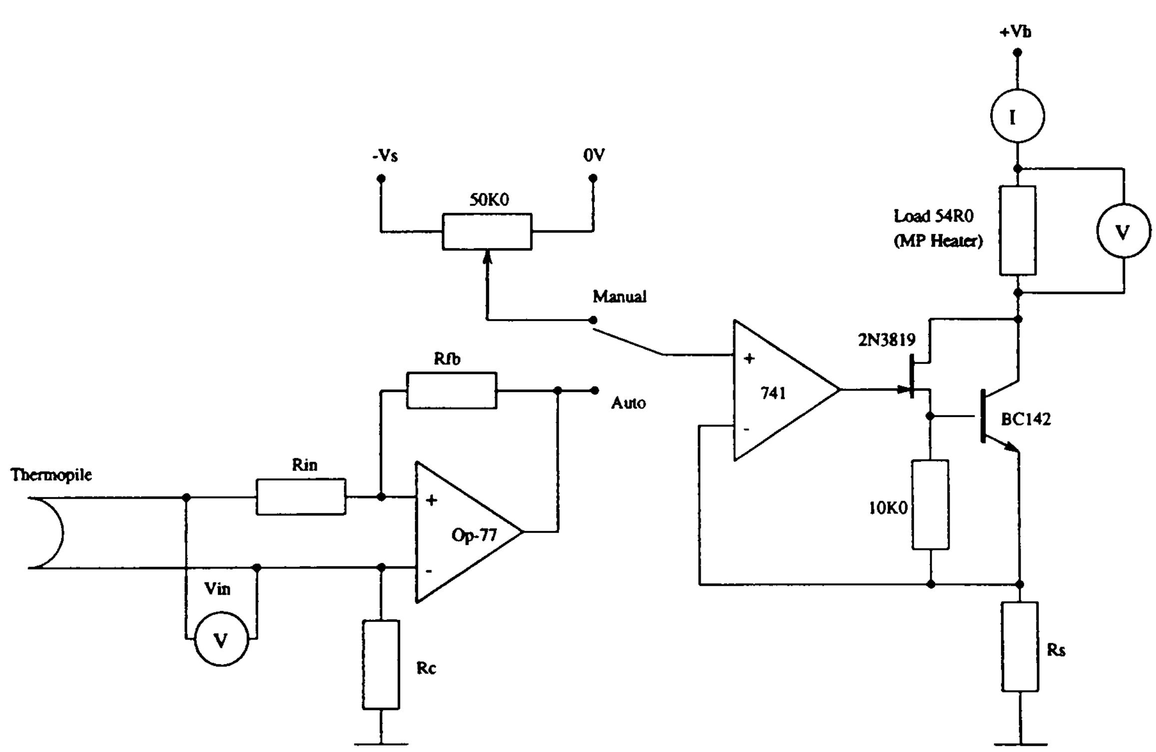

Figure 4-6: Measuring Plate Temperature Controller

The proportional controller is the inverting amplifier with R_{fb} as feedback. The offset of the OP-77 is small enough that no offset null circuitry is necessary. The control signal is fed into the current sink formed by the 741 op-amp and the transistors to supply the heater current. The "Auto/Manual" switch is provided to enable the heater current to be set manually if required. The heater power provided to the measuring plate is measured using analogue 'Avo' meters to measure the heater current and voltage in a four wire system.

4.4 Data Analysis

The effective emissivity of the blanket can be determined simply by measuring the heat flow through the blanket between two boundary temperatures. The heat flow is given by:

$$q = \frac{1}{\frac{1}{\epsilon_{eff}} + \frac{1}{\epsilon_c} - 1} A\sigma(T_h^4 - T_c^4)$$

where ϵ_{eff} is the effective emissivity of the blanket, ϵ_c is the emissivity of the cold boundary plate (assuming that the blanket is attached to the hot boundary), A is the area of blanket through which the heat flow is being measured and T_h and T_c are the hot and cold boundary temperatures respectively.

If the cold boundary plate is blackened, then $\epsilon_{eff} << \epsilon_c$, and rearranging to give ϵ_{eff} gives:

$$\epsilon_{eff} = \frac{q}{A\sigma(T_h^4 - T_c^4)}$$

The error analysis of the above expression reveals that the error in the emissivity measurement will be dominated by the error in the power q. An error of $\pm 7.6\%$ will be achieved for an error in the power of $\pm 7.2\%$. The value of $\pm 7.2\%$ has been the accuracy obtained using the test apparatus to measure emissivities of around 0.01 for measuring plate and a guard plate temperatures of around 170K. Better accuracies are obtained for higher emissivities or higher guard plate temperatures where the heat flow is greater.

4.5 Results

4.5.1 Measurements Taken

The results of the experiments are summarised in Table 4.1. Unless otherwise stated the sample was considerably larger than the measuring plate to reduce the edge effect. The chamber pressure was less than 2×10^{-6}torr during all the tests.

The first sample to be tested consisted of five layers of aluminium foil separated by nylon net. The vacuum chamber was pumped for 15 hours then the calorimeter was cooled down. The emissivity was measured as 0.0044 between boundary temperatures of 282K and 83K. The measured emissivity fell over the next 7 hours to 0.0029. This fall was attributed to out-gassing of the spacer material. In order to ensure that the sample was thoroughly de-gassed the system was warmed to ambient temperature and the sample baked at 19°C under vacuum for 50 hours. The system was then cooled and the emissivity found to be unchanged at 0.0029 between the same boundary temperatures as above.

The emissivity of the sample was also measured at lower guard plate temperatures. No significant change in the measured emissivity was found when the guard plate temperature was reduced to 170K. Because reducing the guard plate temperature reduces the total heat flow through the blanket, the accuracy of the measurement decreases so most of the measurements were performed with the guard plate at ambient temperature, and the emissivity of the sample determined using the measured boundary temperatures. Using a warm hot boundary also had the effect of considerably decreasing the system cool down time.

NRC-2 "superinsulation" (aluminised mylar) was measured for comparison. 5 and 10 layer blankets were measured without a spacer — the thermal isolation between shields was provided by the low contact area because of the crinkled texture of the shields. Since the emissivities of these blankets were considerably larger than that of the aluminium foil blanket a third measurement was taken of 5 layers of NRC-2 separated by nylon net in order to give a better comparison to the aluminium samples measured.

The effect of a standard fibreglass MLI retaining post on the emissivity of the aluminium blanket was assessed by gluing the post to the centre of the measuring plate and punching a hole through the aluminium foil blanket. The emissivity of the blanket with

Table 4.1: Summary of the test results for MLI Samples measured between room temperature and approximately 80K.

Number of Layers	Shield	Spacer	Notes	Emissivity
5	Aluminium Foil	Nylon Net		0.0029
5	Aluminium Foil	Nylon Net	1 Retaining Post	0.0119
5	Aluminium Foil	Nylon net	small blanket	0.0181
5	NRC-2	None		0.0093
10	NRC-2	None		0.0079
5	NRC-2	Nylon Net		0.0082

the fibreglass support was measured in the same way as for the plain blanket.

The magnitude of the edge effect (the increase in the heat leak through the blanket because of emission from the edges of the blanket) was assessed by cutting an aluminium foil blanket to the same size as the measuring plate. The emissivity measured was therefore the emissivity of an infinite blanket plus a contribution from the edges. The contribution from the edges may be deduced by comparison to the results for a large, effectively infinite blanket.

4.5.2 Discussion

The result for the aluminium foil and nylon net blanket was extremely encouraging, showing that a plain, infinite blanket should meet the 0.01 emissivity specification without difficulty. In fact the emissivity is very close to the theoretical minimum of 0.0028 which is obtained by assuming a shield emissivity of 0.03 in Equation 4.3. This should not be too surprising since the blanket was not compressed so there was very little force between the shields and the spacers resulting in a very high contact resistance. The emissivities of the aluminium foil blankets with edge effect and a retaining posts were significantly higher than the 0.01 emissivity target. This is to be expected because the tests were performed on considerably smaller blankets than the patch back (the measuring plate was 10cm in diameter). The next section estimates the emissivity of the patch blanket by scaling the effects due to the edge effect and the post.

The NRC-2 results were unexpectedly poor. The emissivities measured were only just less than the 0.01 emissivity specification, and adding holes for retaining posts would certainly make the emissivity unacceptable. Since the results for 5 layers of NRC-2 with and without nylon spacers are both large by comparison to the aluminium foil and nylon spacer, it is likely that the reason for NRC-2 being poor is because the shield emissivity is higher than that for aluminium foil. This is probably because the VDA coating on the mylar is only applied to one side, so the other side of the film has a higher emissivity. In addition the crinkling of the shield increases its apparent emissivity because of geometrical factors. If we assume the aluminised side to have an emissivity of 0.05, and the mylar side to have an emissivity of 0.5, the effective emissivity according to Equation 4.3 is 0.0072. If the mylar side is assumed to be black in the infra-red the predicted emissivity rises to 0.0081.

Because the aluminium foil insulation showed considerably better thermal performance than aluminised mylar, and would produce considerably less contamination than either mylar or kapton shields, it was decided to use a 5 layer blanket of aluminium foil with a spacer for the cooler. The spacer chosen was Dacron because it has better outgassing characteristics than nylon and is space qualified[20]. Unfortunately at the time of the tests the Dacron net was not available for testing, but because Dacron net is a coarser mesh than the nylon net tested it should be expected to give improved performance over the nylon net.

4.5.3 Predicted Emissivity of the Patch Blanket

The calorimeter used in the above experiments was considerably smaller than the cooler patch so it was not possible to test the actual patch blanket so the emissivity is estimated using the data available from the tests described above. The patch diameter is 35.4cm whereas the measuring plate diameter was only 10cm.

The emissivity of the patch blanket is formed from components from the heat leak through the blanket itself, through the retaining posts and from the edge effect, which is due to radiation from the edge of the blanket.

The total heat leak through the plain aluminium foil and nylon net blanket was $\epsilon A\sigma(T_h^4 - T_c^4)$ where $T_h = 170$K and $T_c = 80$K. This gives a total heat leak of 1.061mW. In order to determine this contribution for the real patch, we simply scale by the ratio of the areas of the patch to the measuring plate to give 12.997mW.

The total heat leak through the blanket with the edge effect was 6.402mW. The contribution from the edge effect is found by subtracting the heat leak through the plain blanket – 6.402-1.061 = 5.341mW due to the edge effect. We assume that the edge effect is proportional to the circumference of the blanket so we scale as the ratio of the diameters of the patch to the measuring plate to give an edge effect contribution of 18.694mW.

The total heat leak through the blanket with one retaining post was 3.183mW. Subtracting the heat leak through a plane blanket gives a heat leak of 2.122mW due to one retaining post. In the cooler we use 6 retaining posts so the total heat leak will be $2.122 * 6 = 12.732$mW.

Since the heat leaks due to each component have been determined the emissivity of the patch may be determined using:

$$\epsilon = \frac{q_{blanket} + q_{edge} + q_{posts}}{A_{patch}\sigma(T_h^4 - T_c^4)}$$

$$\epsilon = \frac{(12.997 + 18.694 + 12.732)\times10^{-3}}{0.1 \times 5.67\times10^{-8}(170^4 - 80^4)} = 0.0099$$

From this calculation we would expect the cooler blanket to just meet its 0.01 emissivity specification. It must be remembered that this is very much an estimate to give an indication of the relative magnitudes of the components of the blanket emissivity and ensure that the blanket will be close to its specification. The above calculation shows that all three components of the blanket emissivity are of similar importance, so if during the cooler tests it is suspected that the blanket is not performing correctly a number of options are open to improve its performance:

- Increase the number of layers: This will reduce the blanket conduction part of the emissivity, but it is likely to increase the edge effect because the blanket will be thicker, so it is not certain that the net effect would be beneficial.

- Cover the retaining posts: Covering the retaining posts with aluminium tape will reduce their emissivity and cover any gaps in the blanket so should reduce the component due to the posts.

- Reduce the edge effect: The edge effect may be reduced by shielding the edge of the blanket to reduce the radiative load onto it and securing the edge so the blanket is as thin as possible while not allowing the shields to touch. A great deal of care will need to be taken to ensure that no conductive paths are created between the top shields and the back of the patch itself because this could negate the shielding effects of the blanket.

Chapter 5

The Cooler Test Facility

5.1 Overview of the Test Facility

In order to verify the cooler thermal models described previously against experimental results it was necessary to test the cooler in a similar thermal environment to that which will be encountered during the mission. The cooler test facility is shown schematically in Figure 5-1. The vacuum system for the cooler test facility was designed and procured by Dr. R. Watkins and assembled and commissioned by the author. The remaining internal components were designed and assembled by the author.

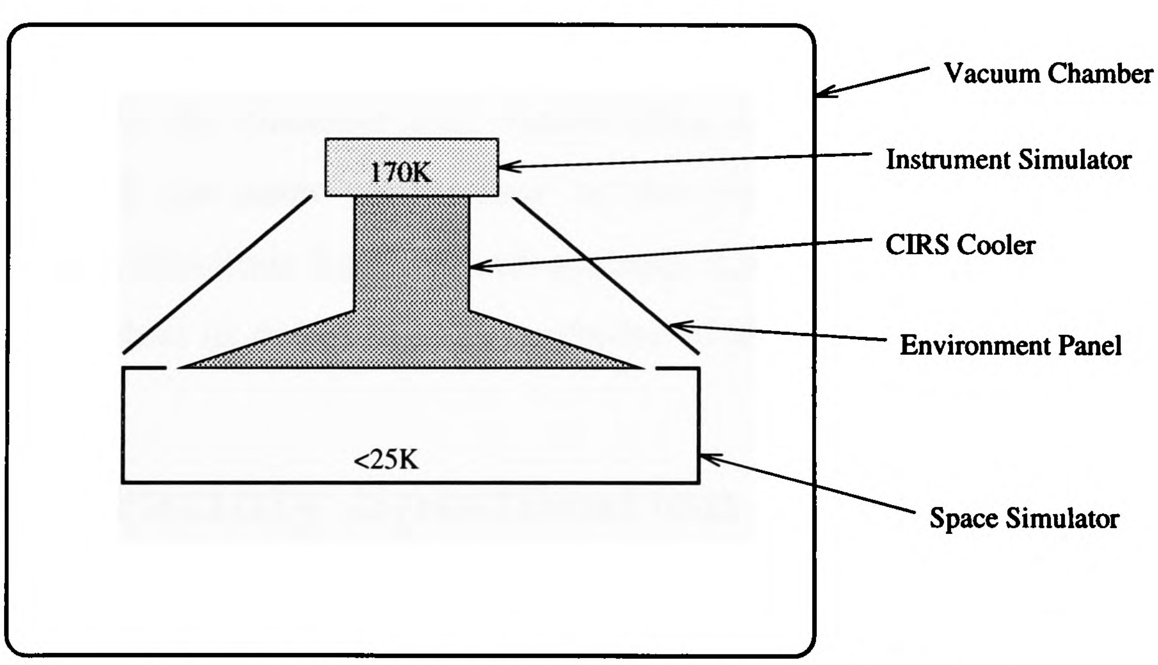

Figure 5-1: The Cooler Test Facility Configuration

The main requirements for the test facility are that it should provide the following:

1. A clean area for cooler and FPA assembly.

2. A high vacuum environment for the cooler and test facility components.
3. A simulation of the thermal and mechanical attachment of the cooler to the CIRS instrument.
4. A simulated view to space for the patch and annular radiator.
5. A known and controllable background temperature for the outside of the cooler.
6. Measurement and logging of the temperatures of the cooler test facility components and the cooler thermometers.
7. Control of the temperatures of the cooler test facility components to provide steady boundary temperatures for the cooler.

The cooler test facility is housed in a clean room which contains clean assembly areas and provides services such as electricity and cooling water supplies for the vacuum systems. The system is based around a stainless steel vacuum chamber which contains the simulated interface to the CIRS instrument, the space simulator black body and two cooled environment panels to surround the cooler as shown in Figure 5-2. The instrument simulator and the environment panels are mounted from a stainless steel tripod, the base of which is supported at the bottom of the chamber (not shown) and are cooled using a commercial circulating coolant refrigeration system. The space simulator is supported within the chamber and cooled using a commercially produced cold head which is driven off the same compressor as the cryopump which pumps the vacuum chamber. The specifications for these sub-systems are considered in Section 5.2 with the components described in detail in the remainder of this chapter.

5.2 Test Facility Specification

5.2.1 Vacuum System Specification

The purpose of the vacuum system is to provide a vacuum environment for the cooler tests which is similar to that to be encountered during the mission. The main effect of the cooler being operated in vacuum conditions is to remove any convection and gas conduction from the system. Convection is not significant at the pressures attainable in

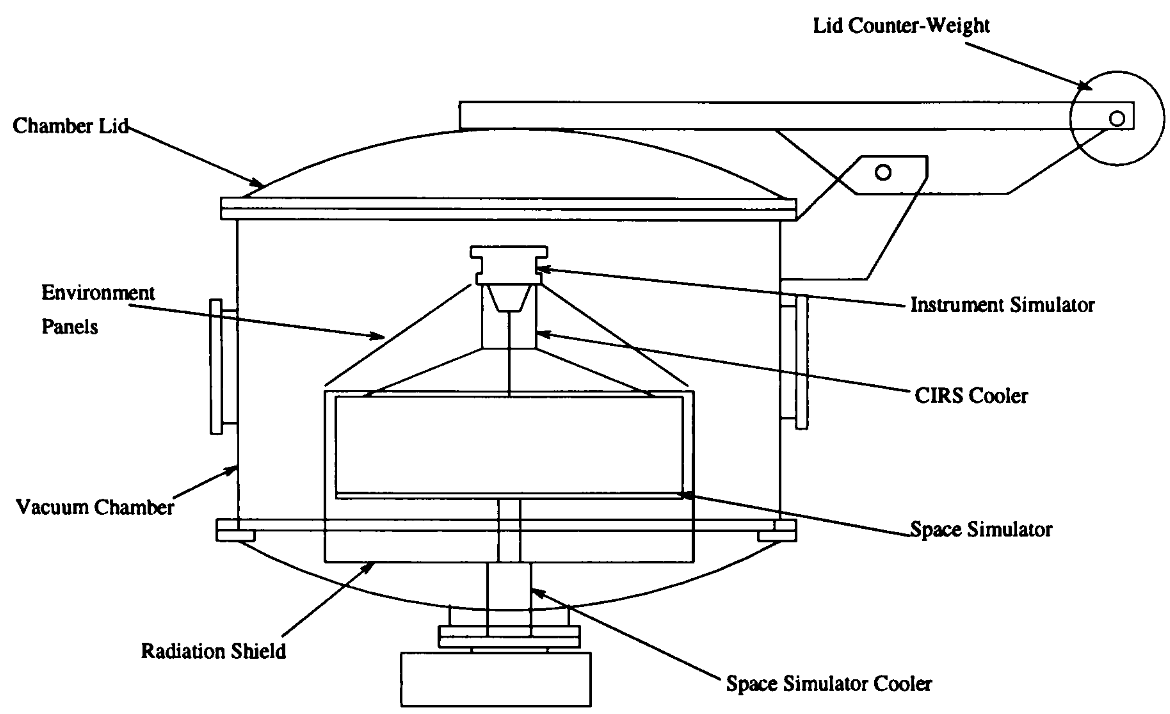

Figure 5-2: Cooler Test Facility Configuration

a high vacuum system so the only heat transport mechanism which must be considered is residual gas conduction. The heat flow between the cone and the patch back due to residual gas conduction is the most significant because the patch is shielded from warmer surfaces by the cone and the space view black body.

The heat flux due to residual gas conduction at low pressure between two surfaces is given by [39]:

$$q_c/A_1 = K a_0 P (T_2 - T_1) \tag{5.1}$$

where K is a constant, a_0 is the overall accommodation coefficient, P is the pressure in torr and T_1 and T_2 are the temperatures of the surfaces. K is approximately 0.016 for air[39] and a_0 is given by:

$$a_0 = \frac{a_1 a_2}{a_2 + \frac{A_1}{A_2}(1 - a_2) a_1} \tag{5.2}$$

where a_1 and a_2 are the accommodation coefficients of the two surfaces and A_1 and A_2 are the areas of the surfaces. If we assume that the cone can be represented by a flat plate, then A_1 and A_2 are both approximately 0.1m^2. a_1 and a_2 are both approximately equal to 0.9 [24] giving a value of 0.818 for a_0.

In the cooler the boundary temperatures are approximately 170K and 80K so using equation 5.1 the power absorbed by the patch due to residual gas conduction is found to be approximately 11.78P watts (where P is the pressure in torr). The target pressure of the vacuum system was set at 5.0$\times$10^{-6}torr when the cooler was installed in the chamber and cold. This target pressure was attained easily for each cooler test. In the vacuum system pressures of 1.0×10^{-6} torr were attainable giving an additional parasitic heat load into the patch of 0.01mW, which can safely be neglected.

5.2.2 Space View Black Body Specification

Cold space has an infinite area and heat capacity, an emissivity of unity and a very low temperature (<4K)[39][40]. It would not be practical to attempt to reproduce this environment in the laboratory where the space simulator target must have finite area and emissivity. This limitation induces an error to the simulation, expressed as a fractional error in the net power radiated to the space simulator target compared to the power that would be radiated to real space. If we assume the patch to be a perfect emitter the net power radiated to space is given by:

$$q_s = A\sigma(T_p^4 - T_s^4) \tag{5.3}$$

and the net power radiated to the space simulator is given by:

$$q_h = \epsilon_h A\sigma(T_p^4 - T_h^4) \tag{5.4}$$

where A is the patch area, T_p is the patch temperature, T_s is the radiative temperature of cold space, ϵ_h is the emissivity of the space simulator target and T_h its temperature.

The fractional error in the radiated power δ is $(q_s - q_h)/q_s$. Substituting the above expressions for the radiated powers gives:

$$\delta = 1 - \epsilon_h \frac{T_r^4 - T_h^4}{T_r^4 - T_s^4} \tag{5.5}$$

This expression relates the fractional error in the radiated power to the space simulator target's temperature and emissivity. The variation of the simulation error δ with target emissivity is plotted in Figure 5-3. It can be seen from the figure that in order to reduce the error to less than 2% the target should have an emissivity of at least 0.99 and a temperature of less than 25K. Figure 5-4 shows the variation of the error with target temperature. It can be seen that for higher temperature radiators (such as the annular radiator or the cooler patch during decontamination), much higher target temperatures may be tolerated without increasing the error significantly.

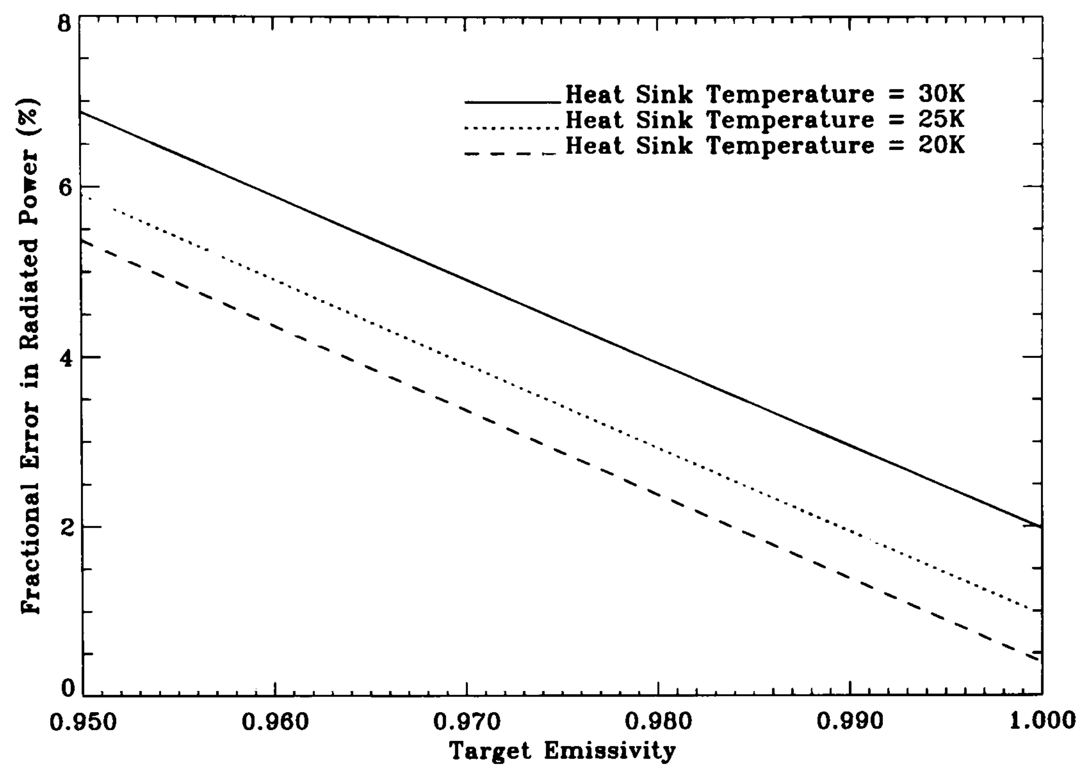

Figure 5-3: Variation of the error in the net power radiated to a space simulator target with target emissivity

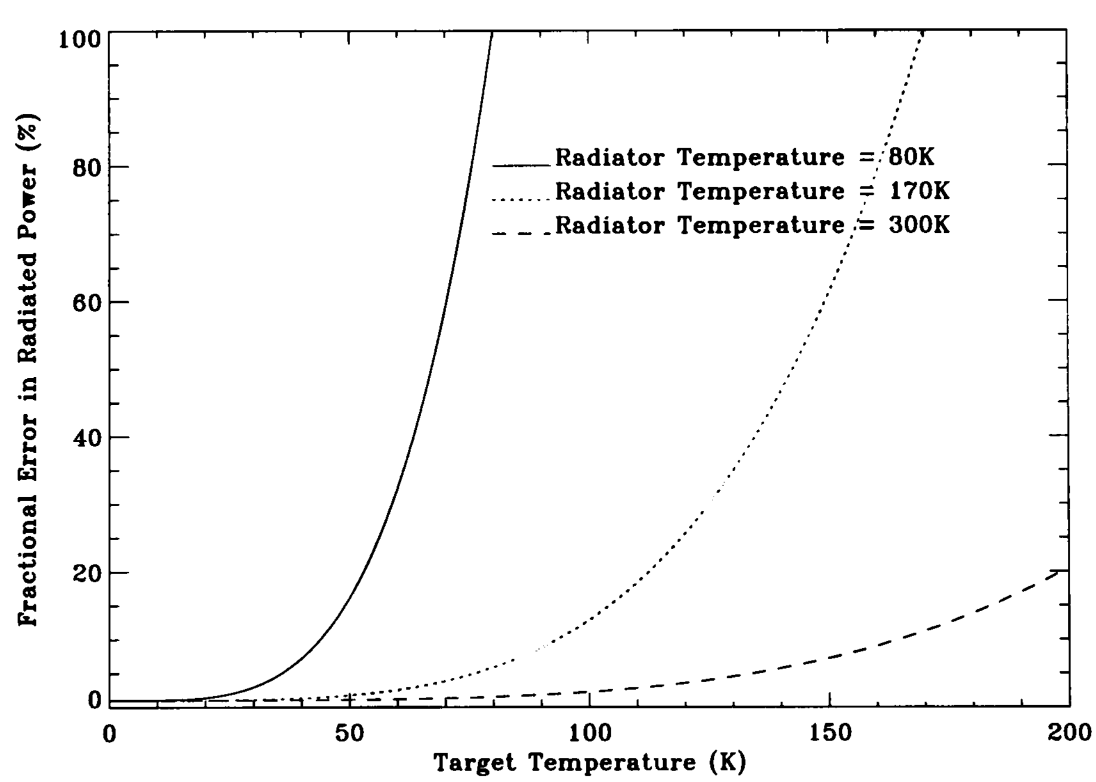

Figure 5-4: The effect of space simulator target temperature on the simulation error for a 0.99 emissivity target for various radiator temperatures.

The design specification for the space view black body determined from the above analysis is for an emissivity of at least 0.99 at a temperature of less than 25K when the cooler is at its operating temperature. A temperature of less than 140K is required during decontamination and start-up when the cooler patch is at 300K.

5.2.3 Instrument Simulator Specification

Simulation of the CIRS instrument is considerably easier than cold space. From a thermal standpoint the CIRS instrument is simply a 170K boundary temperature which should be variable to simulate non-ideal situations. The instrument simulator is a cooled aluminium block with a bolt hole arrangement similar to that on the real instrument to facilitate the attachment of the cooler. It is fitted with heaters and a thermometer for temperature control.

The radiative heat load onto the outside of the cone is not well defined because it varies with the viewing geometry and the spacecraft configuration and surface finishes. Two cooled half cone environment plates are fitted around the outside of the cone and tube to provide a known thermal environment during testing. They should be able to be controlled over a wide range of temperatures (room temperature to 170K) to enable the heat loads to be simulated when they become known.

5.3 Vacuum System

5.3.1 Chamber

The vacuum chamber is a cylindrical, stainless steel vessel approximately 1m in diameter and 1m high with dished ends. The lid of the chamber is hinged and counter-balanced as shown in Figure 5-2 to enable it to be opened easily. Access to the chamber for installing the cooler etc. is from the top of the tank. There are eight 200mm ports in the chamber which were used as shown in Table 5.1. Viton rubber 'O'-rings were used throughout for the vacuum seals.

The base of the chamber contains a flange on which the tripod support for the instrument simulator and environment panels is mounted using simple jacks. The jacks allow the position of the instrument simulator to be varied to enable the cooler to be positioned accurately in the chamber.

The large size of the chamber and its position in the clean room precluded the use of fibreglass heating tapes for baking the chamber to speed up outgassing from the surfaces.

Out-gassing from the chamber walls was minimised during commissioning by cleaning them first with detergent and water to remove heavy oils, then with acetone and finally alcohol. This process ensured that the chamber required only a few days to reach its minimum pressure without baking when first commissioned.

Table 5.1: Port assignments on the CIRS cooler test facility vacuum chamber.

Port	Position	Assignment
1	Base	High Vacuum Cryopump and Gate Valve
2	Base	Cooler for Space View Target
3	Base	Spare
4	Side	Vacuum Gauges, Roughing Line & Vent Line
5	Side	Electrical Leadthroughs
6	Side	Leadthrough for Instrument Simulator Cooling Gas Circuit
7	Side	Spare
8	Lid	RGA Mass Spectrometer

5.3.2 Pumping System

The high vacuum pump for the system is a CTI Cryogenics Cryo-Torr 8, 200mm diameter cryopump. The cryopump is attached to the chamber via a 200mm diameter electro-pneumatically operated gate valve which is used to isolate the cryopump during start-up. A separate compressor provides high pressure helium gas and the electrical supply for the cold head in the cryopump. The same compressor drives the cold head which cools the space simulator target. The schematic of the pumping system is shown in Figure 5-5.

To operate efficiently the cryopump adsorber must first be purged of water vapour by isolating it from the vacuum chamber and performing a number of cycles of evacuating the pump body using a roughing pump and venting with dry nitrogen gas. The pump body is then evacuated to approximately 1×10^{-1} torr using the roughing pump and the integral cold head started to reduce the adsorber temperature to less than 20K. Once the adsorber temperature reaches 20K the roughing pump is attached to the main vacuum chamber and the chamber evacuated to approximately 5×10^{-1}torr. The roughing pump is then isolated and the gate valve opened to enable the cryopump to pump the chamber to high vacuum.

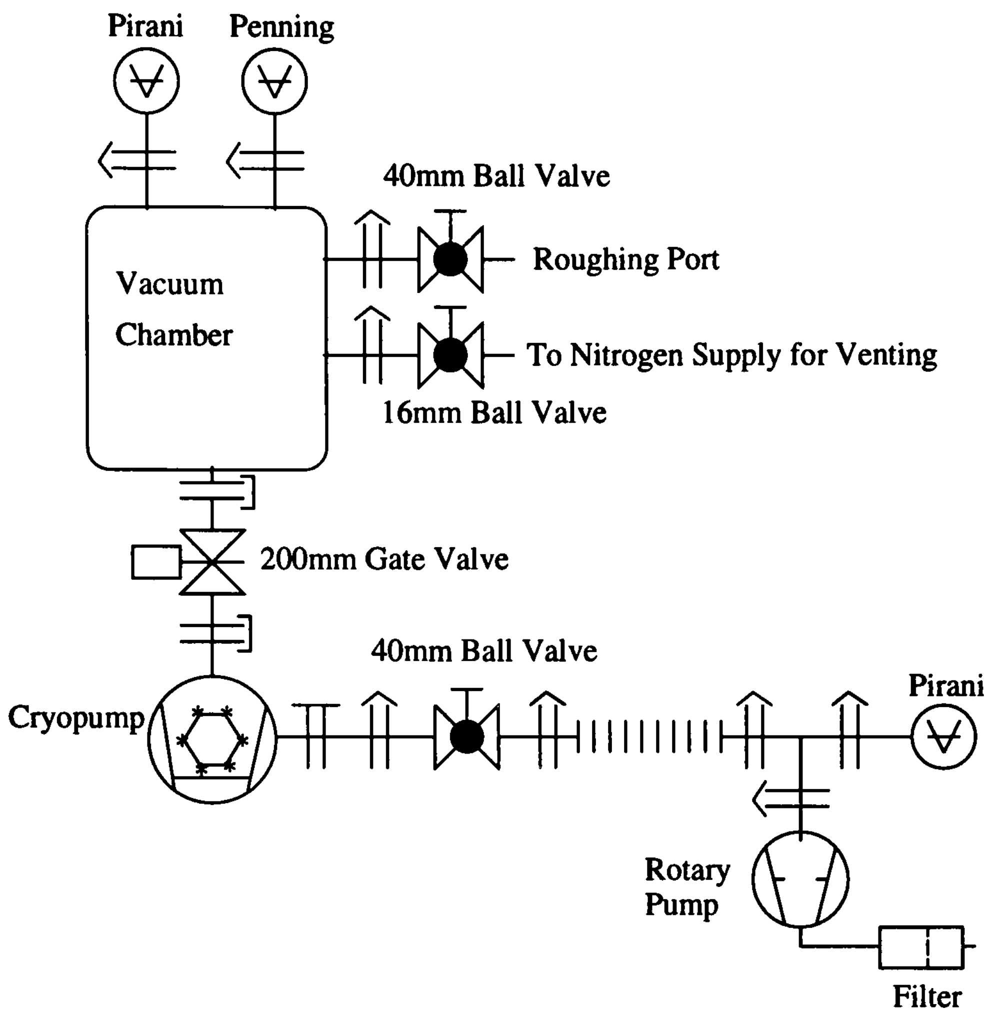

Figure 5-5: Schematic of the cooler test facility pumping system. Symbols conform to DIN 28 401 [42].

5.3.3 Instrumentation

The vacuum instrumentation for the system consists of a Pirani gauge for measuring the roughing pressure and a Penning gauge for high vacuum, giving a pressure measurement range of 1×10^{-7}–1×10^{3}torr. The cryopump has an external temperature gauge which is used to monitor the cool-down. The temperature gauge has a set point which was used as an inter-lock to prevent the gate valve being opened when the cryopump temperature was above 20K. This also served as a safety system in case of power failure because the gate valve will close as the cryopump warms up to reduce the risk of contaminating the components under test.

A quadrupole mass spectrometer residual gas analyser (RGA) was attached to the chamber to give an indication of the composition of the gas in the chamber when it is under vacuum.

5.3.4 Leadthroughs

The vacuum chamber required a number of leadthroughs for electrical connections to the test facility components and to the cooler, and a two way cryogenic fluid leadthrough for the cooling gas for the instrument simulator and environment panels. The electrical leadthroughs were Fischer hermetically sealed, multipole connectors. The cryogenic leadthrough was manufactured in-house and is described in the section describing the instrument simulator.

5.3.5 System Performance

The vacuum system performed well during the cooler testing with runs of over one week being made without the need to regenerate the cryopump. System pressures down to 2.0×10^{-7}torr were achieved after an over night pump down for most of the tests. When the chamber was operating at its lowest pressures the RGA revealed that the dominant component of the residual gas was water vapour. The main sources of the water vapour were most probably the paint on the cooler patch (which is water based) and the Dacron net in the MLI blanket. This assumption is based on the observed system pressures with the cooler installed compared to those without the cooler present in the chamber.

5.4 Space Simulator Black Body

The specification for the space simulator black body was derived in Section 5.2. This section describes the design of the space simulator in detail.

5.4.1 Description

The space view black body comprises a circular base plate (0.72m diameter) covered with 0.25" honeycomb cells cut at an angle so that the flat base plate is not directly visible when viewing at normal incidence. A 0.2m high cylindrical baffle extends from the base plate and is covered with an aperture plate to define the viewing aperture (see Figure 5-6). The base plate was manufactured from 5mm thick aluminium alloy, and the baffle and aperture plate from 1mm thick copper.

The inside surfaces were coated with with Nextel 2010 black paint and the outside was nickel plated in order to reduce the outer surface emissivity to minimise the heat leak into the 25K stage.

The black body is cooled by mounting it directly onto the second (25K) stage of a CTI Model 1020 two stage refrigerator which is driven using the same compressor as the vacuum system's cryopump. The first (80K) stage is used to cool a nickel plated copper radiation shield around the outside of the black body to minimise the heat leak into the second stage to ensure a low operating temperature was achieved.

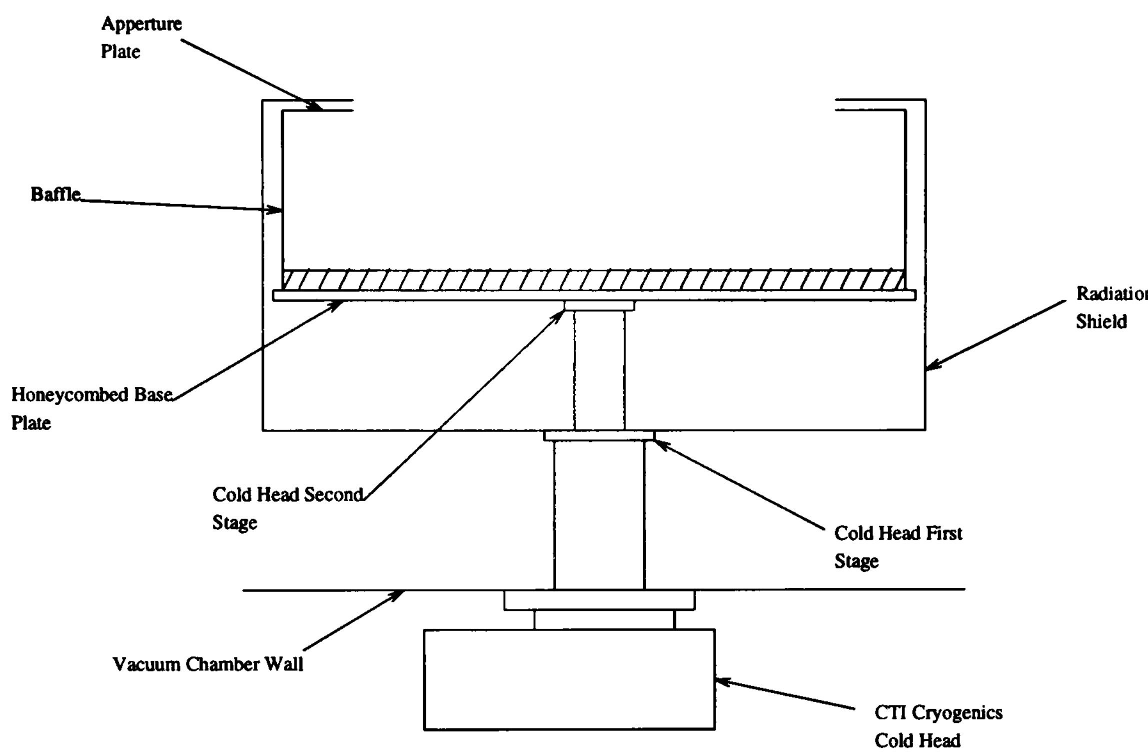

Figure 5-6: Space View Black Body

5.4.2 Black Body Effective Emissivity

The effective emissivity of a cavity is defined by:

$$\epsilon_{eff} = \frac{Q_{cavity}}{A_{aperture}\sigma T^4} \tag{5.6}$$

where Q_{cavity} is the power radiated from the cavity through its aperture, $A_{aperture}$ is the surface area of the cavity aperture and T is the temperature of the cavity. The denominator is the power radiated by a perfect black body of the same size as the cavity aperture.

The calculation of Q_{cavity} is not simple since the energy emitted from each surface undergoes multiple reflections within the cavity before finally being emitted through the aperture. Siegel & Howell [43] give a generalised method for dealing with radiation within cavities in which the cavity is assumed to be formed from N diffuse, grey, isothermal surfaces.

From the analysis of a general cavity given in [43], the following governing equations are obtained for each of the surfaces (k) in the cavity:

$$\sum_{j=1}^{N}(\delta_{kj} - (1 - \epsilon_k)F_{kj})q_{oj} = \epsilon_k \sigma T_k^4 \tag{5.7}$$

where N is the number of surfaces forming the cavity, δ_{kj} is the Kronecker delta, ϵ_k is the emissivity of the kth surface, F_{kj} is the view factor between surface k and surface j (see Appendix ??). q_{oj} is the total heat flux leaving surface j (both reflected and emitted energy), also known as the *radiosity* at surface j. T_k is the temperature of surface k. The above expression may be expressed in matrix form:

$$[A][J] = [C] \tag{5.8}$$

where the components of $[A]$, $a_{kj} = \delta_{kj} - (1 - \epsilon_k)F_{kj}$ and the components of the vector $[C]$, $c_k = \epsilon_k \sigma T_k^4$. $[J]$ is the vector of radiosities (q_{ok}). Equation 5.8 is solved for the radiosities at each surface by inverting the matrix $[A]$. i.e.

$$[J] = [A]^{-1}[C] \tag{5.9}$$

From the heat balance at a surface, the total heat lost by surface k is:

$$Q_k = A_k \left(q_{ok} - \sum_{j=1}^{N} F_{kj} q_{oj} \right) \tag{5.10}$$

The radiation model of the space view black body divides the base plate, baffle and aperture plate into a number of annular and cylindrical nodes. The software allows the number of annuli and cylinders to be varied in order to assess the accuracy of the solution and the aperture is represented by a single circle. The viewfactors between the nodes are calculated using analytical expressions derived from the basic expression for the viewfactor between two coaxial disks (see Appendix ??). The matrices $[A]$ and $[C]$ are then set up according to Equation 5.8. The temperature of the aperture is set to absolute zero and its emissivity to unity (so that all the energy striking it leaves the system). The temperatures and emissivities of the other surfaces are taken as input to the program. Matrix $[A]$ is inverted using a standard mathematical library subroutine [53]. The radiosity matrix $[J]$ is calculated using Equation 5.9.

The effective emissivity of the cavity is calculated by using Equation 5.10 to calculate the total heat flow into the aperture node. This is equal to Q_{cavity} in Equation 5.6 giving:

$$\epsilon_{eff} = \frac{\sum_{j=1}^{N}(\delta_{kj} - F_{kj})q_{oj}}{\sigma T^4}$$

where T is the assumed temperature of the cavity (the temperature of the base plate).

The model of the black body has been run for various resolutions (number of nodes in discretisation) in order to determine the resolution required to give accurate results. It was found that no variation of the apparent emissivity of the cavity was observed at resolutions greater than 20 nodes per large surface (base plate and baffle), so this was the resolution used in the other model runs. The aperture plate was represented by five nodes because of its significantly smaller area and memory limitations on the computer used for the calculation.

The effective emissivity of a black body of base diameter 0.72m, baffle height 0.2m with a 0.4m diameter aperture was calculated for various surface emissivities. The emissivity of the honeycombed base was determined by linear interpolation of the data presented in [41] for simple cylindrical cavities. This approach was demonstrated to be acceptable by constructing a geometric model of a honeycomb cell using the SSPTA radiation analysis program [37] and varying the angle of the cell, calculating the apparent emissivity at each angle assuming the cavity was isothermal. It was found that the effective emissivity of the honeycomb cell increased by less than 1.5% between vertical and a 45°angle, and that the assumption that the cavity was cylindrical rather than hexagonal in cross section had very little effect on the calculated emissivity. The assumption that the baseplate is formed from right, cylindrical cavities will therefore give a slightly pessimistic estimate for the emissivity of the whole black body.

Figure 5-7 shows the variation of the cavity effective emissivity with the surface emissivity. Clearly in order to meet the design requirement of $\epsilon_{eff} > 0.99$ using this design of black body then the surface emissivity must exceed 0.89.

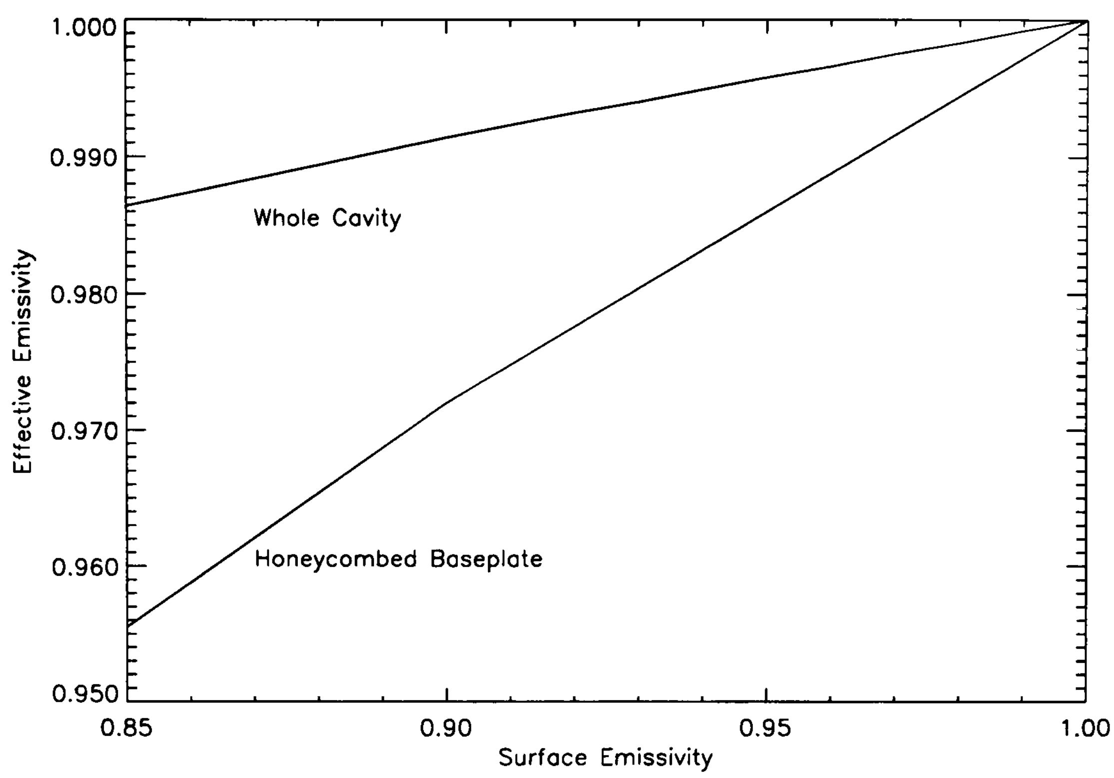

Figure 5-7: The variation of the space view black body emissivity with surface emissivity

5.4.3 Effect of Temperature Gradients

The analysis presented above assumed that the baseplate, baffle and aperture plate will all be at the same temperature (25K). In practice this will not be the case because only the base plate will be cooled only at its centre so there will be a radial temperature gradient along the baseplate.

Because the temperature of the cavity is taken to be the temperature of the baseplate at a point half the radius of the plate from the centre (i.e. the thermometer position), the *apparent* emissivity of the cavity will be reduced because less of the incident radiation will be absorbed. Note that the true emissivity does not change, simply the effective temperature has increased, but the analysis is simpler if we attribute the effect to a change in the effective emissivity.

The model was run for the cavity analysed above, but with various values used for the temperature of the baffle and with the base centre temperature held constant at 25K. The temperatures of the individual nodes in the base plate were calculated assuming the heat flow through the base plate to be constant at all radii, giving a logarithmic temperature gradient. For the model runs the baffle was assumed to be cooler than the baseplate in order to give a reduction in the apparent emissivity (the model assumes that the cavity emits to a cold heat sink (the aperture) rather than absorbs from a hotter source). The apparent emissivity was calculated assuming the temperature of the cavity to be the temperature of the baseplate at the half outer radius position. The results are shown in Figure 5-8. It can be seen that the temperature change should be less than approximately 0.7K for the apparent emissivity to remain above 0.985. The temperature change across the base plate is estimated in the Section 5.4.5.

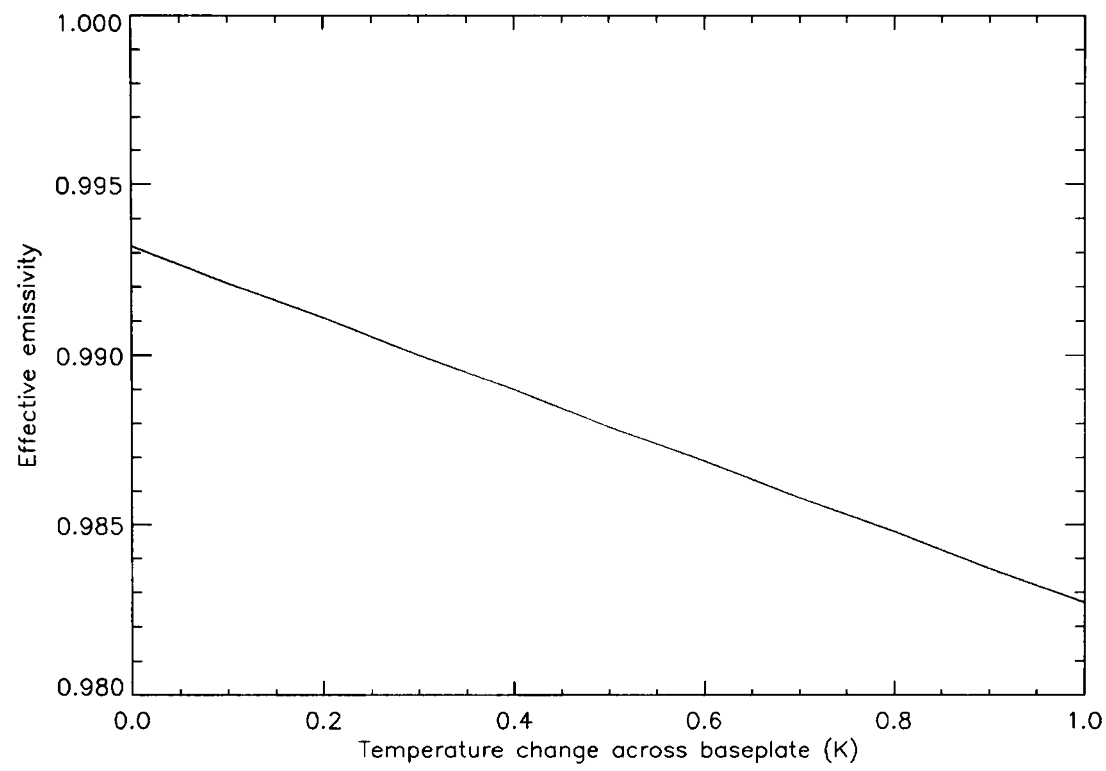

Figure 5-8: The variation of the space view black body effective emissivity with the temperature change along the base plate

5.4.4 Paint Selection

Many infra-red black paints have emissivity values quoted which exceed 0.95 [45][47] which would suggest that the specification of 0.89 stated above could easily be attained. Unfortunately most of the data presented is measured with the sample at room temperature (whereas our black body will be at 25K) and/or the total emissivity is determined by analysing spectral reflectance data. The spectral reflectance data generally covers the range 5–55μm which provides good coverage for 300K radiation, but only covers approximately 50% of 80K black body radiation. 98% of the energy of an 80K Planck function lies in the range 18–290μm . This makes the emissivity of the paints at low temperatures somewhat uncertain.

Nextel 101-C10 paint was chosen because this paint has been the most widely studied of the infra-red black paints, and some low temperature data exists for it:

- The spectral emissivity of the paint has been measured down to liquid nitrogen temperatures (77K) and showed very little change from the room temperature values (> 0.9 over the range 5–55μm) [46].

- The specular reflectance has been measured at low temperatures (7K) and long wavelengths (to 500μm) [45] and the results are similar to the other paints studied. It was found that the specular reflectance increased significantly when the sample was cooled from 300K to 7K.

In order to make an estimate of the total emissivity (and hence absorptivity) of the Nextel paint at low temperatures and for 80K radiation, the data published in [45] has been analysed. The data presented in [45] was in the form of specular reflectivity at various wavelengths. The data was converted into emissivity by assuming $\epsilon = (1 - \rho)$. Because the measurements do not include the diffuse component of the reflectivity, the values were corrected at short wavelengths (where diffuse reflection dominates) by decreasing the emissivity to 0.95 wherever it would appear to have a higher value. This forces the corrected emissivity to agree with the value measured by [47] at short wavelengths. No correction has been made at long wavelengths where it would be expected that specular reflection would dominate. The corrected spectral emissivity data is shown in Figure 5-9 along with an 80K Planck function.

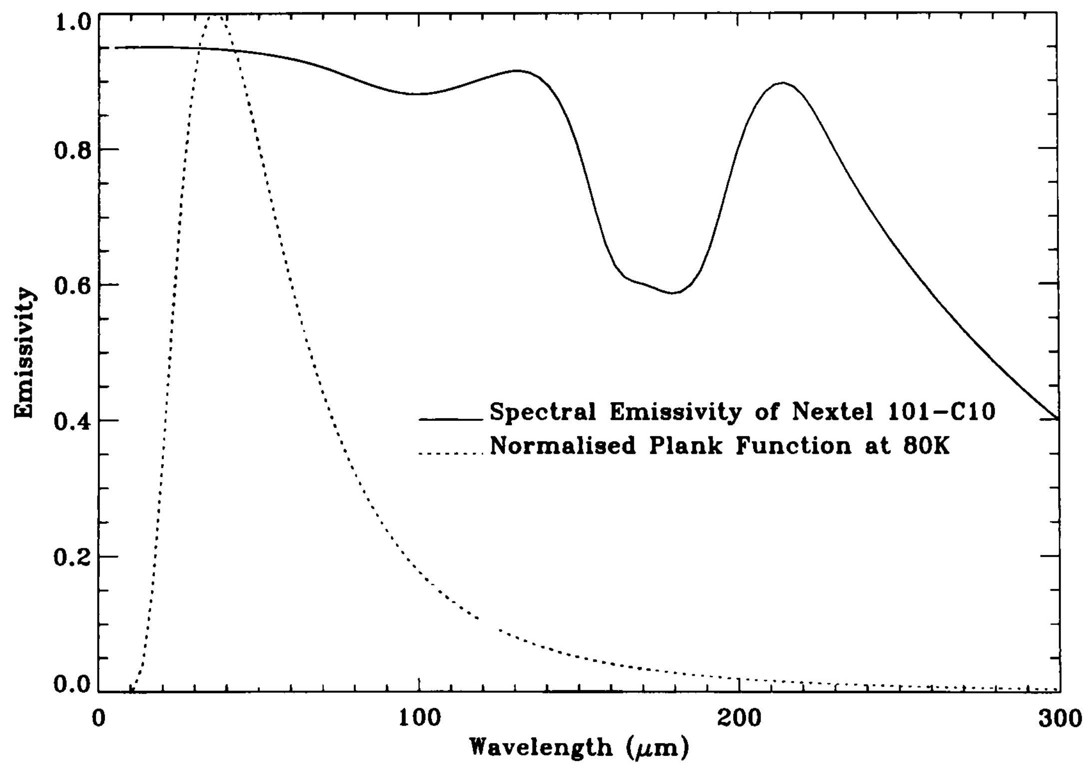

Figure 5-9: The Spectral Emissivity of Nextel 101-C10 Paint

The total emissivity of the paint for 80K radiation was calculated from the corrected spectral emissivity data by taking an average of the spectral emissivity data weighted against the 80K Planck function. The total emissivity for 80K radiation was calculated to be 0.919 which meets the 0.89 emissivity specification.

It should be noted that this calculated value is based on specular reflectivity data at 7K, rather than total reflectivity at 25K which would be optimum. The fact that only the specular component of the reflectivity was measured will tend to over-estimate the emissivity, and the data being taken at a lower temperature than will be used in practice will tend to give an under-estimate. Since the effect of reducing the temperature had only a small effect on the reflectivity below $100\mu m$ [46] where most of the 80K radiation is concentrated, it would be expected that there will be a net over-estimate of the emissivity. If we assume that the paint emissivity will lie in the range 0.90–0.92 the black body effective emissivity will lie in the range 0.991–0.993 which meets the design specification.

5.4.5 Black Body Thermal Design

As stated in section 5.4.1 the black body will be cooled using a two stage helium refrigerator. The unit which has been selected is a CTI-Cryogenics "Cryodyne 1020CP" which should give 35 watts of cooling at 77K and 12 watts at 20K on the first and second stages of the cooler respectively. The characteristic of the unit is shown in Figure 5-10.

In order to minimise parasitic heat loads into the space simulator, the simulator is mounted directly onto the second stage of the refrigerator. It was found that the refrigerator was sturdy enough not to require any further support, so the only heat load into the black body is the radiative load onto the outside surfaces from the radiation shield, and onto the inside from the CIRS cooler, plus the conductive heat load through the electrical cables for the thermometers and heaters.

An estimate of the heat loads onto the stages was made by assuming that the radiation shield at 80K views only the 300K chamber walls. If an emissivity of 0.05 is assumed for the radiation shield, a heat load of 37.4 watts is obtained.

The heat load onto the outside surface of the black body is estimated by assuming that it views only the shield at 80K and has an emissivity of 0.05, giving a heat load of 0.15 watts. The heat load into the aperture is calculated for two conditions: Normal

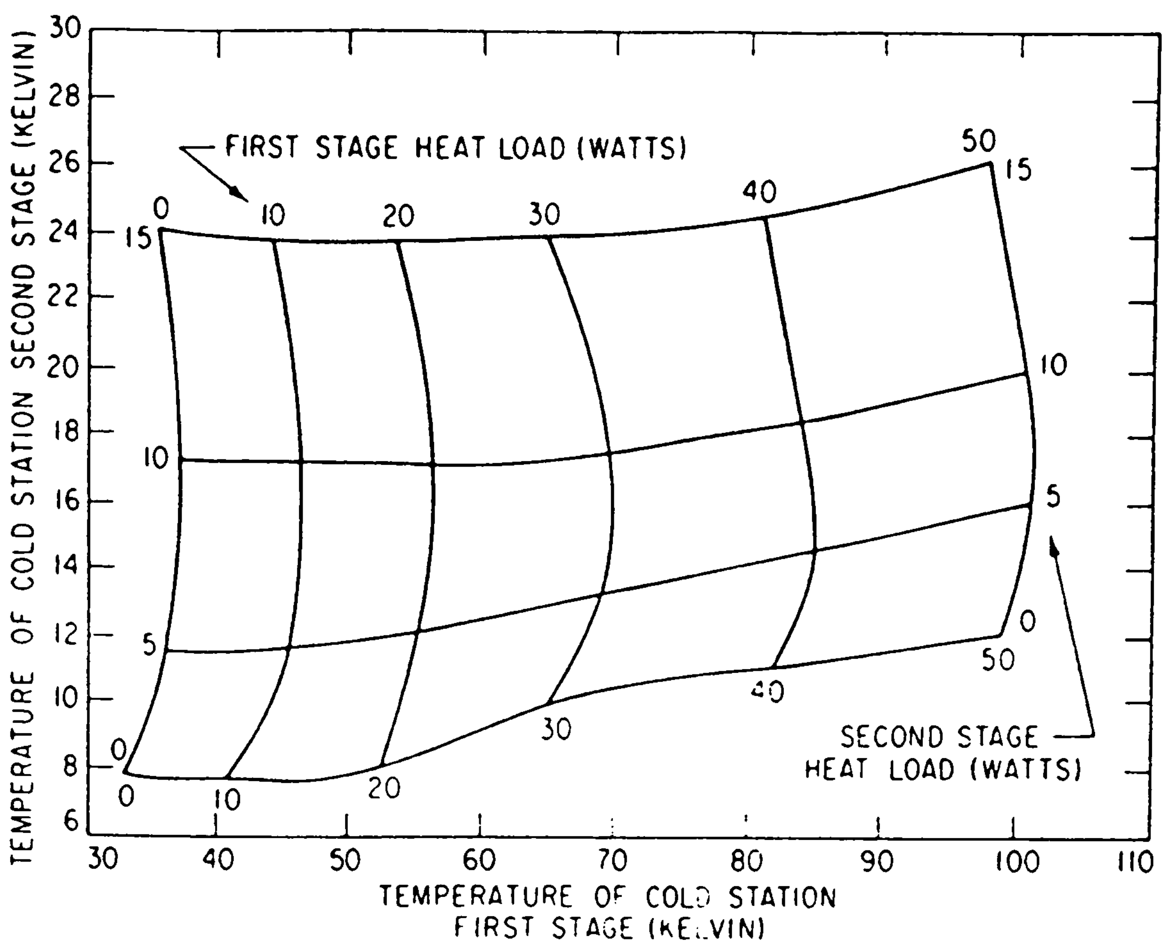

Figure 5-10: Typical Refrigeration Capacity of the CTI Cryogenics Model 1020C Cryodyne Cryocooler (Manufacturers' Data)

operation, in which case the aperture is assumed to view a 170K black body, and start up when it views a 300K black body. The heat loads are 6.01 watts under normal operation, and 58.32 watts at start up. The heat load through the electrical cable is estimated to be a further 1W.

From the manufacturers' data in Figure 5-10 it can be seen that with the heat leaks of 37.4 watts into the first stage, and 7.0 watts into the second stage, the black body should reach a temperature of approximately 15K, which is well within the 25K specification. In operation the space simulator has achieved temperatures below 15K with the cooler installed. The temperature achieved is slightly lower than that predicted because the radiation shield floats to a lower temperature than the 80K assumed — Temperatures below 70K were measured during the commissioning tests. In addition the assumption that the cooler had an effective temperature of 170K was an over-estimate because the annular radiator temperature was around 150K and the patch temperature around 80K.

The temperature gradient across the base plate may be estimated by assuming that all of the heat load is incident on the outer edge of the base plate. We determine the thermal resistance of the base plate between its outer edge and the thermometer mounting block

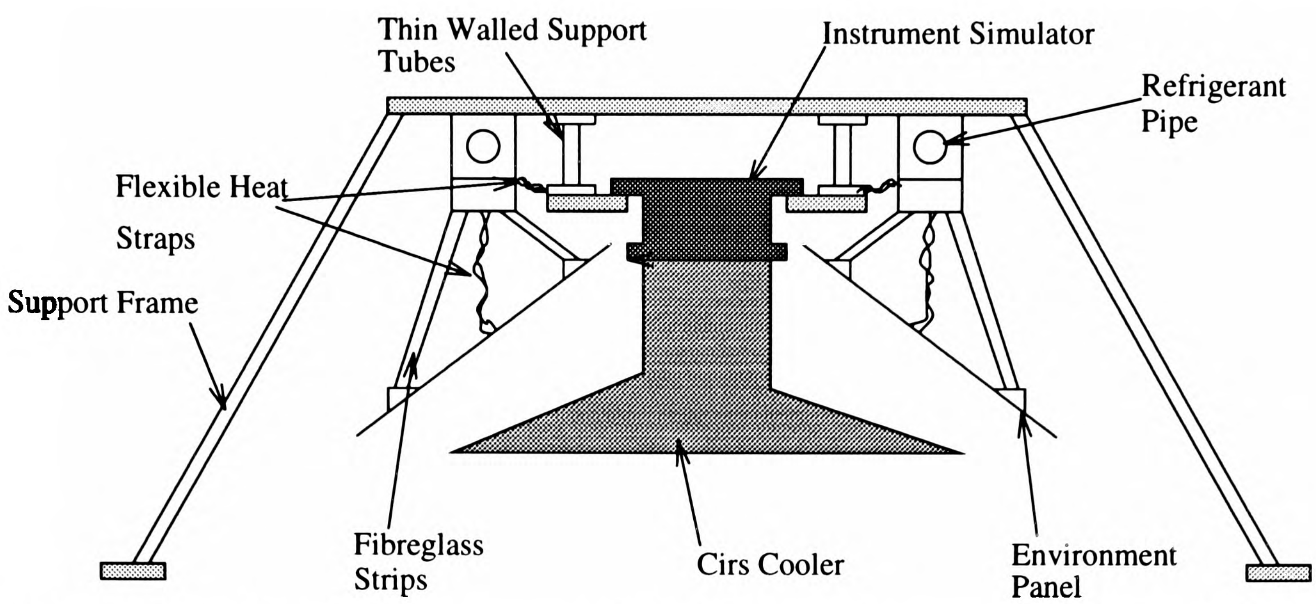

Figure 5-11: Schematic of the instrument interface, environment panels and their support structure

(at a radius of approximately 15cm), assuming a thermal conductivity of 200W/m/K and a thickness of 5mm which gives a resistance is approximately 1.1K/W. The total heat load through the base plate is around 800mW giving a worst case temperature rise of 0.88K between the thermometer and the edge of the base plate. In practice this temperature change will be reduced because a large proportion of the incident radiation will be absorbed along the base plate rather than at the very edge. When this was modelled using an SSPTA numerical model a temperature change of just under 0.5K was predicted. Both the models neglected the conduction through the honeycomb cells, which will also tend to reduce the temperature rise.

5.5 Instrument Interface/Environment Panels

5.5.1 Design Requirements

5.5.2 Description

The instrument interface is an aluminium alloy block with a flange on one end which has the same dimensions and bolt positions as the CIRS instrument. The other end of the block has a flange to mate with the mounting plate on the support frame.

The environment panels are half cone faceted shells manufactured from 1mm copper plate and then nickel plated. They completely surround the outside of the cooler in order to provide a known radiation environment for the cone and tube. The gaps between the

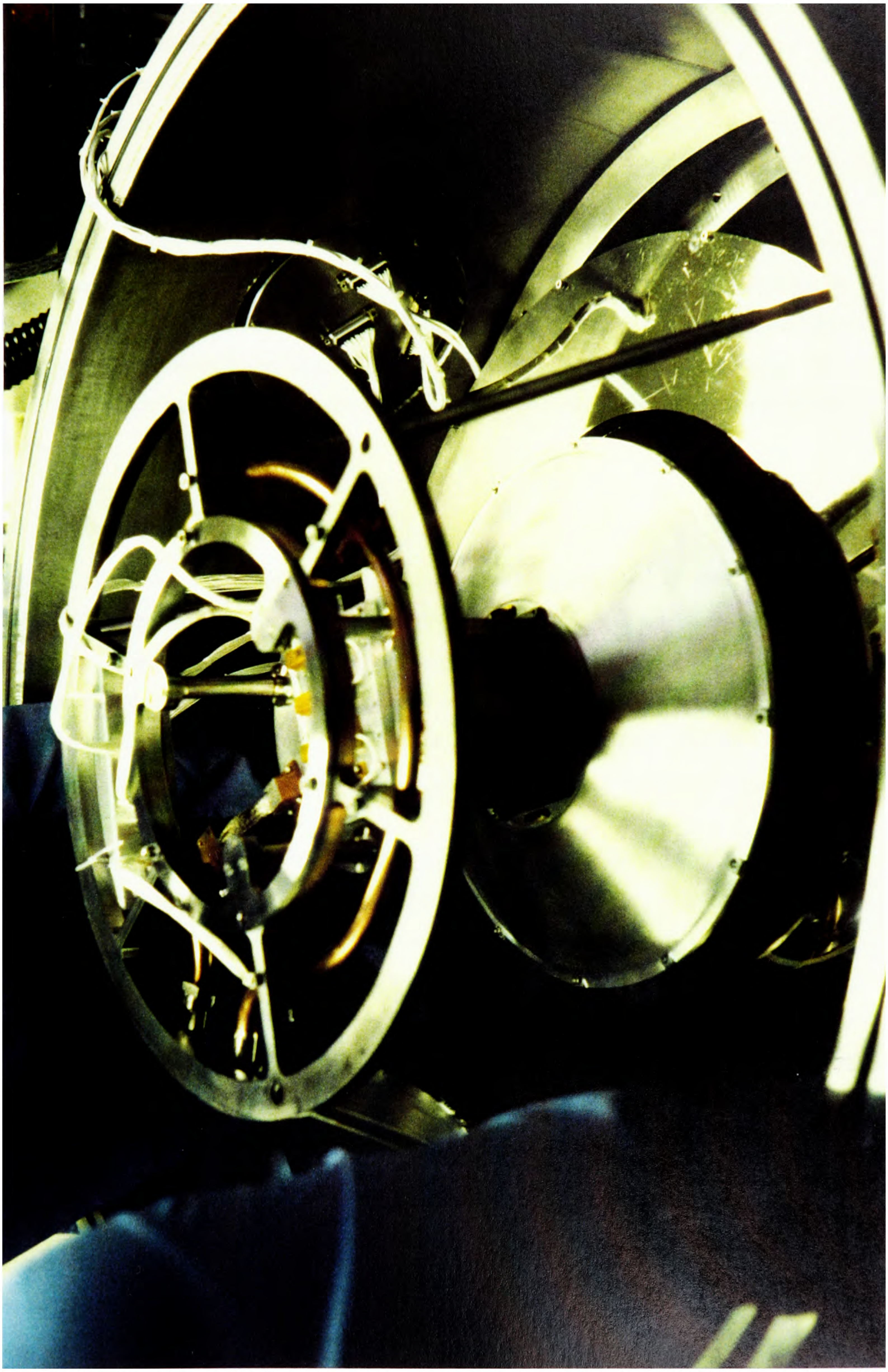

Figure 5-12: The DM CIRS cooler mounted on the instrument simulator in the vacuum chamber.

environment panels and the space simulator radiation shield are covered with aluminised mylar to ensure that no part of the cooler views the hot chamber walls.

The instrument simulator and the environment panels are mounted on a support frame formed from thin walled stainless steel tubing which attaches to a flange in the bottom of the vacuum chamber. This allows the cooler to be mounted in the aperture of the space simulator black body without any components actually touching the 20K stage so that the space simulator may reach its minimum temperature. The schematic of the assembly is shown in Figure 5-11. Figure 5-12 shows the cooler mounted from the instrument simulator being lowered into the aperture of the space simulator. The environment panels have been removed to check the positioning of the cooler within the aperture.

5.5.3 Thermal Design

In order to allow the instrument simulator and environment panels to be cooled, they must be thermally isolated from their support frame which will be close to ambient temperature. The instrument simulator is mounted from the frame using thin walled stainless steel tubes in order to provide a rigid mounting to ensure accurate positioning of the cooler within the space simulator aperture, while giving adequate thermal isolation. The environment panels do not require such rigid positioning so they are mounted from flat fibreglass bands.

The components are cooled using a Polycold P-200 cryogenerator. This is a commercial unit which circulates liquefied gas around a cooling circuit. The cooling circuit in this case is a ring of 0.5" copper tube which is connected to the Polycold unit using armoured stainless steel flexible hoses and a custom manufactured cryogenic leadthrough (Figure 5-13). The leadthrough works by moving the joint between the coolant pipes and the vacuum flange away from the body of the flange using thin walled stainless steel tubing. This reduces the heat leak between the flange at 300K and the tubing at around 150K because of the low thermal conductivity of the stainless steel tubing and the vacuum insulation on the inside of the leadthrough. The outside of the leadthrough and the external coolant hoses are covered with 'Armaflex' foam rubber insulation. The instrument simulator and environment panels are connected to the cooling circuit using short, flexible copper braid heat straps.

In operation temperatures as low as 158K have been achieved. Should lower temperatures be required in the future, there remain a number of options for improving the thermal performance such as reducing the radiative and conductive loads onto the components, and improving the insulation on the coolant lines outside the chamber.

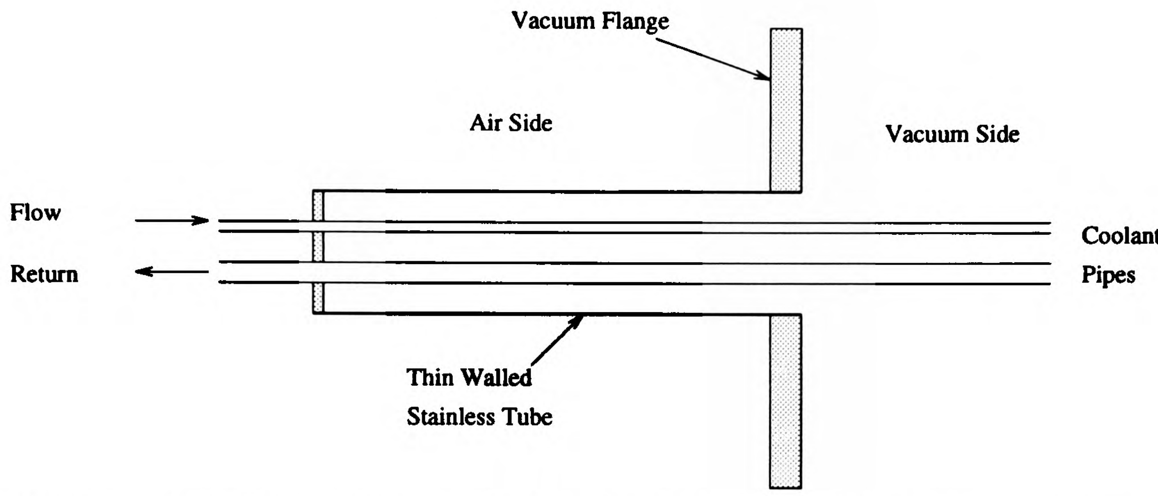

Figure 5-13: The cryogenic leadthrough for the Polycold gas circuit

5.6 Monitoring and Control System

The monitoring and control system for the cooler test facility is based around a Viglen 80386 25MHz computer running the Linux Unix-like operating system. Signals from the temperature sensors in the test facility and cooler are processed using electronics housed in a 19" rack system before being measured using a 12 bit analogue to digital converter (ADC) installed in the computer. Temperature controller heaters are controlled using a purpose built electronics unit which is programmed using a digital input/output card in the computer.

5.6.1 Electronics

Temperature Monitoring Electronics

The thermometers which were originally specified by GSFC for the cooler and adopted for the cooler test facility components were cryogenic thermistors with a resistance of 1MΩ at 80K, so the temperature monitor electronics were designed using a conventional, constant voltage, potential divider technique[49]. However delays in procuring the thermistors forced a change in the specification for the thermometers so industrial wire wound platinum resistance thermometers manufactured to BS1904:1984 Class B [50] were used.

Because the circuit boards had already been manufactured the basic measurement technique was left unchanged with the gain of the amplifier increased to account for the reduced signal from the potential divider. The bias resistor in the potential divider was sized to give a maximum bias current through the thermometer of 1.0mA. The gain of the amplifier was set to give the 0–4V input required by the PC-60A analogue to digital converter.

At the time of the initial cooler tests performed by the author neither the temperature monitor and control circuits, nor the cryogenic thermistors to be used on the flight model cooler were available, so a simple system was developed quickly to enable the tests to be performed. Industrial flat film platinum resistance thermometers similar to those used on the test facility components were used on the cooler and FPA. The resistance measurement circuit for the thermometers was a conventional constant current, four wire measurement circuit which was designed and constructed by Mark Sanders. The output was scaled to give a -4V to +4V output range in order to maximise the resolution of the measurement. The resolution attained was approximately 0.04K.

Heater Control Electronics

Temperature control of the thermal components of the test facility was provided using resistance heaters mounted on the components. The heaters were controlled by the computer using a software three term (PID) controller. The power supply for these heaters was a 6kW variac. The supply to individual heaters was switched by the computer using an electronic controller developed by E. Morgan. The controller switches the heater supplies using solid state relays. A pulse width modulation technique is used to give the required power output (0-100%). The computer programs the controller using its digital output board to supply a three bit number to select the channel and an 8 bit number to select the power. A power value of 0 gives almost zero power and a power value of 255 (decimal) gives 100% power.

5.6.2 Electrical Wiring

The wiring schematic for the cooler test facility is shown in Figure 5-14.

Separate electrical leadthroughs are used to take the signals from the cooler, the

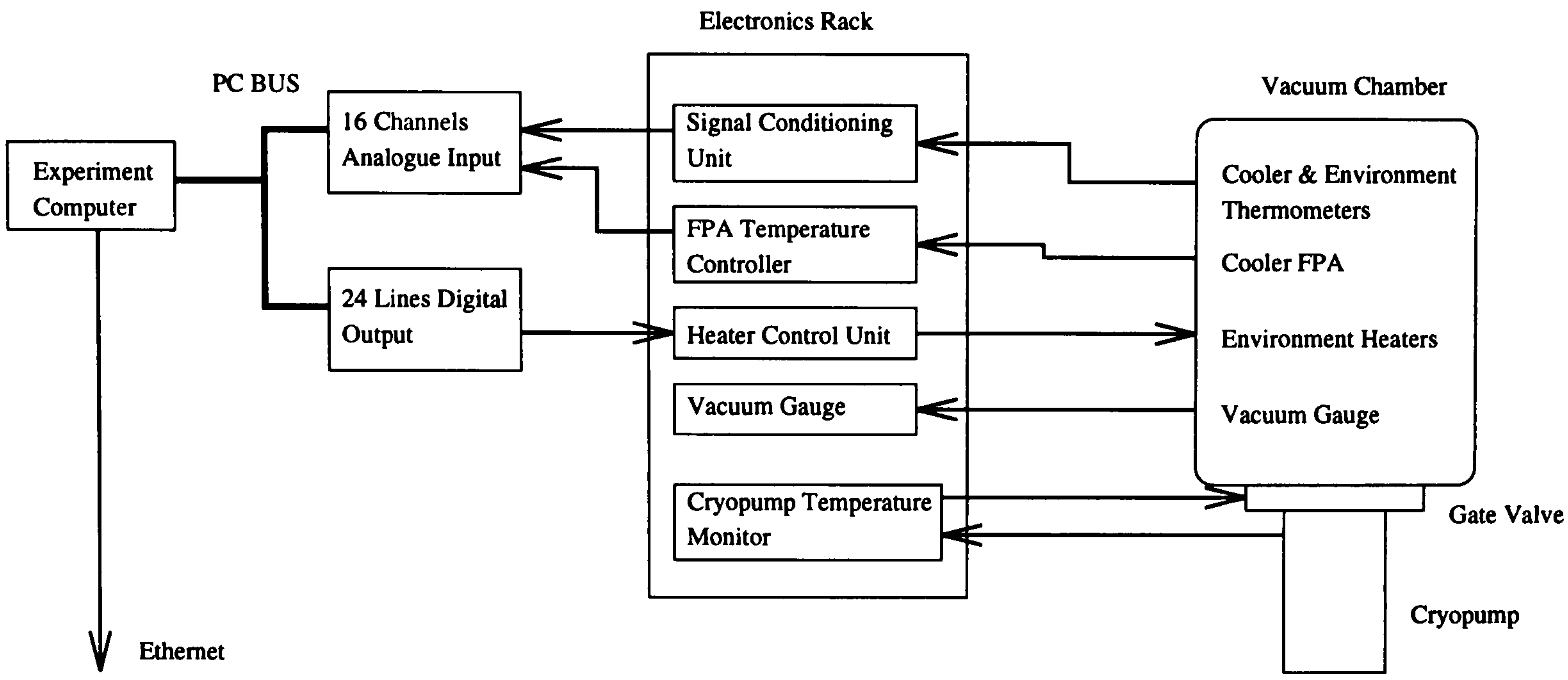

Figure 5-14: Electrical wiring in the cooler test facility

FPA, test facility thermometers, and test facility heaters from the vacuum chamber to the electronics rack.

Electrical connections to each thermal component of the test facility (Instrument simulator, space view black body and environment panels) are made using a single 15 way 'D' connector on each component. A simple wiring harness connects the components to an electrical junction box where the signals are routed to one of the dedicated electrical feedthroughs for heaters or thermometers.

Electrical connections to the CIRS cooler are made using a single harness connected directly to the cooler electrical feedthrough.

5.6.3 Software

The specification for the data acquisition and control software running on the test facility computer is that it should:

- Log the temperatures of the cooler thermometers and the test facility components at a regular, user specified interval and write the data to a file for later analysis.
- Enable the user to program the test facility heaters to given power levels.
- Control the temperatures of the test facility components to user specified set points.
- Provide a constantly updated display of the temperatures of components, the temperature controller set points and the heater powers on the screen.

It was decided that rather than using the conventional MS-DOS operating system on the computer, which is a single user operating system, the computer should run the Linux, Unix-like operating system which is available under the Gnu public licence. Using a Unix-like operating system had the advantage that the state of the system could be monitored remotely by logging into the computer over the department's local area network and examining the output files, and that the software could be updated and re-compiled on the computer while the console was controlling an experiment. This also meant that it was not necessary to enter the clean room while developing the software.

The control program itself is a simple continuous loop which reads each temperature in turn while monitoring the keyboard for operator intervention, and calculating the heater powers required using a standard three term control algorithm. The software holds the most recent temperature measured for each channel in memory, and after the required period between recording data has elapsed, it writes the most recent set of temperatures to the output file. In fact four output files are produced - a log file which records all operator commands and their effects, and three data files, one for each level of data processing from raw counts from the analogue to digital converter to temperature. The reason for writing more than one output file was to enable the system performance to be checked easily, and to allow the data to be re-processed simply should an error in calibration have been found at a later date.

5.7 Test Facility Operating Procedure

The procedure for operating the test facility was developed to minimise the risk of damaging the cooler, either by physically damaging it by dropping, or by contaminating the gold surfaces in the cooler and FPA.

The sequence observed when performing a cool-down test on the cooler and/or FPA is as follows:

1. The cryopump is first started by roughing out the pump body with a mechanical pump, and starting the cryopump cold head.

2. The cooler and FPA are attached to the instrument simulator block on an assembly bench outside of the chamber. The assembly will then balance safely on the

instrument simulator with the FPA enclosed to ensure it is not damaged.

3. The tripod support for the instrument simulator is raised high in the chamber using simple jacks and the instrument simulator and cooler are attached to the support. The construction of the support and instrument simulator is such that the cooler and instrument simulator are supported without the need for bolts so the risk of dropping them is reduced. Bolts are used to fasten the simulator to the support in order to increase the thermal contact between them.

4. The jacks are lowered until the cooler patch and annular radiator are held in the aperture of the space simulator without touching the space simulator itself.

5. The environment panels are attached around the outside of the cooler and any gaps sealed with aluminised mylar or aluminium tape. This ensures that the cooler does not see the hot chamber walls, only the environment panels.

6. The electrical harnesses are connected to the leadthroughs and the connections checked.

7. The chamber lid is closed and the chamber roughed out to approximately 1×10^{-1}torr using the rotary vane vacuum pump. The gate valve is then opened to expose the cryopump and reduce the system pressure to $<5\times10^{-6}$ torr.

8. The space simulator cold head and the Polycold refrigerator for the instrument simulator and environment panels are started simultaneously. In practice the Polycold cools far faster than the space simulator so the Polycold gas circuit acts as a secondary cryopump in preference to the space simulator.

The CIRS cooler reaches its equilibrium temperature approximately 36 hours after starting the space simulator cold head.

5.8 Test Facility Performance

5.8.1 Vacuum System

As stated previously the vacuum system performed well, with pressures as low as 2×10^{-7}torr were attained for long periods. The CTI compressor which drives the cryopump failed twice during commissioning and initial testing. On both occasions the failure was due to the a solenoid valve in the oil cooling circuit failing and the compressor over heat protection tripping the unit. After the compressor trip the cryopump started to warm up and the gate valve was closed automatically by the cryopump temperature monitor unit to prevent condensible materials re-entering the vacuum chamber.

5.8.2 Thermal

The thermal performance of the test facility was similar to the predictions — The instrument simulator and environment panels attain temperatures below 170K and the space simulator easily reached its 25K design temperature for every test. Figure 5-15 shows typical cool down curves for the test facility components. The cool down characteristic of the space simulator has an unusual shape. The initial cool down is approximately linear, then the slope increases significantly when the cold head reaches approximately 80K. It decreases very rapidly to zero when the cold head reaches its operating temperature. This characteristic shape has been observed both with and without significant thermal mass and radiative loads on the second stage of the cooler. Commissioning tests revealed that the transition to the steep part of the curve corresponds to the point where the temperature of the second stage of the cooler approaches the temperature of the first stage — Before that point the second stage was trailing the first at a higher temperature so the second stage was being cooled mostly by conduction from the first. Once the temperatures are similar the second stage cooler begins to work efficiently to increase the cooling rate.

The other components follow more conventional exponential cooling curves to reach their equilibrium values. The rapid cool down of the instrument simulator is achieved because the Polycold refrigerator has an extremely high cooling power (200W) at higher temperatures. The rapid cool down property is useful for operation of the test facility because it ensures that the Polycold cooling pipes are the coldest part of the system during the initial cool down so they will tend to act as a water vapour cryopump to reduce contamination onto the space simulator and the CIRS cooler which cool far more slowly.

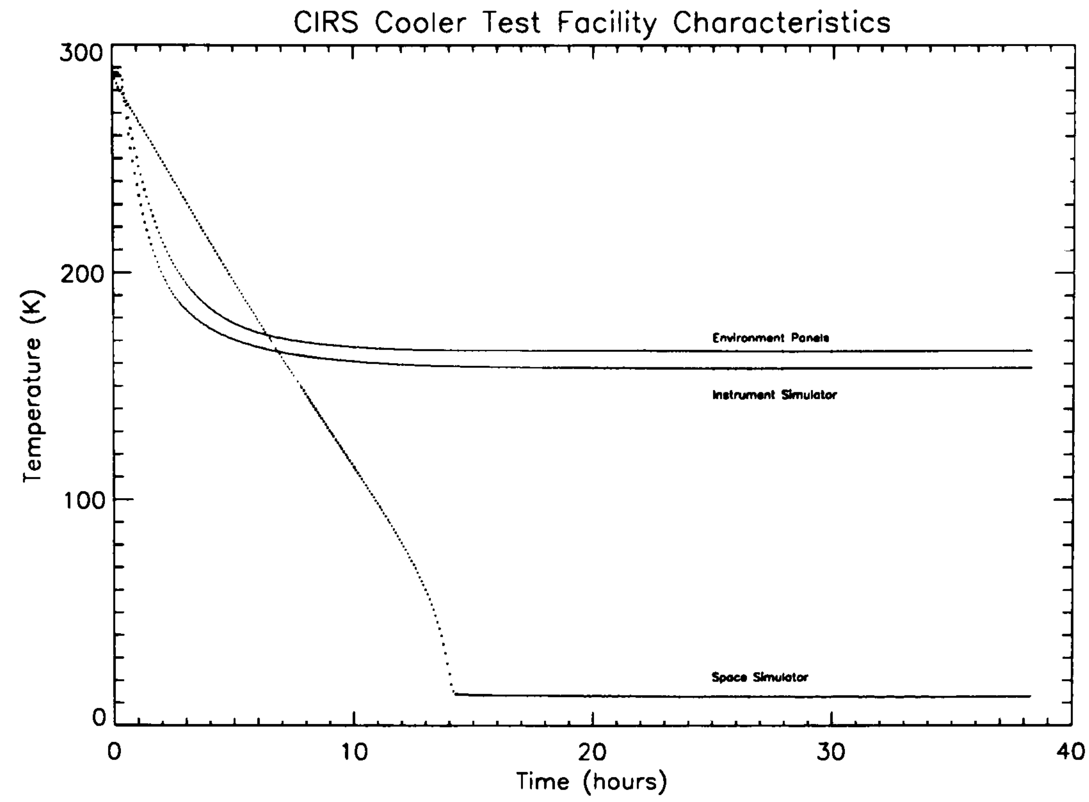

Figure 5-15: Typical cool down curves for the cooler test facility components

5.8.3 Data Acquisition and Control System

The data acquisition and control system performed well after some initial problems with the computer software crashing after several hours of operation. The software temperature controllers performed well because the temperature of the clean room was controlled, giving very few temperature fluctuations within the tank for the controllers to deal with.

setcounterchapter5

Chapter 6

Test Results

This chapter describes the thermal tests performed and the results obtained during the testing of the development model (DM) CIRS cooler and FPA. The results are compared to the thermal models described in Chapter 3 and an attempt is made to fit the model parameters to the results obtained.

The test sequence described below was determined partly by a desire to build up the cooler gradually to enable the effects of adding new components to be assessed, and partly by the availability of components at the time of a particular test. The manufacture of the titanium alloy cone was a particular problem so it was necessary to use an aluminium alloy cone for most of the tests described in this chapter. This resulted in a reduced performance to that predicted in Chapter 3. A number of tests were performed on the complete cooler by the remainder of the CIRS team after the author had left the project.

The DM cooler used for the majority of the tests is shown in Figures 6-1 and 6-2. Figure 6-1 shows the aluminium cone attached to the titanium tube. The panels for the preamplifiers are attached to the tube and the electrical connector for the thermometers is fitted to the top of the cone. Figure 6-2 shows the patch mounted on the cone and tube. The unpainted aluminium radiator is shown in position.

Most of the components used in the tests were manufactured by sub-contractors to detailed designs produced by T. Vellacott based on the work described in Chapter 3. The author was responsible for the assembly of the cooler, installing it in the test facility and the operation of the facility during the tests.

The tests performed are described in Section 6.1. The results are compared to the

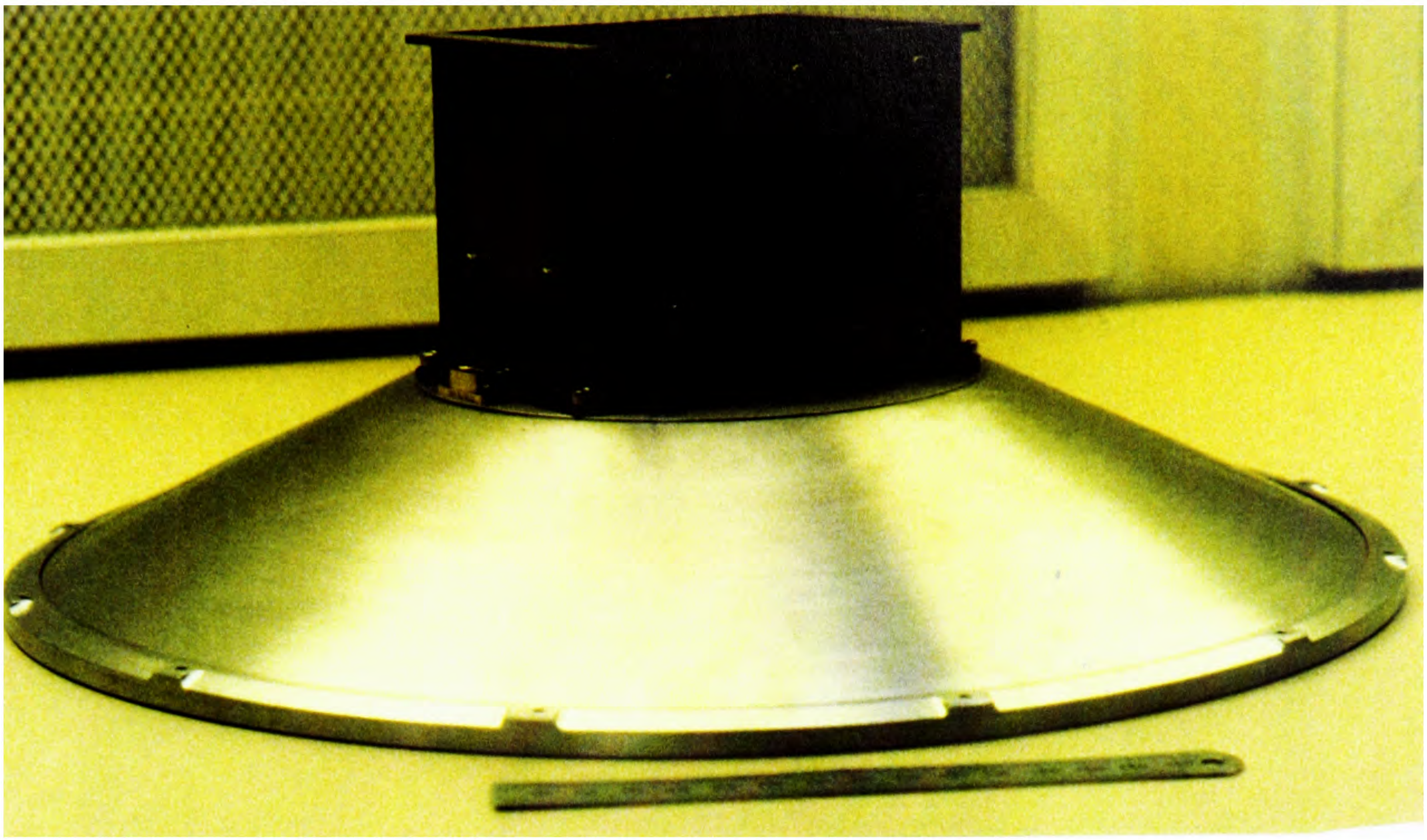

Figure 6-1: The DM cooler aluminium cone and titanium tube.

thermal model predictions in Section 6.2.

6.1 Cooler Test Results

Table 6.1 summarises the tests performed on the DM CIRS cooler and the results obtained. The individual tests are discussed in detail below.

6.1.1 Test 01 — 04 August 1993

The object of this first test to be performed on the DM CIRS cooler was to check that the test facility was functioning correctly and the basic principle of operation of the cooler was correct. The simplest cooler which could be constructed was assembled. The cooler comprised an aluminium cone, a titanium tube, the patch painted with MSA94B paint and the suspension ring. The patch was suspended from the suspension ring by titanium alloy wires. Six fibreglass retaining posts for the MLI blanket were attached to the back of the patch, but the blanket was not installed. Platinum resistance thermometers (PRTs) were attached to the back of the patch, the suspension ring, and the small end of the

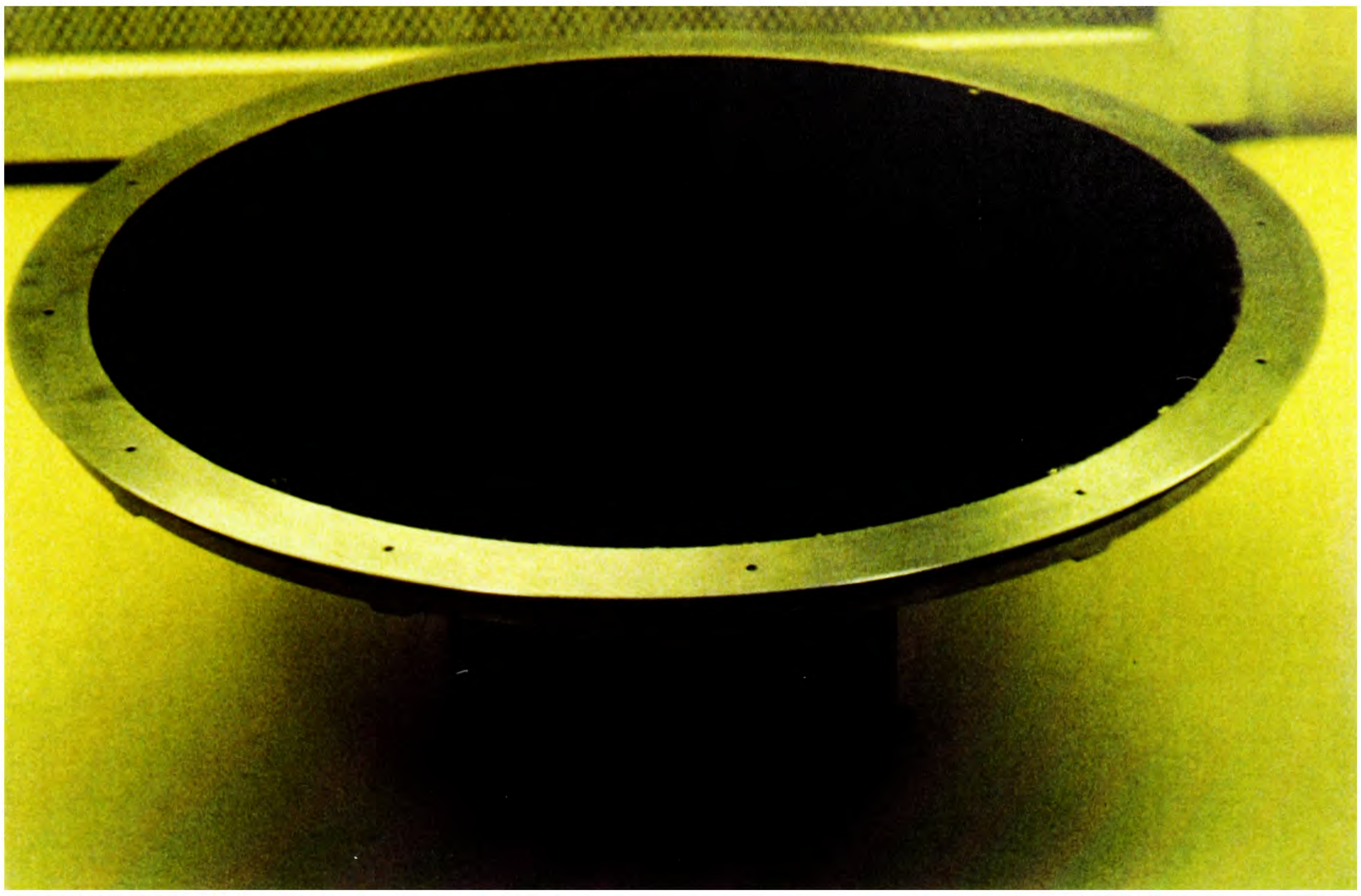

Figure 6-2: The DM cooler with the patch installed. (The unpainted annular radiator is shown in position.)

cone. The thermometer on the suspension ring was not well mounted so the temperature it reads is likely to be lower than the true value. The electrical connections between the thermometer on the patch and the cone were made using a 25mm long piece of commercially produced four way, 50μm diameter constantan conductor ribbon cable.

At the time of the experiment the Polycold unit which cools the instrument simulator and the environment panels was not installed so the temperatures of these components were allowed to float.

The vacuum chamber was pumped down over night, then the space simulator cooler was started. The space simulator cooled to its operating temperature of about 19K in approximately 14 hours and that the patch temperature closely followed the temperature of the space simulator until close to the base temperature of the patch. The patch temperature reached 123.9K in around 25 hours. The temperatures of the other boundaries (the instrument simulator and the environment panels) fell very slowly because they were not actively cooled. The instrument simulator reached a minimum temperature of 271.5K, and the environment panels 274.9K.

Table 6.1: Results obtained during the testing of the DM CIRS cooler. T_i is the temperature of the instrument simulator, T_e is the temperature of the environment panels, T_{ct} is the temperature of the top of the cone, T_{cb} is the temperature of the base of the cone and T_p is the patch temperature at thermal equilibrium with no heaters switched on. All temperatures are measured in Kevin.

Test	Date	Configuration	T_i	T_e	T_{ct}	T_{cb}	T_p
01	04aug93	Al Cone, Ti Tube	271.5	274.9	241.2	236.4	123.9
02	10aug93	Al Cone, Ti Tube	157.8	258.8	187.4	186.1	92.9
03	20aug93	Al Cone, Ti Tube, Patch MLI	269.0 169.9	269.8 269.5	245.8 199.9	235.2 196.0	95.7 79.0
04a	20sep93	Al Cone, Ti Tube, Patch MLI Cold Finger	160.0	259.7	196.5	192.4	78.1
04b	18oct93	Repeat of 04a	166.7	259.9	196.3	196.1	77.7
05a	28sep93	Al Cone, Ti Tube, Patch MLI Cold Finger, Annular Radiator	166.6	260.5	181.0	176.6	82.8
05b	14oct93	Repeat of 05a	158.1	259.2	175.3	173.8	78.8
06	20oct93	As 05a with spacers between annular radiator and suspension ring	166.4	258.5	178.8	177.3	80.8
07	22oct93	As 05a with silicone grease in joints between annular radiator, suspension ring, cone and tube.	158.2	257.4	175.2	173.5	78.9
08a	25oct93	As 05a with tidied-up patch (Al Tape around edge)	168.1	259.5	180.7	179.0	79.7
08b	29oct93	As 08a	196.9	260.0	191.0	197.9	88.0
09	19nov93	Ti Cone, Ti Tube, Patch MLI, Cold Finger, Annular Radiator, Dummy Common Carrier.	168.7	260.2	201.4	176.4	84.5
10	25nov93	Repeat of 09 with Cooled Environment.	157.4	164.9	157.7	140.8	69.8
12	28mar94	Ti Cone, Al Tube, Patch MLI, Annular Radiator, Cold Finger Flexible link & FPA.	169.9	170.5	162.6	153.4	75.6

6.1.2 Test 02 — 10 August 1993

For this test the gas circuit for the Polycold refrigerator was installed to allow the instrument simulator to be cooled. The environment panels were un-cooled. The instrument simulator was not thermostated so it was allowed to cool to its minimum attainable temperature. The configuration of the cooler for this test was exactly the same as for Test 01 on 04 August.

The cooler was cooled in a similar manner to Test 01. The operating temperature of the space simulator was 14.3K. The instrument simulator reached a temperature of 157.8K with the environment panels at 258.8K.

The final patch temperature of 92.9K represents a 31.0K improvement over the previous test. The instrument simulator temperature changed by 113.7K so we can deduce that the sensitivity of the patch temperature to the instrument temperature ($\frac{\partial T_p}{\partial T_i}$) for this cooler configuration is 0.27K/K.

6.1.3 Test 03 — 20 August 1993

The object of this test was to assess the effect of adding the MLI blanket to the back of the patch. A MLI blanket comprising five layers of aluminium foil separated by Dacron net spacer was installed in the cooler and secured with fibreglass washers and circlips. A simple cool-down test was performed with the instrument simulator thermostated to 269.0K. The environment panels floated to 269.8K and the patch reached a minimum temperature of 95.7K. The instrument simulator temperature was reduced to 169.9 and the patch temperature fell to 79.0K.

In order to assess the effect of adding the MLI blanket by comparing these results to Test 01, it is first necessary to correct the patch temperature to account for the instrument temperatures not being the same — The instrument temperature in this test was 1.7K less than for Test 01. However the sensitivity of the cooler to the instrument temperature was determined to be 0.27K/K, so the corrected patch temperature is $95.7 + 0.27 \times 1.7 = 96.2$K. This is the the temperature which the patch would have reached if the instrument temperature was the same as in Test 01.

Comparing this corrected patch temperature (96.2K) to that obtained in Test 01 (123.9K) shows that the patch temperature was reduced by 27.9K by adding the MLI blanket. Now the thermal models predict the heat load sensitivity of the cooler to be approximately 0.1K/mW (See Chapter 3), so this reduction of 27.7K is equivalent to a reduction in the heat load of 277mW.

6.1.4 Test 04 — 20 Sep 93 and 18 Oct 93

The two tests 04a and 04b were performed on identical cooler configurations. The cooler comprised a titanium alloy tube, aluminium cone, suspension ring, patch and cold finger. A five layer MLI blanket was attached to the back of the patch. Between the two tests the cooler was completely dismantled and re-assembled.

It is surprising to note the difference in the temperature change along the cone — For both tests the cone top was at a similar temperature (approximately 196.4K), but during Test 04a the temperature drop along the length of the cone was approximately 4.1K whereas for Test 04b the temperature drop was only 0.2K. In addition it is noted that the patch reached a lower temperature during Test 04b. This result suggests that there was less radiative or conductive coupling between the cone and the patch during 04b compared to the first test which was probably caused by the patch MLI blanket being assembled more carefully the second time with greater care being taken to ensure that the hole for the cold finger was large enough that the aluminium shields did not touch the cold finger and add to the heat losses.

6.1.5 Test 05 — 28 Sep 93 and 14 Oct 93

For these tests the annular radiator was added to the cooler used in Tests 04. The radiator was painted with MSA94B paint and had been baked in a vacuum oven over night to drive off the water from the paint.

Test 05a produced a surprise result when the equilibrium patch temperature was higher than for Test 04a without the annular radiator, even though the cone top temperature was 15.5K lower than the previous test. Upon removing the cooler from the test facility it was discovered that one of the patch suspension wires had broken and it appeared that one of the patch bridges was in contact with the annular radiator. For this reason it was decided to repeat Tests 4a and 5a. The results for the repeat of Test 04a are discussed above.

The repeat (Test 05b) was performed on the cooler after it had been completely dismantled and re-assembled. Unfortunately the instrument simulator heater failed during the cool down so the instrument simulator reached a lower equilibrium temperature than Test 05a. The equilibrium patch temperature was 1.1K *higher* than Test 04b which was performed on the cooler without the annular radiator and under similar conditions. Possible reasons for this result are discussed in Section 6.2 below.

If we assume that the apparent fouling of the annular radiator on the patch in Test 5a was either insignificant or the components were not fouling at the operating temperature (see discussion of Test 6) we can use these results to determine a second value for the sensitivity of the patch to the instrument temperature. The sensitivity obtained by comparing Tests 5a and 5b is 0.47K/K. Similarly the sensitivity of the patch temperature to the cone top temperature is calculated as 0.701K/K.

6.1.6 Test 06 — 20 Oct 93

Following the curious results obtained for Tests 05a and 05b, a test was performed to determine conclusively whether or not the annular radiator was touching the patch and causing the increased heat load. 0.5mm thick aluminium spacers were fitted between the annular radiator and the suspension ring to increase the clearance between the patch bridges and the annular radiator. The spacers were smeared with a thin layer of silicone vacuum grease to ensure that there was no significant increase in the thermal resistance between the annular radiator and the suspension ring.

At equilibrium the patch temperature (80.8K) was between the temperatures attained in Tests 05a and 05b. This proves that the unexpected reduction in the cooler performance was not caused by the annular radiator fouling on the patch suspension wires — If they had been, it would be expected to see a significant improvement in the cooler performance compared to Tests 05a and 05b.

6.1.7 Test 07 — 22 Oct 93

In all the tests performed previously, the cone temperature had been consistently higher than that predicted by the models. This was likely to be caused either by the emissivity of the outside of the cone and tube being higher than the value used in the models, or by contact resistances between the cone and the annular radiator allowing the annular radiator to float to a lower temperature than the cone base. In order to test whether there were significant contact resistances between the cone and the annular radiator, the joints between the tube and cone, the cone and the suspension ring, and the suspension ring and the annular radiator were smeared with a thin layer of silicone vacuum grease. This will ensure good thermal contact at the joints. When the cooler was re-installed in the test facility and cooled down, both the cone and the patch temperatures were very similar to those achieved in Test 05b which had the same instrument temperature.

This confirms the assumption that the thermal contact at the interfaces is good without the need for thermal contact greases etc.

6.1.8 Test 08 — 25 Oct 93

The thermal models of the cooler patch assume that the edge of the patch is a clean, metallic surface. The patch used in the tests had a fillet of glue around the edge where the front and back skins of the patch were bonded together. Additionally the edge of the radiator honeycomb was open in places allowing the black radiator surface to view the underside of the annular radiator. Test 07 was performed to determine the extent of the adverse effect caused by these defects. A strip of aluminium tape was fastened around the edge of the patch skins and around the outside of the radiator to ensure that the surfaces viewing the annular radiator and suspension ring were clean. A simple cool down test was performed and the equilibrium temperature was found to be 79.7K This is 1.1K colder than the closest comparable test (Test 06) which would suggest a saving of 11mW assuming a 0.1K/mW sensitivity.

6.1.9 Test 09 — 19 Nov 93

The first titanium alloy cone was available for this test. This cone had been manufactured by spinning which had resulted in the top of the cone not being completely flat which raised concerns about the thermal contact resistance between the cone and the tube. In order to ensure that the resistance was low the joint between the tube and the cone was formed with soft aluminium spacers and indium gaskets between the two components (The flight model cone will be manufactured by super-plastic forming so the top will be flat so the spacers and gaskets should not be necessary in the future).

The temperature controller heater cable was also available for this test so a dummy common carrier was manufactured and assembled into the cooler. The dummy common carrier was a copper block of the same dimensions as the common carrier with a copper rod the same size as the finished flexible link machined onto it. This enabled it to be attached to the top of the cold finger without the need for the FPA tripod (which was not yet assembled). The temperature controller heater cable was glued to the back of the dummy common carrier. The integral heater in the cable being used for the test was not working so a resistor was glued to the opposite side of the dummy common carrier. The miniature thermistors to be used in the flight model had not been delivered so a flat film PRT was glued onto the common carrier adjacent to the resistor.

The assembled cooler was installed in the test facility and cooled to its equilibrium temperature. The patch reached a temperature of 84.5K at equilibrium. The cone temperatures remained high because the environment panels were still not cooled and the new cone had a very poor surface finish which resulted in a high emissivity.

6.1.10 Test 10 — 25 Nov 93

The heat straps which are required to cool the environment panels in the test facility were installed for Test 10. The cooler configuration was identical to Test 09.

The cooler patch reached an equilibrium temperature of 69.8K with an instrument temperature of 157.4K and an environment temperature of 164.9K. The base of the cone reached 140.8K.

6.1.11 Test 11

Test 11 was performed by Dr. T. Vellacott to verify the performance of the cooler temperature controller and decontamination heater. The real common carrier and FPA tripod were installed. It was found that as predicted, 18W of heater power would raise the patch to the specified temperature (240K).

6.1.12 Test 12 — March 1994

The cooler configuration for this test was changed significantly from the earlier ones — The tube is now manufactured from aluminium alloy. This was a mechanical decision following a similar change in the instrument. The super-plastic formed titanium alloy cone was used, and the titanium alloy patch suspension wires have been replaced by 7×0.1mm stainless steel wires because of problems with the mechanical performance of the cooler (see Appendix C). The inner and outer surfaces of the cone was covered in aluminised mylar to reduce its emissivity. With the instrument simulator and environment thermostated to 170K the patch reached an equilibrium temperature of 76.2K.

The sensitivity of the patch temperature to the instrument temperature was measured by reducing the instrument simulator temperature to 157.0K. This resulted in a patch temperature of 74.2K which gives a sensitivity of the patch temperature to instrument temperature of 0.15K/K. With a 50mW heat load into the FPA and an instrument temperature of 170K the patch reached a temperature of 80.7K giving a sensitivity of the patch temperature to FPA heat load of 0.09K/mW.

6.2 Results Analysis

In order to determine the extent to which the experiments on the DM cooler were agreeing with the model predictions, the simple analytical model (SAM) and the full numerical model (FNM) of the CIRS cooler were modified to represent the cooler under test. The following sections summarise the models used, the results obtained and the modifications required to improve the model after comparison with the test results.

6.2.1 Test 01 and Test 02

For Tests 01 and 02 the cold finger to patch connection was removed from the model. (This has the effect of removing the FPA and cold finger from the model). The cone material was changed to aluminium alloy rather than titanium alloy, and the radiation model was re-calculated using SSPTA with the patch back emissivity increased to 0.05 (bare metal) because there was no MLI blanket present. Because the annular radiator was not present for the first two tests, its outer surface emissivity was set to 0.05 to represent radiation from the suspension ring which was not painted.

Table 6.2 shows the comparison between the temperatures of the main components in the model and the experimental results. It can be seen from the table that the error in the calculated patch temperature is 8.7K, which is equivalent to some 87mW. In addition the cone temperature in the experiment is lower than that predicted by the model. The increased heat load into the patch is likely to be due either to the patch radiator emissivity being lower than predicted, or the patch back emissivity being higher than the value of 0.05 assumed. It is quite possible that the emissivity could be increased because of contamination on the surfaces caused by the patch radiator outgassing.

The discrepancy in the cone temperatures suggests that the cone is being cooled more than the model predicted, which would indicate that the cone-space coupling is larger than predicted, possibly because of radiation from the cavity formed between the patch and the suspension ring.

Table 6.2: Comparison between equilibrium model predictions and experiment results for Test 01

Component	Model	Experiment
Instrument Simulator	271.5K	271.5K
Environment Panels	274.9K	274.9K
Space Simulator	20.0K	18.0K
Cone Top	258.2K	241.2K
Cone Base	257.1K	236.4K
Patch	115.2K	123.9K

Table 6.3: Comparison between equilibrium model predictions and experiment results for Test 02

Component	Model	Experiment
Instrument Simulator	157.8K	157.8K
Environment Panels	258.7K	258.7K
Space Simulator	15.0K	14.3K
Cone Top	178.6K	187.4K
Cone Base	179.0K	186.1K
Patch	83.1K	92.9K

The results for Test 02 show that the error in the predicted patch temperature has increased to 9.8K. In this case the predicted cone temperatures were lower than the temperatures achieved in the test.

From the two sets of tests and model results we can compare the sensitivity of the patch temperature to the cone top temperature ($\frac{\delta T_p}{\delta T_c}$). A value of 0.576K/K was obtained in the experiment compared to a value of 0.403K/K from the full numerical model. A feeling for the meaning of the sensitivity to cone temperature is obtained from a very simple model:

Assume the patch is a simple disk, one side of which views space at a temperature of absolute zero with an emissivity of ϵ_p and view factor of unity. The other side views a flat plate (the cone) at a temperature of T_c with an emissivity of ϵ_{eff} with unity view factor. There is no conductive coupling between the cone and the patch. At equilibrium the power radiated to space is balanced by the heat load from the cone:

$$\epsilon_p A\sigma T_p^4 = \epsilon_{eff} A\sigma(T_c^4 - T_p^4)$$

This gives

$$T_p = \left(\frac{\epsilon_{eff}}{\epsilon_p + \epsilon_{eff}}\right)^{0.25} T_c$$

so the sensitivity is given by:

$$\frac{dT_p}{dT_c} = \left(\frac{\epsilon_{eff}}{\epsilon_p + \epsilon_{eff}}\right)^{0.25}$$

Using the SAM values: $\epsilon_p = 0.92$ and $\epsilon_{eff} = 0.026$ (assuming the cone and patch have emissivities of 0.05) then the calculated sensitivity is 0.407 which shows good agreement with the numerical model. This simple model neglects the effect of the patch suspension (which has the result of making the sensitivity non-linear). The fact that the sensitivity is higher than predicted suggests that either the patch back emissivity is larger than predicted, or the patch radiator emissivity is lower (or a combination of the two). If we assume that the patch radiator emissivity = 0.92 we can use the measured sensitivity of 0.576K/K to calculate the value of ϵ_{eff} to be 0.11, which is considerably higher than the 0.026 value calculated using the SAM which would point to either a contamination problem or the patch paint emissivity being considerably lower than expected.

6.2.2 Tests 03 to 04b

Tests 03 to 04b have been grouped together because the cooler configuration is very similar for all of them — The only difference between them is the addition of the cold finger which is only expected to add a maximum of 3.5mW heat leak into the cold stage, or approximately 0.4K temperature difference. In order to compare the performance of the cooler to the experiments the full numerical model (FNM) was modified to represent the cooler configuration in Test 04b, that is MLI on the patch back with the cold finger. The model was run for various instrument temperatures, keeping the environment temperature constant at 270K. The simple numerical model (SAM) of the cooler was modified in a similar manner, but no account was taken of the change in the material thermal conductivities at the raised environment temperatures in the experiment. The results obtained are plotted in Figures 6-3, 6-5, and 6-4. The full numerical model is plotted as a solid line with the simple analytical model drawn dashed. The experimental results are plotted as individual points on the figures.

The results show that the SAM shows far better agreement with the results then the more detailed FNM. In particular Figure 6-4 shows very good agreement between the SAM and the experiment for the variation of the patch temperature with the cone temperature. In fact the sensitivity of patch temperature to cone temperature predicted by the SAM was slightly higher than the experiment (0.376 compared to 0.361). Figure 6-5 shows that at high instrument temperatures the cone cools significantly more than predicted by either of the models. This suggests that the cone is more strongly radiatively coupled to the space simulator than assumed in the model. The likely cause of this is that the gap between the suspension ring and the patch acts as a cavity which will have considerably higher emissivity than the plane surface assumed in the model.

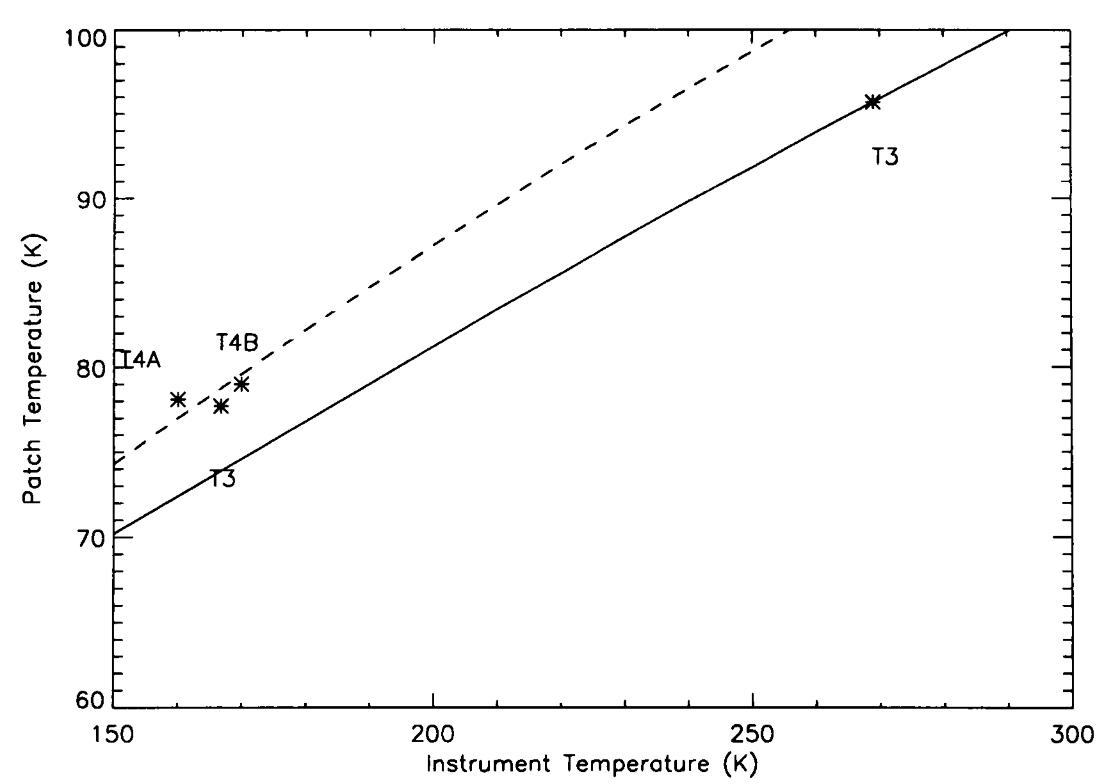

Figure 6-3: Comparison between the FNM, SAM and Tests 3 to 4b. The FNM is shown as a solid line, the SAM is shown dashed.

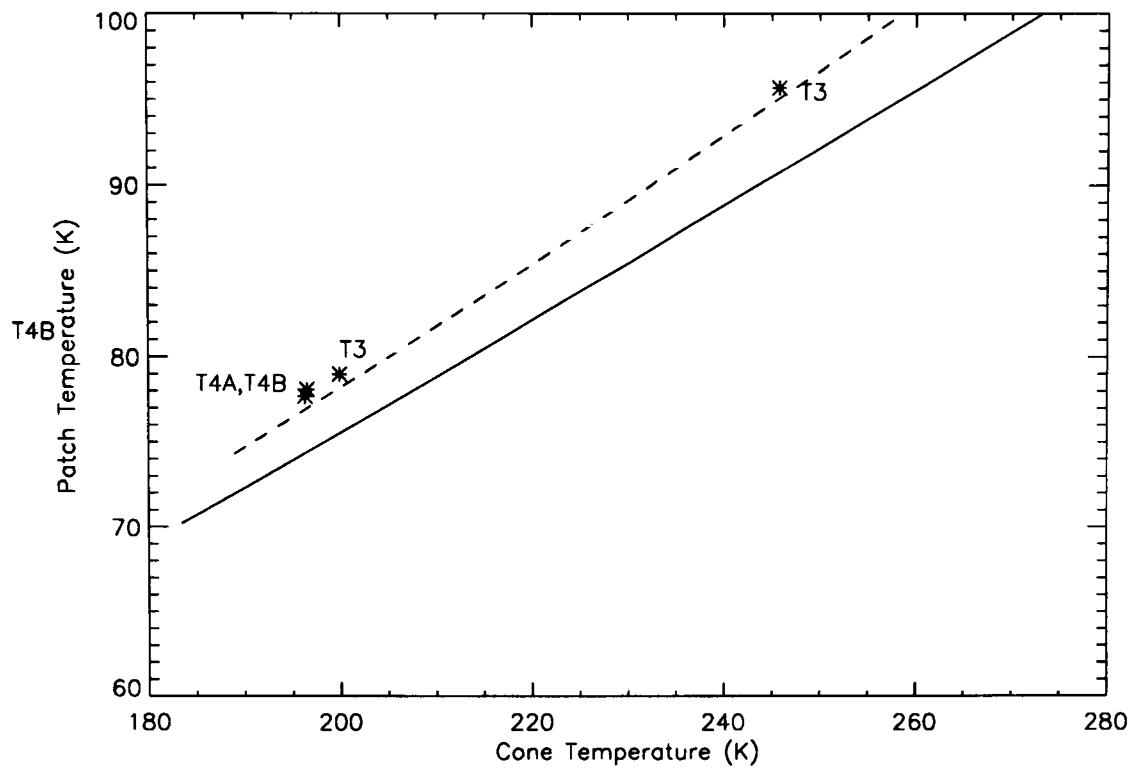

Figure 6-4: Comparison between the FNM, the SAM and Tests 3 to 4b. The FNM is shown as a solid line, the SAM is shown dashed.

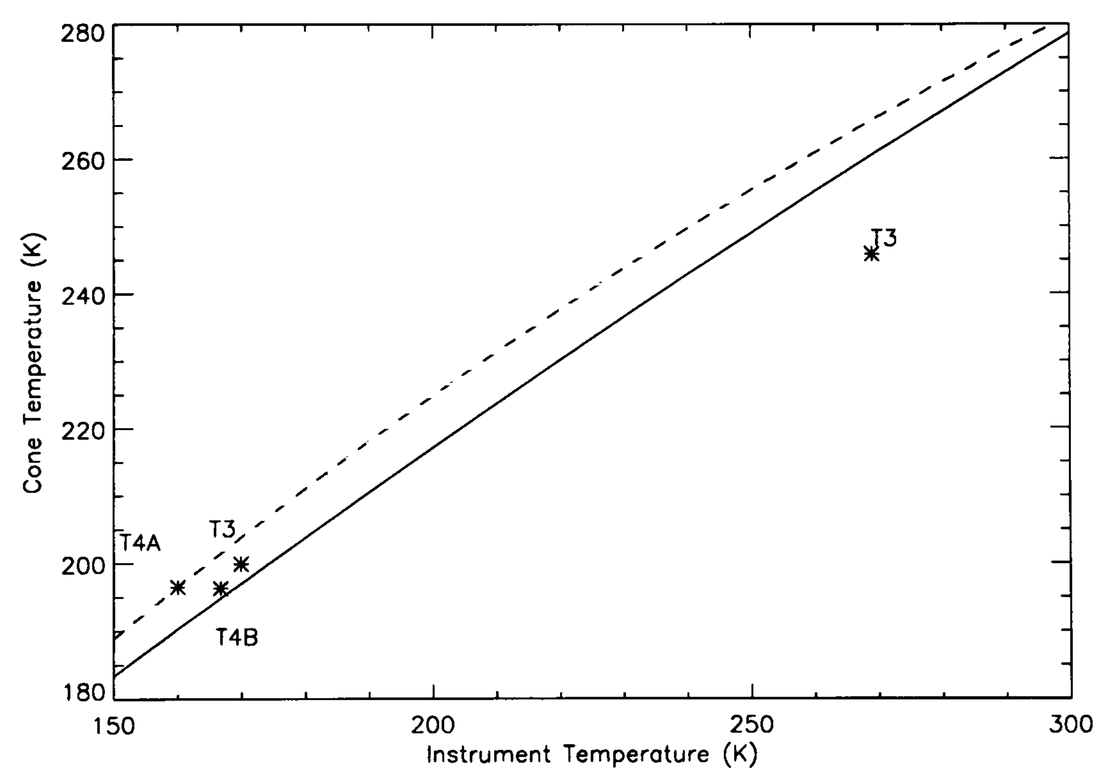

Figure 6-5: Comparison between the FNM, the SAM and Tests 3 to 4b. The FNM is shown as a solid line, the SAM is shown dashed.

It is interesting to note that the patch temperatures attained in Test 02 and Test 03 are very similar, whereas the boundary temperatures are very different. The reason the temperature has stayed approximately the same is that the heat leak into the patch must be about the same for the two tests. Because the only thing which has changed is the emissivity of the patch back (by adding the MLI), it is possible to estimate the emissivity of the MLI Blanket: The radiative heat load onto the patch back in Test 02 is:

$$q_{r2} = \epsilon_2 A_p \sigma (T_{c2}^4 - T_{p2}^4)$$

where ϵ_2 is the emissivity of the patch for Test 02, A_p is the area of the patch, T_{c2} is the cone temperature for Test 02, and T_{p2} is the patch temperature. Similarly for Test 03:

$$q_{r3} = \epsilon_3 A_p \sigma (T_{c3}^4 - T_{p3}^4)$$

where ϵ_3 is the emissivity of the patch for Test 03 (the MLI emissivity). If we assume that the patch temperature was equal for both tests, then $T_{p2} = T_{p3}$ and $q_{r2} = q_{r3}$. Re-arranging the above expressions gives:

$$\epsilon_3 = \epsilon_2 \frac{T_{c2}^4 - T_p}{T_{c3}^4 - T_p}$$

or $\epsilon_3 = 0.323\epsilon_2$. Now ϵ_3 is the emissivity of the MLI blanket and ϵ_2 is the emissivity of the patch back without the MLI. Estimates of the emissivity of the patch back lie in the range 0.03-0.05 which give MLI emissivities in the range 0.010–0.016. This suggests that the MLI blanket is not reaching its design specification of an emissivity of 0.01.

6.2.3 Test 05a to Test 08

Tests 05a to 08 are grouped together because they used a very similar cooler configuration, with only minor variations such as the addition of spacers or aluminium tape etc. The basic configuration of the cooler was a titanium tube, aluminium cone, annular radiator, patch with MLI blanket and a cold finger. As in the previous section the FNM and SAM were modified to represent this cooler configuration and run for various instrument temperatures.

A surprising result from the experiments was that the addition of the annular radiator did not have the effect of reducing the equilibrium patch temperature although the cone temperature had been reduced by approximately 15–20K. The reason was found to be the way that the FNM had been modified to represent the cooler in Tests 01-04b. In order to represent the tests the emissivity of the annular radiator had simply been set to a low value (0.05) rather than modifying the radiation model itself. When the radiation model

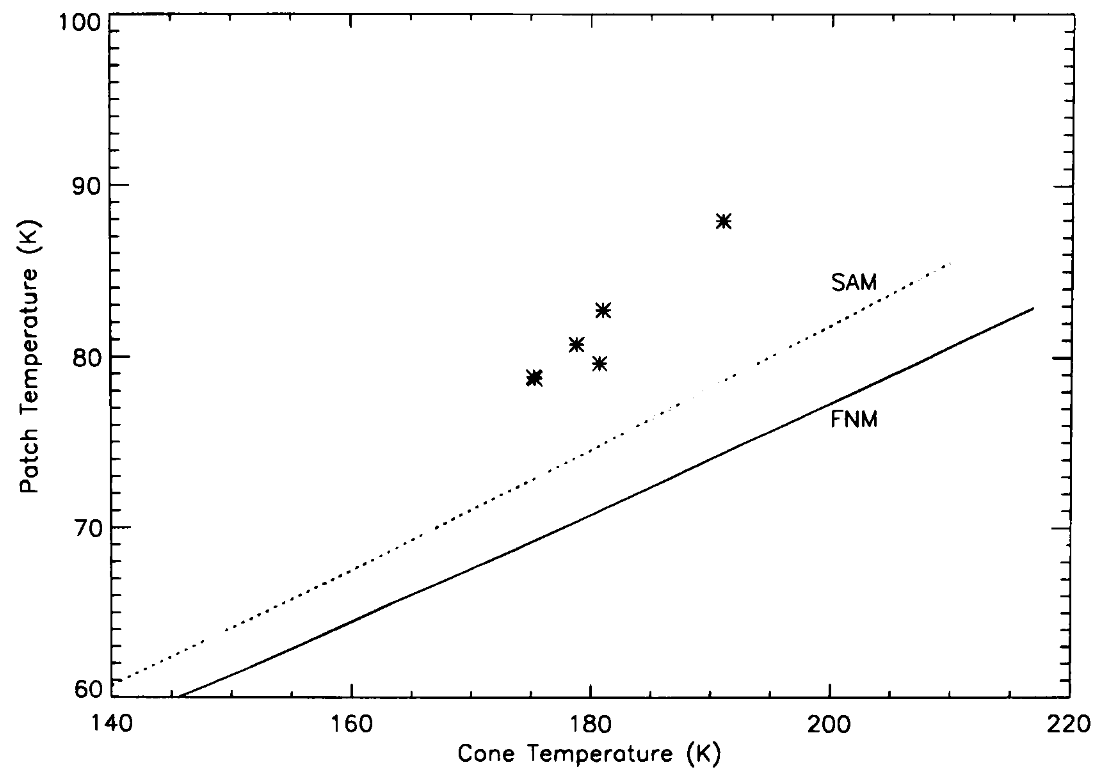

Figure 6-6: Comparison between the SAM, the FNM and the results Tests 05–08.

was altered by removing the annular radiator so that the cone, patch and suspension ring had a view to space the observed effect of the addition of the annular radiator not effecting the patch temperature was reproduced. This shows that the patch edge was being cooled by direct radiation to the space simulator, but this source of cooling was removed when the annular radiator was fitted. Figure 6-6 shows the comparison between the SAM, the FNM and the experiment.

The experiment and the model differ significantly, indicating that some parameters in the model are incorrect for the cooler which was tested. The three parameters which effect the patch temperature most significantly are the patch-cone effective emissivity (the combination of the patch MLI emissivity and the cone emissivity), the patch radiator emissivity and the patch suspension thermal resistance. In order to determine the values of these parameters, the simple analytical model (SAM) was modified slightly so that it would return the equilibrium patch temperature for a given cone temperature and set of input data. It also returned the derivative of patch temperature with respect to each of the parameters. The set of input data contained the patch radiator emissivity, the patch-cone effective emissivity and the suspension thermal resistance. The other parameters in the model were held constant at the usual SAM values. Because at high annular radiator temperatures there is a significant heat load on the patch from annular radiator radiation reflected from the space simulator, an estimate of this heat load was added into the SAM by assuming that the radiation was reflected with a uniform flux across the space simulator aperture. The data for the variation of patch temperature with cone temperature was taken from Tests 05 to 08b and a standard non-linear least squares fit routine was used to determine the values of the parameters [53]. The retrieved parameters are shown in Table 6.4.

Table 6.4: Parameters retrieved from the analysis of Tests 05 to 08b.

Parameter	**Retrieved Value**	**Std. Dev.**
Patch-cone Effective Emissivity	0.0197	0.0119
Patch Radiator Emissivity	0.843	0.340
Patch Suspension Resistance (K/W)	6862	5992
χ^2	9.48	
Q (Incomplete gamma function [53])	0.024	

The retrieved parameters shown in the table were obtained by assuming a standard deviation on the data points of 1K. The parameter Q is a measure of the goodness of fit. It is somewhat smaller than would be hoped — [53] states that a value in excess of 0.1 shows a believable fit with a value in excess of 0.001 possibly believable. The most likely reason for the goodness of fit parameter not being as large as would be hoped (assuming that the model is not vastly wrong) is that the calculation of the probability Q assumes that the errors are normally distributed. In this case the errors are unlikely to be normally distributed so the calculated Q will give a lower measure of the goodness of fit than would be expected.

The standard deviations given in the table are taken from the covariance matrix generated during the curve fit and are valid only on the assumption of Gaussian errors. They are included to give an indication of the likely magnitude of the errors in the fit rather than a definitive error estimate which would require detailed knowledge of the distribution of the errors in the measured temperatures and a Monte Carlo simulation of the data. The standard deviations shown indicate that the errors in the fit are very large because the solution was poorly constrained by the data points available. The particular solution obtained was sensitive to the starting values of the parameters which suggests that the χ^2 curve is not a simple minimum in parameter space but is quite flat with a number of localised minima. The covariance term between the error in the patch MLI emissivity and the patch radiator emissivity suggests that the errors are strongly correlated. This means that for all the error in the patch radiator emissivity is large, the error in the retrieved MLI emissivity will be in the same direction. Therefore the cooler performance predicted using the retrieved parameters shown in the table will be similar for other possible sets of retrieved parameters (since the cooler performance is largely governed by the ratio of the two emissivities.

It appears that neither the patch MLI nor the patch radiator are performing to specification (emissivities of 0.01 and 0.92 respectively). The most likely cause for the failure of the patch MLI to perform as measured in the flat plate calorimeter (see Chapter 4) is that it does not sit flat on the back of the patch as intended because it is forced up in the middle by the cold finger, causing the edges to lift in the spaces between the support studs. Shields may be touching where the cold finger forces them together, and the edge effect will be increased significantly because of the extra surface area of the edge of the blanket (which is effectively a black cavity).

The retrieved patch emissivity is lower than predicted, corresponding to a surface emissivity of approximately 0.55 compared to the 0.70 predicted. The surface finish on the patch paint was not good — The paint appeared grey in the visible and did not adhere well to the metal surface so a low value of the surface emissivity was anticipated. The paint was supplied by GSFC who reported problems with the batch used in the test. A second batch of paint has been supplied which gives a much better finish. It is hoped that more careful surface preparation of the flight model patch will result in a better surface finish and better adhesion to the surface.

The retrieved thermal resistance is larger than the calculated one (4778K/W), but the result is not significant because of the large error on the retrieved value. The large error is most likely to be caused because the temperature range of the measurements was not large enough to distinguish between the linear and fourth order terms in the model.

Figure 6-7 shows the SAM re-calculated using the retrieved parameters compared to both the results of the tests on the aluminium cone cooler which were used for the analysis (stars) and the tests on the titanium cone cooler (diamonds) which were not used for the analysis. The figure shows a reasonable agreement between the fitted curves and the experiment results.

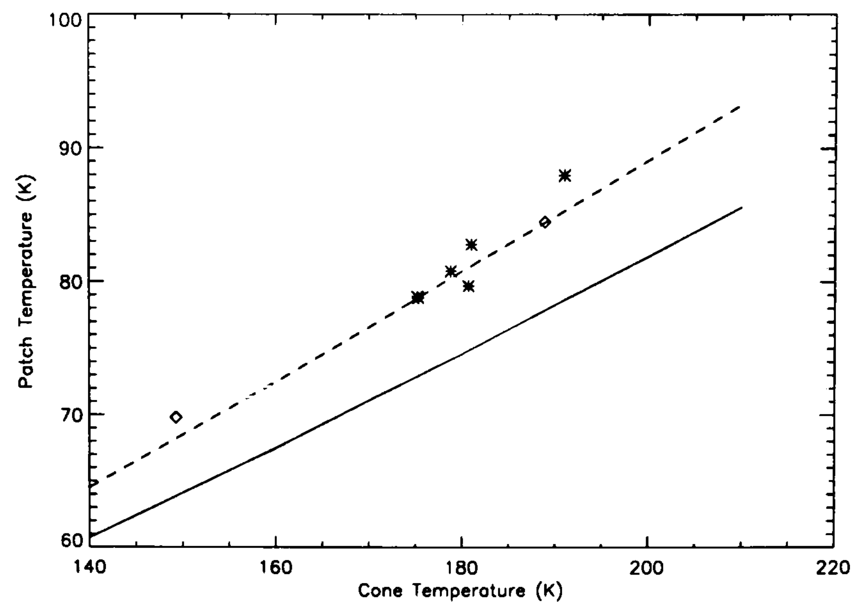

Figure 6-7: Comparison between the original SAM (solid line), the SAM modified using the retrieved parameters (dashed line), the tests using the aluminium cone (stars) and the tests using the titanium cone (diamonds). The tests using the titanium cone were not included in the analysis to determine the parameters in the modified SAM.

6.2.4 Tests 9 and 10

The full numerical model of the cooler was modified for Tests 9 and 10 by removing the tripod legs and detector cables from the model. The emissivity of the tripod top and common carrier was increased to 0.1 because of the components glued to the common carrier. The emissivity of the flexible link was reduced to 0.05 because it was a solid metal rod in the experiment rather than a flexible bundle of wires. The results of the experiments and the models are compared in Table 6.5

The error in the model prediction for Test 10 was 8.1K, corresponding to 73.6mW. The full numerical model for this test predicted a cooling power of 115.3mW at 80K for an instrument and environment temperature of 170K. The cooling power for the experiment can be calculated to be $115.3 - 73.6 = 41.7$mW at 80K. A further 36.4mW of cooling will be required for the FPA tripod and the detector cables, giving a cooling capacity of 5.3mW for the combined cooler and FPA assembly. For this particular cooler configuration we can deduce that it will cool to 80K with the FPA installed, but it will have only 5.3mW of excess cooling to compensate for environmental backloading (The design requirement is 50mW).

Table 6.5: Comparison between the FNM and the results of Tests 9 and 10.

Parameter	Test 09		Test10	
	Model	Expt.	Model	Expt.
Instrument Temperature (K)	168.7	168.7	157.4	157.4
Environment Temperature (K)	260.2	260.2	164.9	164.9
Cone Top Temperature (K)	189.9	201.4	154.5	157.7
Cone Base Temperature (K)	189.6	176.4	140.1	140.8
Patch Temperature(K)	76.5	84.5	61.7	69.8

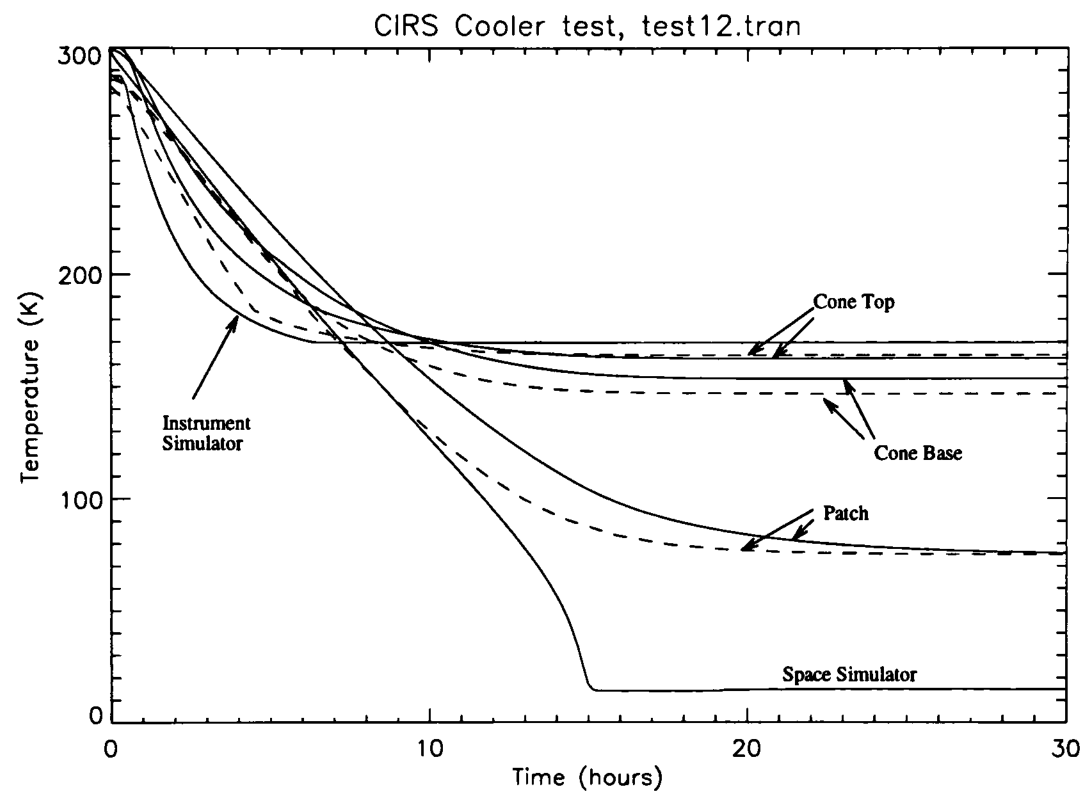

Figure 6-8: Comparison between the experimental results and the FNM for Test 12. The solid lines are the experimental results and the dashed lines the model predictions.

6.2.5 Test 12

For Test 12 the tube material was changed to aluminium alloy and its dimensions changed to represent the changes in the design of the tube. The patch suspension was modified in the model to represent the stainless steel wires used in the test. The common carrier emissivity was increased to 0.2 to account for the temperature controller heater not being covered. A steady state solution of the FNM was calculated for the boundary temperatures encountered in the test. The results are compared in Table 6.6. Figure 6-8 shows the cooldown curves obtained from the experiment and the model.

The model and the experiment show far better agreement for this configuration than for the earlier tests, with the error in the predicted patch temperature reducing to 1.1K, which corresponds to approximately 10.0mW. This suggests that the addition of the aluminised mylar radiation shield on the inside of the cone has brought the cone to patch coupling closer to the levels predicted in Chapter 3 by a combination of reducing the cone emissivity and reducing the effective temperature of the cone. The sensitivity of the patch temperature to FPA heat load shows good agreement with the model predictions (0.09K/mW). The sensitivity of the patch temperature to the instrument temperature was lower than predicted. This could suggest that there was a significant thermal contact resistance between the cone and tube which will reduce the sensitivity of the cone to changes in the instrument temperature.

The cool down curves show that the patch and cone cool more slowly than predicted, suggesting that the heat capacities in the model are too small. The most likely cause for the discrepancy is that the model assumes that the cooler is formed from simple geometric shapes when calculating the volume of the components, so the masses of bolts, ferrules etc. are neglected. The mass of the patch is expected to be low in the model because both the mass of the honeycomb, and the mass of the paint are neglected.

For this cooler configuration, the FNM predicted the cooling power at 80K to be 37.5mW. If we correct this figure for the error in the model, we would expect the real cooling power to be $37.5 - 10.0 = 27.5$mW at 80K, accounting for the error in the model.

In order to determine the cooling power of the original design of cooler (with titanium alloy wire suspension) it is necessary to correct the figure for the cooling power. The following corrections are applied:

1. Patch Suspension: The suspension system in the test used thicker wires than originally specified, and the material was stainless steel rather than titanium alloy, which as a higher thermal conductivity. The heat leak through the patch suspension was approximately 22.9mW larger than the design value.

2. Space Simulator Emissivity: The FNM assumed that the space simulator had an emissivity of unity, whereas the calculated value is 0.99. This will result in a reduction in the radiated power of approximately 1.7mW.

3. Annular Radiator radiation reflected from the space simulator target: The FNM used did not include the backload from radiation reflected from the space simulator. It is estimated that an additional 3.5mW is absorbed by the patch from reflected

Table 6.6: Comparison between the FNM and the results of Test 12.

Parameter	Test 12	
	Model	Expt.
Instrument Temperature (K)	169.9	169.9
Environment Temperature (K)	170.5	170.5
Cone Top Temperature (K)	164.0	162.6
Cone Base Temperature (K)	146.9	153.4
Patch Temperature(K)	74.5	75.6

annular radiator emissions.

These corrections are added to the 27.5mW cooling power to give a predicted cooling power for a cooler with the titanium alloy suspension wires of 55.6mW. This figure just meets the cooler design requirement of 50mW excess cooling at 80K.

Chapter 7

Conclusions and Further Work

7.1 Cooler Thermal Design

The thermal models of the cooler and FPA showed good agreement over the temperature ranges for which they were configured. The differences between the various models can all be accounted for by considering the change in the technique of calculating the heat loads between the models. The results of the numerical models can be bracketed by the SAM by changing the assumptions made in calculating the heat loads so we can be confident that all the models are representing the same configuration, but with different assumptions made.

The heat balance of the cooler shows that the total cooling capacity at 80K is approximately 186mW. The main components which make up the balance at equilibrium are discussed below:

- Tripod Legs (30mW): The dimensions of the legs were taken as those used successfully on the ISAMS instrument [10] so there is no room for improving upon this heat leak without abandoning the ISAMS design which is known to have flown successfully. A great deal of effort was made by the ISAMS team to minimise the heat leak through the legs so it is unlikely that any improvement could be made without risking the structural integrity of the FPA if the material is to be kept as titanium alloy. The main way in which the thermal performance could be improved would be to change the material to a composite such as glass reinforced epoxy (e.g. G10). This route was investigated as part of the ISAMS project but problems were encountered with the structure failing at the joints which is why titanium alloy was used in that case.

- Patch MLI (20mW): The patch MLI is a critical component because of the problem of predicting its emissivity [32, 33, 34, 35]. A calorimeter was built specifically to measure the emissivity of the MLI blanket and it appeared to work well in the apparatus. The apparatus was not large enough to test the whole CIRS blanket so it was necessary to extrapolate the results to the full size blanket. The performance of the blanket was largely dominated by the edge effect and the retaining studs so it would be unlikely that the performance could be improved much further by adding more shields and spacers. The main area in which the blanket could be improved would be in reducing the heat leak into the edge of the blanket (See Section 7.3.1).

- Patch Edge (15mW): The radiative load on the patch edge contributes approximately 15mW to the heat balance. The only way of reducing this heat load would be to add an MLI blanket around the edge of the patch in order to reduce its emissivity. This possibility is currently being investigated by other members of the project.

- FPA Radiation (10mW): The radiative load onto the FPA is a simple function of its surface area and emissivity. The heat load was calculated assuming it was gold plated so the only way to reduce the heat load would be to reduce its size. The FPA design is only 16mm$\times$16mm so it would be very difficult to reduce its size further if the common carrier and sub carrier arrangement were to be retained. The common carrier and sub carrier arrangement is necessary because the two sets of detector arrays are being manufactured in different places and integrated at Oxford.

- Electrical Cables (14mW): The electrical cables have been optimised to give the minimum heat leak for the required maximum electrical resistance. Reducing the heat leak further would require some sort of floating intermediate radiation shield between the cable and the tube which would increase the complexity of the FPA and introduce an extra hazard if it were to come loose during vibration.

7.2 Cooler Performance

The cooler tests described in Chapter 6 showed that the cooler failed to reach the temperatures predicted by the models. It is suspected that the cause of the discrepancy is the patch MLI not performing as well as expected, but the attempt to measure the emissivities of the patch radiator and MLI resulted in large errors in the measurement because of the lack of data points available, and the solution being ill constrained.

The final test described in this thesis (Test 12) produced the closest agreement with the models with the model predicting a temperature 1.1K lower than that achieved in the test. The analysis of the results of the test predicts the cooling power of the finished cooler to be approximately 55mW at 80K if the design remains unchanged. This just meets the specification of 50mW cooling power at 80K. There is a desire to have the cooler reach a minimum temperature of 70K. This would require approximately 100mW cooling power at 80K which will require more work.

Because of time constraints the only test on the complete cooler (Test 12) was a simple cool down to minimum temperature. Now that the complete cooler is available it would be useful to characterise the system by measuring the equilibrium patch temperature at various instrument temperatures and heater powers. This would enable the data analysis described in Section 6.2.3 to be repeated with increased accuracy to determine the radiator and MLI emissivities.

A number of problems in the cooler design were identified during the tests:

1. Patch Finish: The paint used in the DM cooler patch did not adhere well to the surface which will have reduced its performance (Section 6.2.3). The edge of the patch had a glue fillet around its circumference where the front and back skins were bonded together rather than being a clean, gold surface as assumed in the models.

2. MLI: Problems were encountered with the MLI blanket not sitting flat on the back of the patch but lifting in the gaps between the retaining posts. Changing the shield material from aluminium foil to a formable material such as mylar would allow the shields to be shaped to fit around the cold finger and reduce the tendency for the shields to lift away from the patch at the edges.

3. Flexible Link: The flexible link used was a bare bundle of wires which has a large

emissivity. The addition of a flexible sleeve formed from a material such as aluminised kapton would considerably reduce the radiative heat load.

7.3 Further Work

This section describes some recommendations for the improvement of the cooler design.

7.3.1 MLI Improvements

Results of the thermal tests on the DM cooler suggest that the MLI blanket on the back of the patch is not meeting its emissivity specification ($\epsilon = 0.01$), so this is clearly the area of the thermal design which requires most work. The blanket differs from that tested in the lab in that it does not lie flat on the back of the patch, whereas the blanket was perfectly flat in the calorimeter. The cause of the problem is the cold finger forcing the centre of the blanket away from the patch back. This results in the shields being forced together at the centre, probably resulting in them touching, and being forced apart at the edge of the patch between the retaining posts, resulting in an increased heat load into the edge of the blanket.

In order to allow the blanket to lie flat either the holes in the centres of the shields would have to be made bigger so that the shields could lie closer to the patch back, or the shields would have to be shaped to fit around the cold finger base. The first option would have the disadvantage of uncovering more of the cold finger base, and hence increasing the radiative heat load onto it, so some work would be required to determine whether or not the overall effect is beneficial. The second option would require changing the shield material from aluminium to a formable material such as aluminised mylar. Because the emissivity of aluminised mylar shields is higher than that of aluminium, the number of shields would have to be increased, and a suitable manufacturing process developed.

7.3.2 Cone Improvements

The heat load into the back of the patch could be reduced by introducing a radiation shield between the patch and the cone small end. Mounting the shield off the large end of the cone would tie its temperature close to that of the annular radiator so the effective temperature to which the patch is exposed would be reduced. The main problems with this proposal are mechanical: It will be necessary to make the shield rigid enough to meet the requirements for the resonant frequency of the structure while keeping within the mass budget. It is possible that the reduction in the cooler mass which resulted from changing the cone manufacturing process to super-plastic forming could be used to add the radiation shield.

7.3.3 Flexible Link

The flexible link in the current cooler design is a simple bundle of copper wires which has a very high emissivity. The addition of a close fitting radiation shield such as a layer of aluminised mylar would reduce the heat load significantly. The addition of such a shield would make the assembly of the cooler and FPA more difficult because it would need to be fitted after the cold finger to flexible link joint had been made so would run the risk of damaging the FPA.

7.4 Summary

The thermal models of the CIRS cooler which were described in Chapter 3 show good agreement between them in their predictions of the cooler performance. The cooler test facility proved to be satisfactory for simulating the expected operating environment of the cooler. Test results on the DM CIRS cooler showed that it did not achieve the minimum temperatures predicted by the thermal models although it is likely to meet its design specification of 50mW cooling capacity at 80K. A number of design improvements have been suggested and are being implemented to increase the cooling capacity of the flight model cooler.

Appendix A

Conductive Shape Factors

The Fourier heat conduction equation,

$$q/A = -k\frac{dT}{dx} \tag{A.1}$$

defines the heat flow per unit cross sectional area through a material when the temperature gradient parallel to the heat flow is $\frac{dT}{dx}$ and k is the thermal conductivity of the material.

For geometries where the area perpendicular to the heat flow is not constant such as radial heat flow in a disk or cone, the above expression is modified with A/l being replaced by an equivalent value S, where S is known as the conductive shape factor for the given geometry. The conductive shape factor can be found for a given geometry by dividing the path between the points into thin slices over which the area is assumed constant, and integrating over the path.

e.g. Radial Conduction in a Cylindrical Segment

Consider the cylindrical segment shown in Figure A-1. The heat flow we require is the flow between radius r_1 and r_2.

At a radius r, the area perpendicular to the heat flow (A) is given by:

$$A = \alpha r t$$

Where α is the segment angle and t is the thickness of the cylinder.

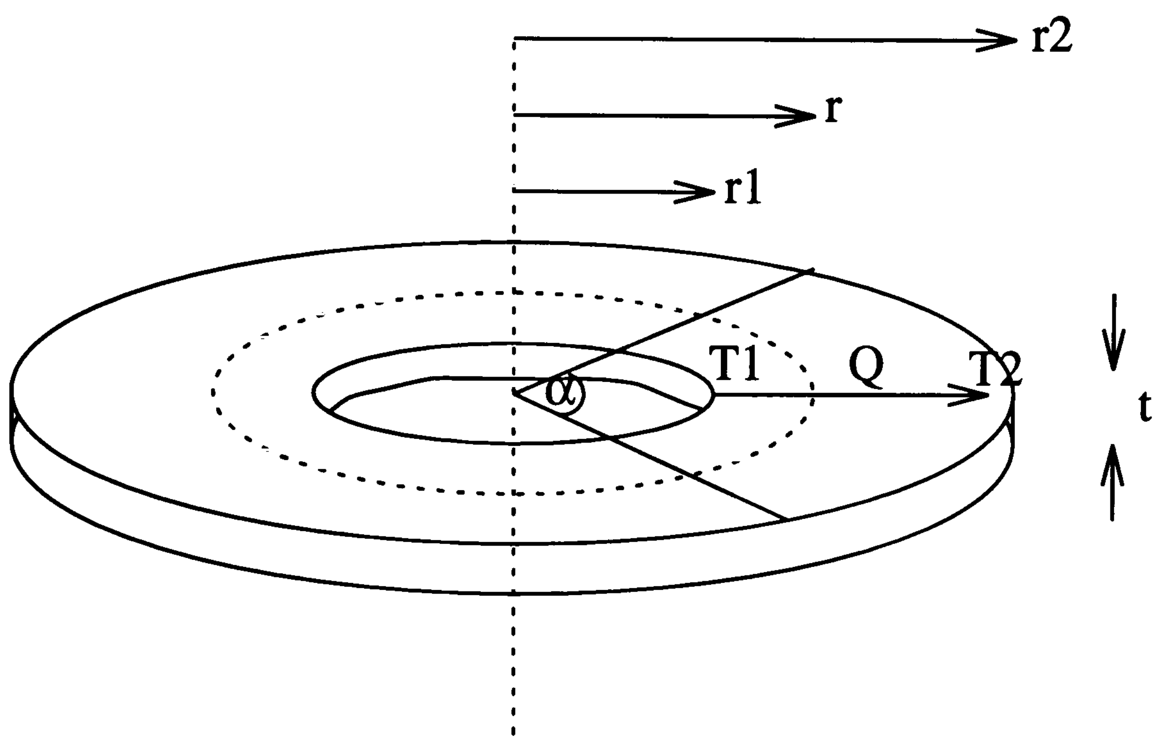

Figure A-1: Radial Conduction in a Cylindrical Segment

Assume that the area A is constant over a distance dr, and that the temperature difference between r and $r + dr$ is dT. Therefore the heat flow across the element dr is:

$$Q = k\frac{A}{l}dT = k\frac{\alpha r t}{dr}dT$$

Rearrange and integrate between r_1 and r_2:

$$\int_{r_1}^{r_2} \frac{dr}{r} = -\frac{k\alpha t}{Q}\int_{T_1}^{T_2} dT$$

which gives:

$$Q = k\frac{\alpha t}{\log r_2/r_1}(T_1 - T_2)$$

so the conductive shape factor for radial conduction in a cylindrical segment of angle α, thickness t, between radii r_1 and r_2 is:

$$\frac{\alpha t}{\log(r_2/r_1)}$$

This corresponds to published expressions for radial conduction in a thin disk [51]. The above process has been repeated for a number of other geometries in cylinders, conical shells etc. for use in the numerical models of the cooler. The results are summarised in the following table.

Geometry	**Direction**	**Shape Factor**
Cylindrical Segment	Radial	$\frac{\alpha t}{\log(r_2/r_1)}$
Cylindrical Segment	Tangential	$\frac{t\log(r_2/r_1)}{\alpha}$
Cylindrical Segment	Vertical	$\frac{\alpha(r_2^2-r_1^2)}{2l}$
From Circle to Segment	Radial	Approx $\frac{2}{\alpha t}$
Conical Shell Segment	Radial	$\frac{\alpha t\sin(\beta)}{\log\left(\frac{2r_2t+t^2\cos(\beta)}{2r_1t+t^2\cos(\beta)}\right)}$
Conical Shell Segment	Tangential	$\frac{t\log(r_2/r_1)}{\alpha\sin(\beta)}$

Where r_1 and r_2 are the inner and outer radii of the segment respectively, α is the segment angle in radians, β is the cone half angle in radians. t is the thickness of the shell, where appropriate. The expressions in the table are used in the numerical models of the cooler to determine the conductances between the various nodes in the model.

Appendix B

Radiation Heat Transfer

This Appendix details the mathematical relationships used in calculating radiation heat transfer in this thesis.

B.1 Basic Principles

The simplest case of radiation heat transfer is that of a body surrounded by a perfectly black enclosure as shown in Figure B-1. In this case the net heat flow between the body and the enclosure is:

$$q_{1--2} = \epsilon_1 A_1 \sigma (T_1^4 - T_2^4) \tag{B.1}$$

where ϵ_1 is the emissivity of the body, A_1 its surface area and T_1 its absolute temperature. T_2 is the temperature of the enclosure. σ is the Stefan-Boltzmann constant which has the value $5.669 \times 10^{-8} \mathrm{Wm}^{-2}\mathrm{K}^{-4}$. Throughout this thesis the grey body approximation has been used — i.e. it is assumed that the total emissivity ϵ_1 does not vary with wavelength.

The situation becomes more complicated if the enclosure is not perfectly black but

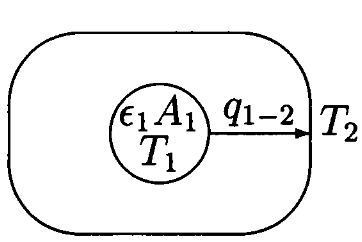

Figure B-1: Body surrounded by a perfectly black cavity

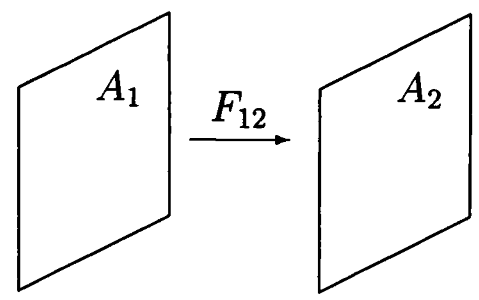

Figure B-2: The viewfactor F_{12} is the fraction of the radiation leaving surface 1 which is incident on surface 2.

reflects some of the incident radiation. In this case the *View Factor* between the two bodies must be considered so that multiple reflections may be taken into account.

B.2 View Factors

B.2.1 Properties of View Factors

Consider two black surfaces 1 and 2 as shown in Figure B-2. The view factor F_{12} is defined as being the fraction of the radiation leaving surface 1 which is incident on surface 2. The view factor is therefore purely a function of geometry — The material properties have no effect on the view factors.

If both surfaces are black, the net heat flow from surface 1 to surface 2 is:

$$q_{12} = A_1 F_{12} \sigma (T_1^4 - T_2^4) \tag{B.2}$$

where T_1 and T_2 are the absolute temperatures of surface 1 and surface 2 respectively. Writing Equation B.2 from the point of view of surface 2:

$$q_{21} = A_2 F_{21} \sigma (T_2^4 - T_1^4) \tag{B.3}$$

But $q_{21} = -q_{12}$ which gives:

$$A_1 F_{12} = A_2 F_{21} \tag{B.4}$$

Equation B.4 is useful when manipulating view factors because it relates the view factor between surface 1 and surface 2 to the view factor between surface 2 and surface 1.

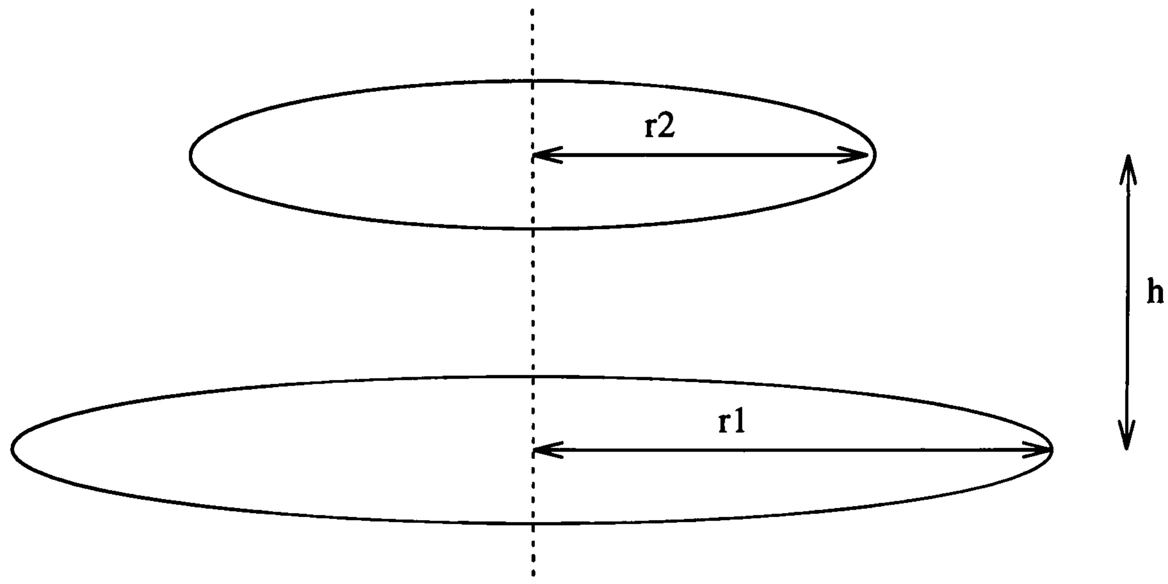

Figure B-3: View factor between two concentric disks

The view factors must be calculated for the specific geometry under consideration. The technique used is to consider small areas of the surfaces dA_1 and dA_2. A straight line drawn between dA_1 and dA_2 intersects the areas at angles ϕ_1 and phi_2 to the normals and the length of the line is r. The view factor may be evaluated for the specific geometry by evaluating the following expression taken from [24]:

$$A_1 F_{12} = \int_{A2} \int_{A1} \cos\phi_1 \cos\phi_2 \frac{dA_1 dA_2}{\pi r^2} \tag{B.5}$$

Equation B.5 is rarely used analytically because for simple geometries the results are available in reference tables [41, 43, 24], or for more complex geometries computer codes such as VIEW [38] or SSPTA [37] are used to determine the view factors.

B.2.2 View Factor Manipulation

Given an expression for the view factor for a simple geometry, Equation B.4 can be used to determine the view factors for other geometries. For example consider the view factors between the end of a cylindrical shell and the surface of the shell.

The starting point is the expression for the view factor between two concentric disks taken from [41] as shown in Figure B-3. The view factor between the disks is given by:

$$F_{12} = 0.5 \left[x - \sqrt{x^2 - 4\frac{R_2}{R_1}^2} \right] \tag{B.6}$$

where

$$x = 1 + \frac{1 + R_2^2}{R_1^2} \qquad R_1 = \frac{r_1}{h} \qquad R_2 = \frac{r_2}{h} \tag{B.7}$$

If we wish to determine the view factor between the base of a cylindrical shell and the inside of the shell first calculate the view factor between the base and the top disk (F_{bt}) using Equation B.6. Since all the radiation emitted from the base must either be incident on the top disk or the inside of the shell, the view factor between the base and the shell $F_{bs} = 1 - F_{bt}$. This method is easily extended to calculate the view factor between an annulus and a cylinder, a cylinder to itself, cylinder to cylinder etc. [43, 24, 41, 11]. Some of the combinations require the use of Equation B.4 to change the direction from which viewfactors are calculated to simplify the analysis. This technique was used in the calculation of the space simulator emissivity as described in Chapter 5.

When the surfaces involved in the heat transfer are grey as opposed to black, the situation is complicated by the need to consider multiple reflections. A number of mathematical methods for calculating the total heat transfer between surfaces in these situations, for example [43, 24, 44].

B.3 Approximations

B.3.1 Small Components

The Simple Analytical Model (SAM) and parts of the Full Numerical Model (FNM) described in Chapter 3 used an assumption that if a small object is completely surrounded by a significantly larger object then the emissivity of the larger object may be neglected and the larger object treated as a black cavity.

This approximation is based on the expression for the net radiative exchange between a convex object completely enclosed by a concave surface given in [24]:

$$q_{12} = \frac{1}{\left(\frac{1}{\epsilon_1} + \frac{A_1}{A_2}\left(\frac{1}{\epsilon_2} - 1\right)\right)} A_1 \sigma (T_1^4 - T_2^4) \tag{B.8}$$

where the subscript '1' refers to the inner surface and the subscript '2' to the outer. If the outer surface is a lot larger than the inner (i.e. $A_2 >> A_1$) then equation B.8 simplifies to Equation B.9:

$$q_{12} = \epsilon_1 A_1 \sigma (T_1^4 - T_2^4) \tag{B.9}$$

This is the expression used in the SAM for the heat load onto small components such as the FPA and the tripod legs. This expression will always over-estimate the heat loads rather than under-estimate them so will tend to give a conservative estimate of the cooler performance.

B.3.2 Effective Temperature

For the case of components which are not isothermal (such as the tripod legs) we define a single temperature which will give a similar net radiative heat load to the true, continually varying temperature distribution along the component. In order to calculate this *effective temperature* (T_{eff}) we take an area weighted average of T^4 along the component:

Consider a cylinder of length l. Assume it has a linear temperature gradient imposed upon it between boundary temperatures T_1 and T_2 at the ends. At a distance x from end 1, the temperature $T(x)$ is given by:

$$T(x) = T_1 + \frac{(T_2 - T_1)x}{l} \tag{B.10}$$

Since we are assuming the component is a cylinder, its circumference does not change along its length so we can simply integrate Equation B.10 along the length of the cylinder to obtain the effective temperature as shown in Equation B.11.

$$T_{eff}^4 = \frac{\int_0^l \left(T_1 + \frac{(T_2 - T_1)x}{l}\right)^4 dx}{\int_0^l dx} \tag{B.11}$$

Evaluating the above expression gives:

$$T_{eff}^4 = \frac{T_2^5 - T_1^5}{5(T_2 - T_1)} \tag{B.12}$$

which is the expression used for the effective temperature of the tripod legs and ribbon cables in the SAM as discussed in Chapter 3. It must be noted that the above analysis assumed that the temperature gradient was linear. This will only be the case if the radiative component of the heat flow through a component is small compared to the conductive component. The expression is therefore valid for the tripod legs (30.8mW conduction, 0.2mW radiation), but gives a large over-estimation of the heat leak through the detector cables which are radiation dominated rather then conduction dominated (See Section 3.3).

A similar procedure may be followed to determine the effective temperature of a conical frustum, again assuming a linear radial temperature gradient to derive the expression quoted in Chapter 3.

Appendix C

Mechanical Performance

This appendix summarises the changes in the mechanical design of the patch suspension system since the Author left the project.

The cooler used in the tests described above was subjected to a series of vibration tests by Dr. T Vellacott. During these tests it was found that the titanium wire patch suspension system failed when subjected to the vibrations specified for accepting the cooler for flight. The problem appeared to be caused by a poor surface finish on the wires resulting in stress concentrations.

In order to reduce this problem the design was changed to use stranded stainless steel wires because the stainless steel had a far smoother surface finish. The effect of the strands would be to prolong the life of the whole cable under vibration. The vibration test requirement for instruments on Cassini was later increased to a level where a free wire suspension system would be unsuitable.

The cooler cover has now been modified to act as a clamp during launch in order to prevent the patch suspension from moving. Half of the suspension wires have been replaced by a combination of wires and springs to enable the patch to be pushed back onto stops on the cone. When the cover is deployed the springs pull the patch off the stops into the position intended in the original design. This design of suspension has been shown to survive under vibration and will undergo a thermal test in the near future. The thermal effects of the changes is expected to be small.

References

[1] T Gehrels (1984); "Saturn"; University of Arizona Press.

[2] R. Courtin (1985), "The Composition of Satrun's Atmosphere" in "The Atmospheres of Saturn and Titan" ESA SP-241, pp13–20.

[3] D. Gautier (1985) "The Composition of the Titan Atmosphere" in "The Atmospheres of Saturn and Titan" ESA SP-241, pp75-81.

[4] J.I. Lunine (1985) "Titan's Surface: Nature and Implications for Cassini" in "The Atmospheres of Saturn and Titan" ESA SP-241, pp83-88.

[5] R Courtin, D Gautier, A marten and B Bézard (1984) "The composition of Saturn's atmosphere at northern temperate latitudes from Voyager IRIS spectra: NH_3, C_2H_2, C_2H_6, CH_3D, CH_4, and the saturnian D/H isotopic ratio"; Astrophysical Journal **287**; 899-916.

[6] J.K. Beatty, B. O'Leary and A. Chaikin (1981); "The New Solar System"; C.U.P.

[7] Simon Calcutt, Fredric Taylor, Peter Ade, Virgil Kunde and Donald Jennings (1992); "The Composite Infrared Spectrometer"; Journal of the British Interplanetary Society; **45**, pp.811-816.

[8] "Infrared Fourier Spectroscopy of Saturn and Titan from the Cassini Orbiter". Volume 1: Investigation and Technical Plan. Feb 1990.

[9] "Composite Infrared Spectrometer (CIRS) Critical Design Review (Volume 1)"; Goddard Space Flight Center (1994).

[10] S. Werrett, A.L. Seivold (1989) "Thermal Design and Verification of an Instrument Cooling System for Infrared Detectors Utilizing the Oxford Stirling Cycle Refrigerator"

[11] G. Mason (1991) "Test and Calibration of the Along Track Scanning Radiometer, A Satellite-Borne Infrared Radiometer Designed to Measure Sea Surface Temperature", D. Phil. Thesis, Oxford Univiersity.

[12] R.V. Annable (1970) "Radiant Cooling" Applied Optics **9(1)**, p185.

[13] M.J. Donohoe and A. Sherman (1976) "Radiant Coolers - Theory, Flight Histories, Design Comparisons and Future Applications", AIAA Preprint 75-184.

[14] R.H. Hulett, C.A. Zierman (1970) "Staged Radiator Design for Low Temperature Spacecraft Applications", AIAA Paper No. 70–854 from 5th Thermophysics Conference 1970.

[15] I.M. Aptaker (1982) "A Near Infrared Mapping Spectrometer for Investigation of Jupiter and its Satellites"

[16] T.T. Caffertry, D.J Kuyper (1983) "Radiative cryogenic cooler for the Thermatic Mapper" Proceedings - SPIE The international society for optical engineering.

[17] P. Kittel (1993) "Comparison of Dewar supports for space applications" Cryogenics **33**, 4, pp429-434.

[18] "American Institute of Physics Handbook", 3rd edition; McGraw Hill (1972).

[19] G.W.C. Kaye & T.H. Laby; "Tables of Physical & Chemical Constants", 14th Edition; Longman; (1973).

[20] "Materials Selection Guide"; Goddard Space Flight Center; NASA/GSFC/REP/PL/104.

[21] "Titanium Alloy IMI 318"; IMI Titanium.

[22] H. Bansemir & O. Haider (1991) "Basic material data and structural analysis of fibre composite components for space application"; Cryogenics **31**; p298.

[23] Goodfellow Metals Catalogue p458.

[24] "Heat Transfer"; J. P. Holman; McGraw-Hill (1989)

[25] "Thermophysical Properties of Matter Vol. 1"; ed. Y.S. Touloukian.

[26] Carol Mosier, Personal Communication (1991).

[27] M.M. Fulk and M.M. Reynolds (1957) "Emissivities of Metallic Surfaces at 76K", J. Ap. Phys **28**,12, pp1464-1467.

[28] "Eléments de conduction et d'émissivité thermique de la limande. Modèle 'conduction + radiation' : rèsultats"; Philipe Lavocat; Personal Communication; (1992)

[29] "Experimental Techniques in Low Temperature Physics"; G. K. White.

[30] "Vacuum"; Leybold AG Vacuum Technology; Friedr. Vieweg & Sohn (1989).

[31] F. Edelstein, W. Harwell, R. Haslett, W. Timlen (1979) "Shuttle Payload Thermal Control, Volume 2, Insulation design and fabrication", NAS5-23414

[32] T.L. Halaczek and J. Rafalowicz (1986) "Heat Transport in Self Pumping Multilayer Insulation", Cryogenics **26(6)**, pp373–376.

[33] T.L. Halaczek and J. Rafalowicz (1986) "Temperature Variation of Thermal Conductivity of Self-Pumping Multilayer Insulation", Cryogenics **26(10)**, pp544–546.

[34] S.L Bapat, K.G. Narayankhedkar and T.P. Lukose (1990) "Performance Prediction of Multilayer Insulation", Cryogenics **30(8)**, pp700–710.

[35] S.L Bapat, K.G. Narayankhedkar and T.P. Lukose (1990) "Experimental Investigations of Multilayer Insulation", Cryogenics **30(8)**, pp711–719x.

[36] "ESATAN User Manual", ESA PSS-03-105 Issue 1, April 1990.

[37] "The Simplified Space Payload Thermal Analyser", NASA.

[38] "VIEWHEAT User Manual"; ESA PSS-82-07-01.

[39] Han Jun, Cui Guang-De, Hong Guo-Tong, "Test and Study for a Small Sized Environmental Simulator of Space Radiant Coolers", ACE **33** pp1161–1165.

[40] H.E. Nuss, (1987) "Space Simulation Facilities and Recent Experience in Satellite Thermal Testing", Vacuum **37**,pp297–302.

[41] "Spacecraft Thermal Control Design Data" ESA PSS-03-108 Issue 1, November 1989.

[42] "Vacuum", Leybold AG; (1989).

[43] R. Siegel and J. R. Howell (1980?) "Thermal Radiation Heat Transfer" Chapter 8.

[44] "Calculation of Radiative Couplings Allowing for Multiple Reflections in THETA"

[45] S. Ungar, J. Mangin, M. Lutz, G. Jeandel, B. Wyncke (1989) "Infrared Black Paints for Room and Cryogenic Temperatures", SPIE Vol. 1157 Infrared Technology XV, pp369–376.

[46] D. L. Stierwalt (1966) "Infrared Spectral Emittance Measurements of Optical Materials", Applied Optics **5** 12, pp1911–1915.

[47] F. J. J. Clarke and J. A. Larkin (1985) "Measurement of Total Reflectance, Transmittance and Emissivity over the Thermal IR Spectrum", Infrarred Physics **25** 1/2, pp359–367.

[48] E. M. Sparrow and S. H. Lin (1962) "Absorption of Thermal Radiation in a V-Groove Cavity", Int. J. Heat Mass Transfer **5** pp1111-1115.

[49] P. Horowitz & W. Hill (1980) "The Art of Electronics"; CUP

[50] Quinn "Temperature"; 2nd Edition; Academic Press (1990).

[51] A. J. Munday & R. A. Farrar; "An Engineering Data Book"; Macmillan (1990).

[52] T. Nightingale (1993) "An Investigation of the Radiometric Performance of the Improved Stratospheric and Mesospheric Sounder", D. Phil. Thesis, Oxford University.

[53] W.H. Press, B.F. Flannery, S.A. Teukolsky and W.T. Vetterling (1988) "Numerical Recipes in C"; C.U.P.